

**PONTIFICIA UNIVERSIDAD
CATÓLICA DEL PERÚ**

Escuela de Posgrado



Reaction front propagation with thermal driven convection

Tesis para obtener el grado académico de Doctor en Física que
presenta:

Roberto Antonio Guzman Ramirez

Asesor:

Dr. Desiderio Augusto Vasquez Rodriguez

Lima, 2024

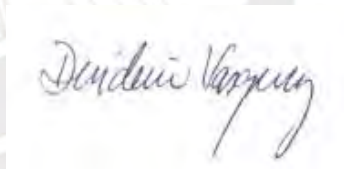
Informe de Similitud

Yo, Desiderio Augusto Vásquez Rodríguez, docente de la Escuela de Posgrado de la Pontificia Universidad Católica del Perú, asesor(a) de la tesis titulada(o) Reaction front propagation with thermal driven convection, de el autor Roberto Antonio Guzman Ramirez, dejo constancia de lo siguiente:

- El mencionado documento tiene un índice de puntuación de similitud de 29%. Así lo consigna el reporte de similitud emitido por el software *Turnitin* el 11/06/2024. No obstante, se tiene que omitir la referencia 1 del informe, ya que corresponde a publicación del mismo alumno. El índice de similitud, omitiendo la referencia señalada, es de 14%, lo que está dentro del límite establecido.,
- He revisado con detalle dicho reporte y la Tesis o Trabajo de investigación, y no se advierte indicios de plagio.
- Las citas a otros autores y sus respectivas referencias cumplen con las pautas académicas.

Lugar y fecha:

Lima, 12 de Junio de 2024.

Apellidos y nombres del asesor / de la asesora: Vásquez Rodríguez, Desiderio Augusto	
DNI: 06480334	Firma 
ORCID: 0000-0003-2436-7221	

Acknowledgments

I am thankful to my parents, who helped me begin this journey in science and have supported me in various ways. This gratitude extends to the many friends who are a great source of support and inspiration to continue with this work.

This research was only made possible with the continuous support from my advisor Desiderio Vasquez, who has taught me for many years both the technical and the humanistic side of research. I am grateful for his patience and expertise.

This work was aided by the financial support from FONDECYT through grant No. 236-2015.



Reaction front propagation with heat induced flow

Propagación de frentes de reacción con flujo inducido por calor

Resumen

Estudiamos la propagación de frentes químicos acoplados a efectos de convección debido a gradientes térmicos. Los frentes de reacción separan fluidos de diferentes densidades debido a gradientes térmicos y de composición. Estas diferencias de densidad puede causar convección. Los frentes pueden describirse mediante una aproximación de frente delgado que separa producto y reactivo en el fluido. Para describir inestabilidades difusivas, el frente evoluciona según la ecuación de Kuramoto-Sivashinsky. Encontramos que el calor producido por la reacción genera convección en frentes exotérmicos que se propagan hacia arriba. Si el fluido de mayor densidad se encuentra encima el fluido de menor densidad, las fuerzas de flotación pueden generar convección. Encontramos que puede aparecer convección si el frente se propaga hacia abajo. Este caso describe fluido de menor densidad en la parte superior. También estudiamos la evolución no lineal de la ecuación de Kuramoto-Sivashinsky acoplada a hidrodinámica. Observamos aumento de velocidad para frentes que se propagan en canales estrechos debido a la convección. Analizamos el efecto de las pérdidas de calor en la propagación de frentes de reacción. La pérdida de calor depende del número de Biot, que representa la cantidad de flujo de calor a través de las fronteras. Para frentes que se propagan verticalmente, encontramos transiciones entre frentes axisimétricos y no axisimétricos, además de regiones de bistabilidad entre ellos. Para frentes que se propagan horizontalmente, la velocidad del frente aumenta a medida que aumentamos el ancho del canal, pero la razón de aumento es más rápida para números de Biot bajos.

Reaction front propagation with thermal driven convection

Abstract

We study chemical front propagation coupled to convection driven by thermal gradients. Reaction fronts separate fluids of different densities due to thermal and compositional gradients. We analyze the presence of convection due to these density differences. Reaction fronts can be described by a thin front approximation that separates reacted from unreacted fluid. For fronts undergoing diffusive instabilities, the front evolution equation corresponds to a Kuramoto-Sivashinsky equation. A horizontal flat front propagating in the vertical direction can exhibit additional instabilities due to density gradients. We found that heat released by the reaction at the front leads to convection for exothermic fronts propagating upward. A positive thermal expansion coefficient will place a higher density fluid above a fluid of lower density, therefore buoyancy forces may lead to convection. However, we also found that convection can appear if the front propagates downward, having the lower density fluid on top. We also solved the non-linear evolution for the Kuramoto-Sivashinsky equation coupled to hydrodynamics. This shows an increase of speed for fronts propagating in narrow channels due to convection. We also analyze the effect of heat losses on the propagation of reaction fronts. Heat losses depend on a Biot number, which represents the amount of heat flow through the boundary. For vertical propagating fronts, we find transitions between axisymmetric and nonaxisymmetric fronts, and regions of bistability between them. For horizontal propagating fronts, the speed of the front increases as we increase the layer width, but the rate of increase is faster for low Biot numbers.

Contents

Acknowledgments	1
Resumen	2
Abstract	3
Table of contents	4
List of Figures	6
Introduction	8
1 Mathematical background	13
1.1 Convective (or material) derivative	13
1.1.1 Reynold's transport theorem	14
1.2 Fourier series	15
1.3 Delta and step functions	17
1.4 Numerical differentiation	18
1.5 Numerical integration	19
1.6 Numerical representation of delta distribution	20
1.7 Numerical solution of differential equations	21
1.7.1 First order ordinary differential equation	21
1.7.2 Second order ODE	22
1.7.3 Advection equation PDE	24
1.7.4 Diffusion equation	25
2 Fluid mechanics	27
2.1 Mass conservation	27
2.2 Momentum transport	28
2.3 Newton's viscosity	30
2.4 Incompressible Navier-Stokes equation	31
2.5 Boussinesq approximation	31
2.6 Stream function and vorticity	32
2.7 Two-dimensional flow	33
2.8 Euler equations and Stokes flow	34
2.9 Darcy's law	36
2.10 Flow in a Hele-Shaw cell	36
3 Heat transport	37

3.1	Fourier's Law	37
3.2	Newton's cooling law	37
3.3	Heat diffusion-advection in a fluid	38
4	Chemical reaction fronts	40
4.1	Chemical transport by diffusion	40
4.2	Quadratic FKPP front equation	41
4.3	Cubic autocatalytic reaction front	42
4.4	Fronts in the IAA reaction	43
4.5	Thin front approximation	44
4.6	Thin front KS equation	47
4.7	Temperature distribution for a thin flat front	48
4.8	Front propagation with heat loss	49
4.8.1	Equations of motion	49
4.8.2	Numerical methods	52
4.9	Thin front with thermal and compositional gradients	53
4.9.1	Equations of motion	53
4.9.2	Linear stability analysis	56
4.9.3	Weakly nonlinear regime	59
5	Exothermic reaction fronts in liquids confined between conductive walls	61
5.1	Results	62
5.1.1	Vertical propagation	62
5.1.2	Horizontal propagation	70
5.2	Summary and discussion	71
6	Front instabilities in the presence of convection due to thermal and compositional gradients	73
6.1	Results	75
6.1.1	Linear stability analysis	75
6.1.2	Nonlinear results	79
6.2	Summary and discussion	85
7	Conclusions	87
	References	89

List of Figures

1	Coordinate system, with origin o , on a level set that represents the convex chemical front propagating with normal speed v_n	45
2	Coordinate system centered in the osculating circle for a convex front.	46
3	Front speed as a function of width for vertical propagation, using walls of different conductivities (different Bi values).	63
4	Concentration (a), temperature (b) and velocity fields (c) for width of $L_x = 49$. The boundary condition corresponds to insulating walls (Bi=0).	64
5	Mixing length as a function of width for vertical propagation, using walls of different conductivities (different Bi values).	65
6	Front speed in vertical propagation for varying Bi numbers and fixed width $L_x=40.6$	66
7	Front speed in vertical propagation for varying Bi numbers and fixed width $L_x=43.4$. Vertical lines describe the region of bistability	67
8	Front speed in vertical propagation for varying Bi numbers and fixed width $L_x=49$. Vertical lines describe the region of bistability	68
9	Concentration (a), temperature (b) and velocity fields (c) for width of $L_x = 49$. The boundary condition includes heat loss (Bi=0.01). These parameters allow bistability.	68
10	Concentration (a), temperature (b) and velocity fields (c) for width of $L_x = 49$. The boundary condition includes heat loss (Bi=0.01). These parameters allow bistability.	69
11	Front speed as a function of width for horizontal propagation using walls of different conductivities (different Bi values).	70
12	Concentration (a), temperature (b) and velocity fields (c) for width of $L_y=40$. The boundary condition includes heat loss (Bi=0.01). These parameters allow bistability.	71
13	Dispersion relations for different positive Rayleigh numbers. Without density gradients ($\mathcal{R}_T = \mathcal{R}_C = 0$), the front is unstable for perturbations of small wavenumbers q . Positive Rayleigh numbers enhance the instability of the front	76
14	Stability map for flat fronts. The shaded region corresponds to stable flat fronts. The numbers correspond to selected values of Rayleigh numbers for dispersion relations shown in in Figs. 15 and 16.	77

15	Dispersion relations for different values of \mathcal{R}_C and positive \mathcal{R}_T . The numbers correspond to different points in Fig. 2. The solid lines are the largest real part of the growth rate. Line 3 also displays the second largest real part of the growth rate. The dotted line 3i displays the non-zero imaginary part of the growth rate for point 3.	78
16	Dispersion relations for points with negative R_T . The curve numbers correspond to the points displayed in Fig. 2. The solid lines are the largest real part of the growth rate. All the corresponding growth rates have no imaginary part.	79
17	Front speed relative to the flat front speed as a function of $\Delta L = L - L_C$ for different values of \mathcal{R}_C and positive \mathcal{R}_T . We also display the case $\mathcal{R}_C = \mathcal{R}_T = 0$.	80
18	Velocity field and front profile (a) for $\mathcal{R}_T = 0.5$ and $\mathcal{R}_C = 0.2$, corresponding to point 1 of figure 14. The color map (b) shows the stream function on a longer region centered at the front, showing two convective rolls. This domain has width $L_x = 2.28$.	81
19	Front speed relative to the flat front speed as a function of the width L , for $\mathcal{R}_T = -2$ and $\mathcal{R}_C = -0.3$. Corresponding to point 5 of the figure 14.	82
20	Velocity field and front profile (a) for $\mathcal{R}_T = -2$ and $\mathcal{R}_C = -0.3$, corresponding to point 5 of figure 14. The color map (b) shows the stream function on a longer region centered at the front, showing two convective rolls. This domain has width $L_x = 13.52$.	82
21	Front speed relative to the flat front speed as a function of the width L , for $\mathcal{R}_T = -0.5$ and $\mathcal{R}_C = 0.15$. Corresponding to point 7 of the figure 14.	83
22	Velocity field and front profile (a) for $\mathcal{R}_T = -0.5$ and $\mathcal{R}_C = 0.15$, corresponding to point 7 of figure 14. The color map (b) shows the stream function on a longer region centered at the front, showing two convective rolls. This domain has width $L_x = 2.89$.	83
23	Velocity field and front profile (a) for $\mathcal{R}_T = -0.5$ and $\mathcal{R}_C = 0.15$, corresponding to point 7 of figure 14. The color map (b) shows the stream function on a longer region centered at the front, showing four convective rolls. This domain has width $L_x = 5.74$.	84

Introduction

This work studies the propagation of chemical fronts in fluids. Chemical reactions convert reactants into products, they can be modeled by time evolution equations that show the changes in chemical concentrations. In some cases, their evolution can lead to steady states, oscillatory states or chemical chaos [1, 2, 3, 4]. Systems that show chemical turbulence appeared in the early theoretical model developed by Kuramoto [5, 6]. The coupling of chemical reactions and molecular diffusion can result in the propagation of a reaction front. These reaction-diffusion models, led by the pioneering work of Turing, show instabilities that result in pattern formation. About forty years later, experiments verified this prediction [7, 8, 9]. This work focuses on the problem of front propagation, where the boundary between reacted and unreacted substances defines a propagating reaction front [10]. As fronts propagate in liquids, their evolution will also depend on fluid motion. To fully account for the front dynamics, we will consider advection-reaction-diffusion equations that involve the fluid velocity.

Front propagation is present in many types of macroscopic phenomena. It describes the evolution of different states of the system along a spatially extended domain. In the context of chemical reactions, front propagation determines the evolution of a flame. Experiments in flame fronts have shown the formation of cellular patterns. The theoretical studies of these fronts led Sivashinsky to develop an equation that describes diffusive instabilities in combustion. This model described experiments that show self-turbulizing behavior of flames [11, 12, 13]. Models for forest fire describe the evolution of the boundary between burnt and unburnt vegetation interacting with the surrounding air, as well as the type of terrain. [14]. The polymerization of a monomer phase also propagates as a front that separates these two phases, these kinds of reactions show advantages in industrial applications [15]. Front propagation also describes the spatial evolution of phase transitions such as solidification in crystal growth. This wavefront can have a planar propagating shape, but this shape can be unstable due to diffusion or thermal effects. Instabilities in propagation and cellular pattern formation are also observed in dendritic crystal growth, which is an important problem to solve in the development of modern batteries [16, 17, 18]. In the context of biological systems, the evolution and spread of a virus is also a front propagation problem. Models for the hepatitis B virus can characterize the conditions when front propagation takes place. In the case of Alzheimer disease, some models consider the evolution of the disease as a propagating front of toxic proteins in the brain. The identification of spiral patterns of chemical activity in the heart is important to

predict tachycardia and fibrillation [19, 20, 21, 22].

Chemical fronts describe the spatial propagation of a chemical substance in an spatially extended domain. Several reactions exhibit propagating fronts of chemical activity, such as the chlorite-tetrathionate (CT) reaction, chlorite-iodate malonic acid (CIMA) reaction, iron(II)-nitric acid reaction, and the iodate-arsenous acid (IAA) reaction [23, 24, 25, 26]. One classic example is the Belousov-Zhabotinsky (BZ) reaction, which is described by a set of differential equations known as the oregonator model. The stirred BZ reaction shows oscillations that helped to establish the validity of the model, which coupled to diffusion describes front propagation in the unstirred reaction. Later experiments showed the formation of Turing patterns in a BZ reaction. Circular symmetry appears in the form of target patterns around a center due to the oscillatory nature of the reaction [27, 28, 29, 30]. Experiments in the BZ reaction also show more complex behaviors such as rotating spiral shapes, and chaotic dynamics. Theoretical models help to explain these complex behaviors [31, 32, 33].

Fluid flow can affect the propagation of chemical fronts in liquids. Fronts propagating inside narrow tubes can be affected by external flow due to an external pressure gradient. This flow, known as the Poiseuille flow, causes advection in the concentration of the species and modifies the speed and shape of the front. Experiments and theories for fronts in the IAA reaction with Poiseuille flow show curved fronts of constant shape that travel with speeds higher than a simple addition of an average fluid velocity [34, 35]. More complex flow dynamics, like the Aref blinking vortex, have been studied in the evolution of the BZ reaction [36]. The fluid flow can also arise due to density changes induced by the chemical reaction itself. Experiments have shown that in the absence of externally imposed flow, reaction fronts can have higher speeds due to density driven convection [37]. This requires considering the hydrodynamic interaction with the chemical properties involved in the reaction. The different chemical compositions in the liquid lead to different densities. Buoyancy forces will induce the less dense fluid to rise above a denser fluid, generating convective flow. In the case of the Rayleigh-Taylor (RT) instability, heavy fluid lies on top of less dense fluid, therefore small perturbations will grow, generating convection. Vertical propagation in the BZ reaction shows that convection takes place only when the width of the domain is higher than a critical value. The IAA reaction shows different front speeds depending on orientation because of density gradients across the front [38, 39, 40]. Theoretical studies of IAA reaction fronts in a Hele-Shaw cell show good agreement with experiments for the RT instability. The IAA reaction in horizontal propagation also shows

that velocity depends on the width of the tube due to density driven convection. Theoretical studies for the CT reaction showed that the RT instability induces fingering shapes on the front [41, 42, 43].

The instability due to density gradients may also arise due to the temperature differences in the fluid. In the case of the Rayleigh-Bénard experiment, heated fluid in the bottom a liquid layer causes convection due to thermal expansion [44]. This instability can lead to convective rolls, or convective patterns known as Bénard cells [45]. The evolution of chemical front must consider the enthalpy of the reaction, which affects the temperature of the fluid. An exothermic reaction rises the temperature of the fluid behind the front heating up the unreacted fluid near the front. Experiments in the CT reaction showed the influence of temperature in three dimensional front propagation [46]. Fronts in both the iron(II)-nitric acid reaction and the chlorite-thiosulfate reaction exhibit changes in shape and speed of the front due to temperature gradients [47]. The influence of heat loss within the fluid can affect the temperature distribution of the fluid. Experiments have shown that temperature decays behind the front for the CT reaction due to heat losses [48]. Theories for vertical propagation in Hele-Shaw cells predict thermal convection even if the fluid of lesser density is above the denser fluid [49]. Further studies showed that the instability also takes place in an unbounded viscous fluids described by the Navier-Stokes equation [50].

Propagating fronts in open layers induce fluid flow due to changes in surface tension across the front. This effect, known as Marangoni flow, changes the front shape in the IAA reaction, and in the BZ reaction [51, 52]. Microgravity experiments on board the European Space Agency sounding rocket MASER 13 isolated this effect from density driven flow [53]. The theoretical description of the IAA reaction coupled with surface tension driven flow accounts for these changes in shape and speed. It also shows that the direction of the surface tension gradient has different effects on the front propagation [54, 55].

Reaction-diffusion models for front propagation account for the front width and velocity in the absence of fluid flow. Since the front width is very thin, the front can be considered as an evolving interface that separates reactants from products. A corresponding front evolution equation involving the surface derivatives describes its propagation. One such equation, an eikonal relation between normal speed and curvature, describes spiral waves in the BZ reaction [56]. The eikonal relation provides a front evolution equation independent of the underlying reac-

tion mechanisms. This relation coupled to hydrodynamics described convection due to density gradients, and surface tension differences across the front [57, 58]. A linear stability analysis of flat fronts propagating in cylindrical tubes predicted transitions to axisymmetric and nonaxisymmetric convection. These transitions were later observed in experiments [59, 60].

In addition to hydrodynamic instabilities, experiments in the IAA reaction showed instability caused by differences in diffusivity between the chemical species. These diffusive instabilities can be modeled by coupled diffusion-reaction equations with different diffusivities, or a front evolution equation similar to the Kuramoto-Sivashinsky (KS) equation [61, 62, 63]. This instability leads to curved fronts depending on the width of the domain. An externally imposed flow changes the conditions of instability, depending on whether this flow supports or opposes the front propagation. Further theoretical work has focused on the interaction between diffusive and hydrodynamic instabilities [64, 65, 66]. Theoretical work determined the stability of fronts described by the KS equation, with either density driven convection, an external Poiseuille flow and Marangoni flow [67, 68, 69].

This thesis focuses on thermal driven convection of chemical fronts. Autocatalytic reaction fronts are exothermic, modifying the temperature of the fluid as they propagate. Here we develop a theoretical framework for the study of reaction-diffusion fronts in the presence of heat release. In these models, we include density changes due to thermal effects, and the possibility of thermal losses through the side boundaries of the domain. In the latter case, heat flow across the walls leads to changes in the shape and the speed of the fronts. This theoretical analysis of thermal losses gives insight into its influence on experimental results, where thermal losses might be unavoidable. Additionally, it shows the possibility of different shapes of fronts and bistability between them. We also study the effect of both thermal and compositional gradients in the KS equation. This aims to describe the effect of convection on diffusive instabilities. We carry out a linear stability analysis that predicts an unexpected instability with a lesser dense fluid on top of a denser fluid. This instability previously appeared in reaction-diffusion models. The thin front approximation shows that the instability is possible for a different description of front propagation. Our numerical studies of the full nonlinear KS equation coupled to hydrodynamics agree with the linear stability analysis.

This thesis is organized as follows. In chapter 1, we develop the mathematical tools

necessary for the theoretical description introduced in this work. This includes a brief description of numerical methods used throughout this work. In chapter 2, we introduce the theory of fluid dynamics from first principles when possible. These equations are complemented with useful approximations related to the hydrodynamics of front propagation. In chapter 3, we include a short description of heat transport. These equations describe the temperature changes due to heat release at the front, which in turn generates thermally driven convection. Chapter 4 deals with the description of chemical fronts. We present reaction-diffusion-advection equations describing front propagation in the presence of fluid flow. In these models, a cubic reaction term coupled to diffusion describes the front propagation in the IAA reaction. We also include a description using a thin front approximation based on an eikonal relation, as well as a brief section on the KS equation. In these cases, heat is released at the front, leading to an analytical solution for the temperature profile of a flat thin front. The last two sections of the chapter deal with the main topics of research of this thesis. For the first problem, we consider the influence of heat losses through the boundary of the domain on the evolution of the reaction front. The second problem is the study of compositional and thermal driven convection on a thin front modeled by the KS equation. In chapter 5, we show the results of the heat loss model, including its effects on the vertical instability of a propagating front. In addition, we find a region of bistability for vertical propagation. We also describe the horizontal propagation with heat loss. These results have been published in reference [70]. In chapter 6, we show the results for the thin front model. The results include dispersion curves from the linear stability analysis, and nonlinear simulations of the system. We find how the conditions for instability depend on the thermal and compositional Rayleigh numbers. The nonlinear results show the increase of speed, the shape of the front, and the fluid velocity field. We published these results in reference [71]. In chapter 7, we summarize this research and present the corresponding conclusions.

1 Mathematical background

The theoretical framework for the description of chemical fronts requires a particular set of mathematical tools. In this chapter, we aim to describe the most important principles that appear in the study of the physical systems. Problems in fluid dynamics require the use of a convective derivative. This procedure is an application of the chain rule in a moving medium, thus receiving its particular name. Most equations relate conservation principles, which require derivatives of conserved quantities to obtain a corresponding transport equation. Reynold's transport theorem describes such procedures that applies to a test volume, surface or line. We introduce Fourier series that allow the solution of partial differential equations (PDE) in a particular domain. In addition, we describe the properties of the Dirac delta function and the Heaviside step function in the context of the theory of distributions. These distributions will be useful in the description of abrupt changes in a continuum problem. For instance, to describe the separation of liquids with different densities and to describe the position of a localized thin interface. The last part of this section shows concepts from numerical analysis that are useful for our work. We introduce finite difference approximations for derivatives and integrals. This allows the numerical solution of PDEs in a discrete grid using a fixed time step. In this manner, we develop the necessary algorithms that can be implemented in a computer.

1.1 Convective (or material) derivative

Physical properties of fluids are described by functions that depend on space and time as $f = f(x, y, z, t)$. These scalar functions can describe the local temperature, density or concentration of a small volume of fluid located at coordinates (x, y, z) . In this case, the calculation of the time derivative of f has to account for the velocity of the fluid. A small test volume at the position (x, y, z) will move according to the fluid velocity such that at a small time later δt the test volume is at the new position $(x + v_x \delta t, y + v_y \delta t, z + v_z \delta t)$. Any property defined within the fluid, like momentum, density or temperature requires taking into account the displacement of the test volume which has this property. The calculation of the time derivative of any extensive quantity f in the fluid has to consider that the positions are functions of time $f = f(x(t), y(t), z(t), t)$. In this case, the total time derivative of the function accounts for the change of positions in time with the chain rule as

$$\frac{df}{dt} = \partial_t f + \partial_x f \frac{dx}{dt} + \partial_y f \frac{dy}{dt} + \partial_z f \frac{dz}{dt}. \quad (1.1)$$

This particular form of the derivative is called the convective derivative, as it includes a convective term that depends on the velocity of the fluid

$$\vec{v} = \frac{dx}{dt}\hat{x} + \frac{dy}{dt}\hat{y} + \frac{dz}{dt}\hat{z}. \quad (1.2)$$

The convective derivative is more compactly written as

$$\frac{df}{dt} = \partial_t f + \vec{v} \cdot \nabla f, \quad (1.3)$$

in terms of the velocity field \vec{v} of the fluid.

1.1.1 Reynold's transport theorem

Physical properties calculated over a certain volume requires an integration over this volume. In a moving medium, the boundaries may evolve in time. Therefore, time derivatives should take into account this change in volume. Reynold's theorem relates the derivatives of a physical quantity with flow across the boundaries [72, 73]. If the medium does not change in time, the change of the property F integrated over a fixed volume is

$$\frac{d}{dt} \int_V F dV = \int_V (\partial_t F) dV, \quad (1.4)$$

where $F = F(x, y, z, t)$. However, in a moving medium, its velocity affects the boundaries of the domain of integration. We can take this into account with the approximation of the change of dV over a small time δt as

$$dV|_{t+\delta t} = dV + \nabla \cdot \vec{v} dV \delta t, \quad (1.5)$$

which is calculated with the Jacobian rule for the change of coordinates [73] or with the algebra of differential forms [74, 75, 76]. On the other hand, the evolution of F is approximated in terms of the convective derivative as

$$F|_{t+\delta t} = F + \partial_t F \delta t + \vec{v} \cdot \nabla F \delta t. \quad (1.6)$$

The following derivative is calculated by using these approximations and keeping terms to first order in δt to obtain

$$\frac{d}{dt} \int_{V(t)} F dV = \int_V (\partial_t F + \nabla \cdot (F\vec{v})) dV. \quad (1.7)$$

This result is known as Reynold's transport theorem. Using Gauss's theorem on the divergence term leads to

$$\frac{d}{dt} \int_{V(t)} F dV = \int_V \partial_t F dV + \int_{\partial V} F \vec{v} dS. \quad (1.8)$$

The last term of this equation is a convective term that takes into account the possibility of flow of the property F across the boundary of V transported due to the velocity field \vec{v} . We will use this result extensively to describe dynamics within fluids.

Using a similar procedure, the time derivative of the flux integral in a moving medium becomes

$$\frac{d}{dt} \int_{S(t)} \vec{F} \cdot d\vec{S} = \int_S \left(\frac{d}{dt} \vec{F} + \vec{F}(\nabla \cdot \vec{v}) - (\vec{F} \cdot \nabla) \vec{v} \right) \cdot d\vec{S}. \quad (1.9)$$

Using Stokes theorem, this result can also be written as

$$\frac{d}{dt} \int_{S(t)} \vec{F} \cdot d\vec{S} = \int_S \left(\partial_t \vec{F} + (\nabla \cdot \vec{F}) \vec{v} \right) \cdot d\vec{S} - \int_{\partial S} (\vec{v} \times \vec{F}) \cdot d\vec{\ell}. \quad (1.10)$$

In this case, the last term of eq. (1.10) represents the rotation of the surface element as time evolves. Additionally, this procedure also applies to integration over a moving line [72].

1.2 Fourier series

We often use the representation of functions as series of sines or cosines when working with differential equations. In the case of a periodic function $f(x)$, we have the Fourier series

$$f(x) = \frac{a_0}{2} + \sum_{n=1}^{\infty} a_n \cos nx + \sum_{n=1}^{\infty} b_n \sin nx. \quad (1.11)$$

The coefficients of these series are obtained from integration [77]. These series are useful to solve problems such as the evolution of temperature T in a one dimensional domain. As an example, we will use a Fourier series expansion to solve the heat equation, which is a partial differential equation. In this case, the evolution of the temperature T is determined by

$$\partial_t T = \alpha \partial_x^2 T, \quad (1.12)$$

over a one dimensional domain described by $x \in [0, L]$. We impose no heat flow through the boundaries of the domain setting

$$\partial_x T = 0. \quad (1.13)$$

The solution involves separation of variables, where the Laplacian operator allows for the solution with a basis of orthogonal functions [78]. This allows to expand T with only a corresponding Fourier cosine series

$$T(x, t) = \sum_n \tilde{T}_n(t) \cos(nqx), \quad (1.14)$$

with $q = \pi/L$. This expansion transforms the problem into a set of ordinary differential equations for \tilde{T}_n . Introducing the series into eq. (1.12) we obtain

$$\sum_n \cos(nqx) \frac{d}{dt} \tilde{T}_n = \sum_n \alpha(nq)^2 (-\cos(nqx)) \tilde{T}_n. \quad (1.15)$$

Since the cosines form a set of linearly independent functions, the expansion coefficients should be equal term by term, therefore

$$\frac{d}{dt} \tilde{T}_n = -\alpha(nq)^2 \tilde{T}_n. \quad (1.16)$$

The solution of each equation corresponds to an exponential function. Introducing these results into the Fourier series, we obtain the general solution of the heat equation with insulating boundary conditions

$$T(x, t) = \sum_n \tilde{T}_n(0) \exp(-n^2 q^2 \alpha t) \cos(nqx). \quad (1.17)$$

The initial condition $T(x, 0)$ determines the coefficients $\tilde{T}_n(0)$. In this example, we obtain the coefficients using linear independence. However, we will deal with more extensive differential equations where we might need to explicitly find projections over the desired basis. In such cases, we might need to impose orthogonal conditions of the basis:

$$\frac{2}{L} \int_0^L \cos(lqx) \cos(mqx) dx = \delta_{l,m}, \quad (1.18)$$

and

$$\frac{2}{L} \int_0^L \sin(lqx) \sin(mqx) dx = \delta_{l,m}, \quad (1.19)$$

where $\delta_{l,m}$ is the Kronecker delta [77]. It is useful to consider integrals where the cosine and sine terms are multiplied. Here we have

$$\frac{2}{L} \int_0^L \cos(mqx) \sin(nqx) dx = \begin{cases} 0 & \text{if } m = n \\ \frac{2n}{\pi(m^2 - n^2)} ((-1)^{m+n} - 1) & \text{if } m \neq n \end{cases}. \quad (1.20)$$

For our work, we will also make use of the following integrals

$$\frac{2}{L} \int_0^L \cos(lqx) \sin(mqx) \sin(nqx) dx = \begin{cases} \delta_{m,n} & \text{if } l = 0 \\ \frac{1}{2}(\delta_{|m-n|,l} - \delta_{m+n,l}) & \text{if } l \geq 1 \end{cases}, \quad (1.21)$$

and

$$\frac{2}{L} \int_0^L \cos(lqx) \cos(mqx) \cos(nqx) dx = \begin{cases} \delta_{m,n} & \text{if } l = 0 \\ \frac{1}{2}(\delta_{|m-n|,l} + \delta_{m+n,l}) & \text{if } l \geq 1 \end{cases}. \quad (1.22)$$

These triple product integrals are useful when dealing with nonlinear terms. Consider for instance the inviscid Burgers equation for $u = u(x, t)$ as

$$\partial_t u + u \partial_x u = 0. \quad (1.23)$$

This equation is a model for the propagation shock waves [79, 80]. As an example, we introduce $u(x, t)$ as a fourier series in the spatial variable

$$u = \sum \tilde{u}_n(t) \sin(nqx), \quad (1.24)$$

similar as with the heat diffusion equation. Introducing the series into the differential equation, we get

$$\frac{d\tilde{u}_n}{dt} \sin(nqx) + \tilde{u}_n \tilde{u}_m \sin(nqx) (mq) \cos(mqx) = 0. \quad (1.25)$$

The corresponding equations for \tilde{u}_n are obtained by projecting over the basis function as

$$\frac{d\tilde{u}_n}{dt} \int_0^L \sin(nqx) \sin(kqx) dx + \tilde{u}_n \tilde{u}_m (-mq) \int_0^L \sin(nqx) \cos(mqx) \sin(kqx) dx = 0. \quad (1.26)$$

These triple product integrals are known results, and the differential equation for each term can be explicitly calculated.

1.3 Delta and step functions

The Dirac delta function $\delta(x)$ is an object defined by the sifting property

$$\int_{-\infty}^{\infty} f(x) \delta(x - x_0) dx = f(x_0), \quad (1.27)$$

for any well-behaved function f [81]. In this section, we will omit the limits of integration and assume the integrals are taken over the whole real line. We then write the sifting property as

$$\int f(x) \delta(x - x_0) dx = f(x_0). \quad (1.28)$$

The Dirac delta is useful in electromagnetism to describe point charges, and in mechanics it describes impulsive forces. It also appears in the study of impulsive signals in the brain and their interactions [82].

The Dirac delta function $\delta(x)$ is formally described as a distribution, which is a generalized function where classical derivative may not exist [83]. In this manner,

it allows for the integration with standard functions. For example, the definition of the derivatives of the Dirac delta function is obtained from integration by parts

$$\int f(x)\delta'(x)dx = f\delta'|_{-\infty}^{\infty} - \int f'(x)\delta(x) = -f'(0), \quad (1.29)$$

where we have assumed that f goes to zero outside a compact domain. This is generalized for higher order derivatives as

$$\int \left(\left(\frac{d}{dx} \right)^n \delta(x) \right) f dx = (-1)^n f^{(n)}(0), \quad (1.30)$$

with iteration of integration by parts as shown in [84]. The superscript (n) denotes the n -th derivative.

Another useful distribution is the unitary step function $\Theta(x)$ (or Heaviside function) defined as

$$\Theta(x) = \begin{cases} 0 & \text{if } -\infty < x < 0 \\ 1 & \text{if } 0 \leq x < \infty \end{cases}. \quad (1.31)$$

Some definitions consider the value at zero as $\Theta(0) = 1/2$ [85]. Its weak derivative $\Theta'(x)$ is the Dirac delta $\delta(x)$ [83]. This can be shown by its action on an integral as

$$\int_{-\infty}^{\infty} f\Theta' dx = - \int_{-\infty}^{\infty} f'\Theta = - \int_0^{\infty} f' = f(0). \quad (1.32)$$

This is the sifting property that defines the Dirac delta. We conclude that $\Theta'(x) = \delta(x)$.

Other important properties include the composition of distributions with standard functions [86]. All of these tools will help us describe models where the physical description includes sharp or abrupt structure such as surfaces and points in a three dimensional domain. Moreover, distributions are useful to describe discontinuities in functions such as in the case of reaction fronts.

1.4 Numerical differentiation

The solution of nonlinear differential equations will require the development of algorithms that approximate the solutions of these equations. They will be programmed later in a digital computer. We apply the method of finite differences to approximate the derivatives on a discrete grid. Accordingly, we choose a set of points x_i uniformly distributed on the x axis with a spacing equal to Δx between

adjacent points. The values of the function f evaluated at discrete points x_i are represented as

$$f_i = f(x_i). \quad (1.33)$$

This notation will be used to describe numerical algorithms associated with the function f .

Using a truncated Taylor expansion, we find that the first derivative of the function at the point x_i can be approximated by a forward finite difference scheme

$$\frac{df}{dx}\Big|_{x_i} = \frac{f_{i+1} - f_i}{\Delta x} + \mathcal{O}(\Delta x). \quad (1.34)$$

Here $\mathcal{O}(\Delta x)$ indicates terms of order Δx and higher. Another useful scheme is the backward difference formula

$$\frac{df}{dx}\Big|_{x_i} = \frac{f_i - f_{i-1}}{\Delta x} + \mathcal{O}(\Delta x), \quad (1.35)$$

which is an approximation of the same order as before. A higher order approximation can be achieved with a centered difference formula

$$\frac{df}{dx}\Big|_{x_i} = \frac{f_{i+1} - f_{i-1}}{2\Delta x} + \mathcal{O}(\Delta x^2), \quad (1.36)$$

which has an error of quadratic order and higher [87].

The second derivative can be approximated by a central three point scheme

$$\frac{d^2f}{dx^2}\Big|_{x_i} = \frac{f_{i+1} + f_{i-1} - 2f_i}{\Delta x^2} + \mathcal{O}(\Delta x^2). \quad (1.37)$$

This is accurate to order Δx^2 [87].

1.5 Numerical integration

Integrals can also be approximated using a discretized grid. The solution can be carried out by calculating the area under the curve with polynomial approximations of the curve. The first algorithm uses two points to get a linear approximation and calculate the area of the trapezoid. This results in the approximation for the integral as

$$\int_a^b f(x)dx = \frac{\Delta x}{2} \sum_{i=0}^{n-1} (f_i + f_{i+1}). \quad (1.38)$$

Where we have $n + 1$ points that divide the domain (a, b) into n uniform segments of uniform width $\Delta x = (b - a)/n$.

More accurate results rely on quadratic approximation of the curve, using three consecutive points on the grid to fit a parabola. This procedure results in Simpson's rule [88], which for an odd number of points in the grid corresponds to

$$\int_a^b f(x)dx = \frac{\Delta x}{3} \sum_{i=0}^{n/2-1} (f_{2i} + 4f_{2i+1} + f_{2i+2}). \quad (1.39)$$

With a similar expression if the number of points is even. This method provides a higher accuracy compared to the trapezoidal rule [89].

1.6 Numerical representation of delta distribution

The numerical integration method can be used to define the representation of the delta distribution. Using the sifting property, we require that the numerical delta $\delta(x)$ satisfies

$$\int f(x)\delta(x - x_j)dx = f_j. \quad (1.40)$$

Evaluating the integral over a discrete uniformly spaced grid leads to

$$\sum_i f_i \delta_{i,j} \Delta x = f_j, \quad (1.41)$$

defining a numerical representation of the delta function as

$$\delta_{i,j} = \begin{cases} 0 & \text{if } i \neq j \\ \frac{1}{\Delta x} & \text{if } i = j \end{cases}. \quad (1.42)$$

This approach also applies for the numerical representation of the derivatives of the delta function [84]. For the first derivative, the numerical integral can be represented by

$$\sum_i f_i \delta'_{ij} \Delta x = \frac{f_{j-1} - f_{j+1}}{2\Delta x}. \quad (1.43)$$

Where we have used the centered difference formula. This corresponds to the rule

$$\delta'_{ij} = \begin{cases} \frac{1}{2\Delta x^2} & \text{if } i = j - 1 \\ -\frac{1}{2\Delta x^2} & \text{if } i = j + 1 \\ 0 & \text{if } i \neq j \pm 1 \end{cases}. \quad (1.44)$$

For the second derivative, we have

$$\sum_i f_i \delta''_{ij} \Delta x = \frac{f_{j+1} + f_{j-1} - 2f_j}{\Delta x}. \quad (1.45)$$

Which corresponds to the rule

$$\delta_{ij}'' = \begin{cases} \frac{1}{\Delta x^2} & \text{if } i = j + 1 \\ \frac{1}{\Delta x^2} & \text{if } i = j - 1 \\ -\frac{2}{\Delta x^2} & \text{if } i = j \\ 0 & \text{other cases} \end{cases}. \quad (1.46)$$

These representations will become useful in the numerical solution of problems involving discontinuities.

1.7 Numerical solution of differential equations

We will approximate the differential equations using numerical finite differences for the derivatives. The resulting algorithms can be implemented in a digital computer. From the many possible methods, the chosen algorithm should balance simplicity, accuracy and stability. In this section, we discuss finite difference algorithms applied to differential equations.

1.7.1 First order ordinary differential equation

For the first order ordinary differential equation (ODE) given by

$$\frac{dy}{dt} = g(y, t), \quad (1.47)$$

where g is a known function, we can find a numerical solution by considering a discretized time domain. Using a time step Δt , the derivative can be approximated by a forward difference formula and the function g is evaluated at the present time $g(y_i, t_i) = g_i$. We obtain the discretization

$$\frac{y_{i+1} - y_i}{\Delta t} = g_i, \quad (1.48)$$

with $y_i = y(t_i)$. This leads into an iterative algorithm for the evolution of $f(t)$ as

$$y_{i+1} = y_i + g_i \Delta t. \quad (1.49)$$

This algorithm is referred to as the explicit (or forward) Euler method [90]. It requires the explicit evaluation of g at the present time step i .

Using different finite difference approximations will lead to different algorithms. For example, applying a backwards difference formula we have

$$\frac{y_i - y_{i-1}}{\Delta t} = g_i, \quad (1.50)$$

which can be rewritten by shifting each index as

$$\frac{y_{i+1} - y_i}{\Delta t} = g_{i+1}. \quad (1.51)$$

This backward difference formula requires knowledge of g at the future time step g_{i+1} . This algorithm is known as the implicit (or backward) Euler method, where the evaluation of g is implicit.

Another important aspect to consider is the stability of the algorithm. This stability property refers to the convergence of the solutions after a long time. The choice of algorithm will be restricted by this property. In some cases, it can be controlled by choosing an appropriate value for the time step Δt . In other cases, choosing backward Euler instead of forward Euler will minimize possible instabilities [90].

1.7.2 Second order ODE

This type of equation involves the second derivative of the unknown function. In addition to time evolution equations, we find second order boundary value problems. For the time evolution equation, the initial state and its derivative are known, whereas the boundary value problem requires knowledge of the function on the boundaries of a domain. One such equation is the one dimensional Poisson equation defined as

$$\frac{d^2 f}{dx^2} = g, \quad (1.52)$$

where $g = g(x)$ is known.

This problem can be treated numerically by discretizing the second derivative as

$$\frac{f_{i-1} - 2f_i + f_{i+1}}{\Delta x^2} = g_i, \quad (1.53)$$

with two additional equations that represent the boundary conditions. These conditions specify the values of the function at the boundary, or the values of the derivatives, or a combination of both. The unknown function values f_i describe a tridiagonal system of equations. This system can be solved by Thomas algorithm [91], which is an efficient method for solving this system of equations. It is an explicit version of a gaussian elimination procedure in the special case of tridiagonal systems. This algorithm inverts the matrix of order $n \times n$ with a number of operations proportional to order n , whereas the most general gaussian elimination is of order n^3 [92]. The set of equations obtained from eq. (1.53) corresponds to n unknowns f_i , considering that the boundaries determine expressions for f_0 and f_{n+1} . This leads to a tridiagonal system for n unknowns $x_i = f_i$ determined by

$$a_i x_{i-1} + b_i x_i + c_i x_{i+1} = d_i, \quad (1.54)$$

with $a_1 = 0$ and $c_n = 0$. The solution proceeds by first scaling the equations. The first equation takes the form

$$x_1 + \frac{c_1}{b_1}x_2 = \frac{d_1}{b_1}, \quad (1.55)$$

then we scale the second equation and eliminate x_1 to obtain

$$x_2 + \frac{c_2}{b_2 - c'_1 a_2}x_3 = \frac{d_2 - a_2 d'_1}{b_2 - c'_1 a_2}. \quad (1.56)$$

Where $c'_1 = c_1/b_1$ and $d'_1 = d_1/b_1$. The rest of the equations can be recursively reduced by

$$c'_i = \frac{c_i}{b_i - c'_{i-1} a_i}, \text{ and } d'_i = \frac{d_i - a_i d'_{i-1}}{b_i - c'_{i-1} a_i}. \quad (1.57)$$

The corresponding equations now read

$$x_i + c'_i x_{i+1} = d'_i. \quad (1.58)$$

Since the last equation corresponds to $x_n = d'_n$, it allows the solution by backward substitution with the known values of c'_i and d'_i using $x_{i-1} = d'_i - c'_i x_i$.

The Thomas algorithm has allowed us to directly solve the Poisson equation. However, this limits us to use the three point formula for the second derivative. Any other representation of the derivative results in a different system of equations. An alternative method is the relaxation algorithm. We show how to introduce the relaxation method for the discretization defined in eq. (1.53). This method is based in a Jacobi iteration scheme [90], where the function f is assumed to be an initial guess, and the values are iterated such that

$$\frac{f_{i-1}^n - 2f_i^{n+1} + f_{i+1}^n}{\Delta x^2} = g_i. \quad (1.59)$$

Here f^n represents the function at the n -th iteration of the method. These iterations continue until convergence, where $f^n = f^{n+1}$, therefore satisfying the original Poisson equation eq. (1.53). The algorithm for updating f_i according to this discretization is

$$f_i^{n+1} = \frac{1}{2}(f_{i-1}^n + f_{i+1}^n - \Delta x^2 g_i). \quad (1.60)$$

For points near the boundary, we require equations that describe the appropriate boundary conditions. The solution of problems with a relaxation algorithm can be optimized by introducing an appropriate initial guess for f .

1.7.3 Advection equation PDE

In physical situations, we are interested in equations where the unknown function depends on space and time. One important example is the advection equation

$$\partial_t f + v \partial_x f = 0. \quad (1.61)$$

This equation represents the advection of the function f by a constant velocity field v . The solution for f corresponds to the initial condition given by $f_0 = f(x, 0)$, displaced by a distance vt :

$$f(x, t) = f_0(x - vt, t). \quad (1.62)$$

The numerical solution of this problem involves discretization in space and time. We describe the discretized function with two indices $f(x_i, t_n) = f_i^n$, approximating the derivatives with two point algorithms. With the function advecting to the right ($v > 0$), we choose the spatial derivative in the opposite direction. This leads to the iterative algorithm for f

$$\frac{f_i^{n+1} - f_i^n}{\Delta t} + v \frac{f_i^n - f_{i-1}^n}{\Delta x} = 0. \quad (1.63)$$

This choice of algorithm helps avoid numerical instabilities as compared to other choices such as a downwind scheme [90]. The upwind differentiation scheme gives an iteration equation for the function at every time step as

$$f_i^{n+1} = f_i^n + \frac{v \Delta t}{\Delta x} (f_i^n - f_{i-1}^n). \quad (1.64)$$

This algorithm has a slight inconvenience. It can be shown that this finite difference scheme represents an additional diffusion term [90]. This scheme is satisfied by the same advection equation, but with an additional diffusive term as

$$\partial_t f + v \partial_x f = \frac{v}{2} (\Delta x - v \Delta t) \partial_x^2 f. \quad (1.65)$$

The diffusive term depends on the size of the grid and can be made sufficiently small by increasing the number of points in the grid. But the diffusive behavior might still be present if the evolution is carried out on a long time scale.

The analysis of the stability for the advection problem leads to a constraint on the grid values named Courant-Friedrichs-Lewy (CFL) condition [93]. In the scheme we proposed, the von Neumann analysis gives the following CFL condition

$$0 < v \frac{\Delta t}{\Delta x} < 1. \quad (1.66)$$

When this condition is not met, the iterative procedure diverges. It is interesting to note that the sign of v is important, since we have the condition that this scheme is only stable for advection towards the positive axis. This stability is what characterizes the upwind differentiation scheme. The CFL condition imposes a balance on the choice of the discretization in both time and space. It might be useful to have good spatial resolution with small Δx . However, this forces Δt to be also very small to avoid numerical instability. As a heuristic rule, we might remember this as having a grid velocity, defined as $\Delta x/\Delta t$, greater than the speed of the advection.

1.7.4 Diffusion equation

We turn our attention to a higher order partial differential equation (PDE), a parabolic equation that represents the diffusion process:

$$\partial_t f = D \partial_x^2 f. \quad (1.67)$$

Where D is a constant that represents the diffusion coefficient. Similarly to the advection equation, we have to develop a combined scheme with derivatives in time and in space. The simplest algorithm corresponds to a forward simple Euler time derivative combined with a central finite difference approximation for the spatial derivative

$$\frac{f_i^{n+1} - f_i^n}{\Delta t} = \frac{D}{\Delta x^2} (f_{i+1}^n + f_{i-1}^n - 2f_i^n), \quad (1.68)$$

with the indices as $f(x_i, t_n) = f_i^n$. The solution relies on iterating this scheme as

$$f_i^{n+1} = f_i^n + \frac{D\Delta t}{\Delta x^2} (f_{i+1}^n + f_{i-1}^n - 2f_i^n). \quad (1.69)$$

This algorithm requires choosing small time steps to avoid numerical instabilities [87]. A more robust method is the Crank-Nicholson algorithm, which calculates the second derivative as the mean of the derivative between the time steps as

$$\frac{f_i^{n+1} - f_i^n}{\Delta t} = \frac{D}{2} (\partial_x^2 f^{n+1} + \partial_x^2 f^n), \quad (1.70)$$

however this requires solving for the unknowns f_i^{n+1} . This can be achieved using the Thomas algorithm for the tridiagonal system of equations. Writing the spatial derivatives explicitly we have

$$\frac{f_i^{n+1} - f_i^n}{\Delta t} = \frac{D}{2\Delta x^2} (f_{i+1}^n + f_{i-1}^n - 2f_i^n + f_{i+1}^{n+1} + f_{i-1}^{n+1} - 2f_i^{n+1}). \quad (1.71)$$

Reordering the terms, we find a tridiagonal system of equations

$$\left(-\frac{D}{2\Delta x^2}\right) f_{i-1}^{n+1} + \left(\frac{1}{\Delta t} + \frac{D}{2\Delta x^2}\right) f_i^{n+1} + \left(-\frac{D}{2\Delta x^2}\right) f_{i+1}^{n+1} = \frac{f_i^n}{\Delta t} + \frac{D}{2} \partial_x^2 f^n, \quad (1.72)$$

which can be readily solved with the algorithm described for eq. (1.54).

We can develop a similar method for the solution for the two dimensional diffusion problem

$$\partial_t f = D\partial_x^2 f + D\partial_y^2 f. \quad (1.73)$$

In this case, instead of averaging the derivative, we can treat only one dimension implicitly at each half time step. Then the algorithm requires two steps, first

$$\frac{f_i^{n+1} - f_i^n}{(\Delta t/2)} = D\partial_x^2 f^{n+1} + D\partial_y^2 f^n \quad (1.74)$$

where the x derivative is calculated implicitly, and later the y derivative is considered implicitly:

$$\frac{f_i^{n+1} - f_i^n}{(\Delta t/2)} = D\partial_x^2 f^n + D\partial_y^2 f^{n+1}. \quad (1.75)$$

This algorithm is called alternate direction implicit (ADI) [94]. Using this scheme, we allow for more numerical stability and the time step is not restricted to a very small value. This is very valuable in two dimensional problems, as the computational time increases rapidly depending on the size of the grid.

2 Fluid mechanics

In this thesis we consider the propagation of reaction fronts in liquids. In these cases, fluid flow modifies the dynamics of the reaction. This flow may be caused by an external pressure gradient, such as fluid flowing in a tube with a corresponding Poiseuille flow profile. In other cases, the reaction itself can induce density changes resulting in convection. This change in density can be caused by changes in the chemical compositions, as well as changes in temperature due to heat released or absorbed by the reaction. The interaction between the reaction and the fluid requires the use of dynamic relations for the fluid velocity field. In this chapter, we will introduce the Navier-Stokes equation for the evolution of viscous flow. This equation is derived considering the momentum transport in the fluid. The induced flow can be described using the Boussinesq approximation, where the change in density appears only in the large gravity term. To eliminate the pressure from the equations, we will develop a vector potential description for the velocity field. In this context, the velocity will be described by a vorticity and a stream functions. The NS equations can be simplified depending on the specific situation. Reaction experiments carried out in Hele-Shaw cells allow for a simplified description using Darcy's law. The experimental parameters of interest may allow additional simplifications, for instance if viscosity is large, we may use a Stokes flow approximation. In order to use the appropriate models for the problem we have to take into account the scaling of the equations.

2.1 Mass conservation

The evolution of a fluid medium requires developing properties for the scalar and vector fields within the domain. The first property we describe is mass conservation. The mass in any volume element can be calculated from a density field as

$$\int \rho dV = M. \quad (2.1)$$

The condition of mass conservation requires that M behave as a constant. This is described by a zero derivative, with the derivative following Reynolds transport theorem (eq. (1.7)) as

$$\frac{d}{dt}M = 0 = \frac{d}{dt} \int \rho dV = \int \partial_t \rho + \nabla \cdot (\rho \vec{v}) dV. \quad (2.2)$$

This equation leads to the following equivalent statement

$$\int \partial_t \rho dV = - \int \nabla \cdot (\rho \vec{v}) dV, \quad (2.3)$$

such that changes in density within a volume is only possible if it is transported by a velocity field. Using the Stokes theorem we also have

$$\int_V \partial_t \rho dV = - \int_S \rho \vec{v} \cdot d\vec{A}, \quad (2.4)$$

which provides the change in density by calculating how much mass flows outwards from the domain. From the conservation of mass given by

$$\int (\partial_t \rho + \nabla \cdot (\rho \vec{v})) dV = 0, \quad (2.5)$$

we obtain a differential form of the conservation law. This expression must be zero for any volume, thus the expression inside the integral must be always zero

$$\partial_t \rho + \nabla \cdot (\rho \vec{v}) = 0. \quad (2.6)$$

This is the continuity equation which guarantees mass conservation. In the case of incompressible flow, the density is assumed as a constant. This simplifies the equation into the condition that the velocity field is divergenceless

$$\nabla \cdot \vec{v} = 0. \quad (2.7)$$

2.2 Momentum transport

We analyze the mass of a small volume of fluid to measure the momentum transfer [95]. In the test volume, forces provide its acceleration, as stated by Newton's second law

$$\vec{F}_{tot} = \frac{d}{dt}(m\vec{v}). \quad (2.8)$$

When this is applied to the test mass, we have the change of momentum as an integral

$$\frac{d}{dt}\vec{p} = \frac{d}{dt} \left(\int \vec{v} dm \right) = \frac{d}{dt} \left(\int \vec{v} \rho dV \right). \quad (2.9)$$

Additionally, forces can act distributed over the whole volume of the test mass, and also distributed over the surface of the test mass. The force \vec{F}_{tot} is described as the sum of two components which are the vectors \vec{f} and \vec{T} . The first term \vec{f} describes the force per unit mass distributed over the volume of the test mass. The second term \vec{T} measures the force distributed over the surface of the test mass. The total force is described by the sum

$$\left(\vec{F}_{tot} \right) = \int \vec{f} dm + \int \vec{T} dS. \quad (2.10)$$

The surface force is considered as arising from the stress tensor σ_{ij} , such that the components of \vec{T} are $T_i = \sigma_{ij}n_j$, with n_j the components a normal unit vector to the surface. In this expression, and from now on, we assume Einstein's summation convention for the indices, such that if an index appears twice in an expression, it implies a sum over the repeated index. The total force takes the new form in terms of components

$$(F_{tot})_i = \int f_i \rho dV + \int \sigma_{ij} n_j dS. \quad (2.11)$$

This expression can be further simplified using Gauss's theorem

$$(F_{tot})_i = \int f_i \rho dV + \int \partial_j \sigma_{ij} dV. \quad (2.12)$$

The final result is the dynamical equation for a test mass contained in a small volume dV , therefore the change in momentum is equal to the total forces

$$\frac{d}{dt} \int \rho v_i dV = \int f_i \rho dV + \int \partial_j \sigma_{ij} dV. \quad (2.13)$$

The time derivative is carried out as in the Reynolds transport theorem (eq. (1.7)) to obtain

$$\int (\partial_t(\rho v_i) + \partial_j(\rho v_i v_j)) dV = \int f_i \rho dV + \int \partial_j \sigma_{ij} dV. \quad (2.14)$$

For any volume element the integrals have to be equal, therefore we obtain a differential form for the dynamical equation

$$\partial_t(\rho v_i) + \partial_j(\rho v_i v_j) = f_i \rho + \partial_j \sigma_{ij}. \quad (2.15)$$

This can be simplified by using the mass conservation condition (eq. (2.6)) in the left hand side of this equation

$$\partial_t(\rho v_i) + \partial_j(\rho v_i v_j) = v_i(\partial_t \rho + \partial_j(\rho v_j)) + \rho \partial_t v_i + \rho v_j \partial_j v_i. \quad (2.16)$$

Here the factor of v_i in the right hand side is the continuity equation, since this factor is zero, we obtain

$$\partial_t(\rho v_i) + \partial_j(\rho v_i v_j) = \rho \partial_t v_i + \rho v_j \partial_j v_i. \quad (2.17)$$

This results in Cauchy's momentum equation

$$\rho \partial_t v_i + \rho v_j \partial_j v_i = f_i \rho + \partial_j \sigma_{ij}. \quad (2.18)$$

The evolution equation requires knowledge of the force distribution f_i and the stress tensor σ_{ij} . For certain fluids, such as water at room temperature, the stress tensor can be described by Newton's viscosity [96].

2.3 Newton's viscosity

To apply Cauchy's momentum equation, we need to account for the stress tensor σ_{ij} . In general, the stress tensor will depend on the thermodynamic state in terms of internal energy (temperature), the mass density, and on the velocity gradients. Assuming a linear dependence on the velocity gradient, the simplest form for the tensor gives

$$\sigma_{ij} = A_{ij} + B_{ijkl}\partial_k v_l. \quad (2.19)$$

This is further simplified by the assumption that the tensor has to be isotropic. That is, independent of the rotation of coordinates. This assumption is related to the conservation of angular momentum for small volume elements. The possibility of angular momentum change at small scales requires a different approach [73]. In this case, the stress tensor involves a second order tensor component A , and a fourth order component B . The only possible isotropic two order tensor is any multiple of the Kronecker delta δ_{ij} as

$$A_{ij} = \alpha\delta_{ij}, \quad (2.20)$$

and the only possible fourth order tensor is composed of products of Kronecker deltas [97]. This general fourth order isotropic tensor is

$$B_{ijkl} = \lambda\delta_{ij}\delta_{kl} + \mu(\delta_{ik}\delta_{jl} + \delta_{il}\delta_{jk}) + \nu(\delta_{ik}\delta_{jl} - \delta_{il}\delta_{jk}). \quad (2.21)$$

Where λ , μ and ν are arbitrary scalars. Each component has a geometrical meaning [98]. In the case of the stress tensor, the third term ν vanishes when multiplied with $\partial_k v_l$ in eq. (2.19). The resulting form of the tensor becomes

$$\sigma_{ij} = -p\delta_{ij} + \lambda\partial_k v_k\delta_{ij} + \mu(\partial_i v_j + \partial_j v_i). \quad (2.22)$$

The first term is the thermodynamic pressure p that is present even in the absence of flow. We also define the mechanical pressure as the mean of the eigenvalues of the stress tensor

$$p_m = -\frac{1}{3}\sigma_{ii}. \quad (2.23)$$

The difference between these pressures is that mechanical pressure is only related to the translational energy of the molecules, whereas the thermodynamic pressure accounts for the additional degrees of freedom such as rotation or vibration [99]. The term proportional to μ relates to a change of shape for a small volume of fluid, therefore this term is proportional to the strain rate tensor $S_{ij} = (\partial_i v_j + \partial_j v_i)/2$.

The stress tensor is further simplified under the Stokes assumption [73], which states that the thermodynamic pressure and the mechanical pressure are equal.

Thus, in the relation

$$-p_m = -p + \left(\lambda + \frac{2}{3}\mu \right) \partial_i v_i, \quad (2.24)$$

we get a condition between λ and μ . The Stokes assumption requires $\lambda = -\frac{2}{3}\mu$. In this way, we obtain Newton's viscosity law

$$\sigma_{ij} = -p\delta_{ij} - \frac{2}{3}\mu\partial_k v_k\delta_{ij} + 2\mu S_{ij}, \quad (2.25)$$

here μ corresponds to the coefficient of dynamic viscosity.

2.4 Incompressible Navier-Stokes equation

The Navier-Stokes (NS) equation describes the momentum transport coupled to Newton's viscosity law. The general form is

$$\rho\partial_t v_i + \rho v_j \partial_j v_i = f_i \rho + \partial_j \left(-p\delta_{ij} - \frac{2}{3}\mu\partial_k v_k\delta_{ij} + 2\mu S_{ij} \right). \quad (2.26)$$

We can reduce the equation further assuming constant μ and constant ρ , which leads to the incompressibility condition $\partial_i v_i = 0$. Therefore, the rectangular components of the NS equation are

$$\rho\partial_t v_i + \rho v_j \partial_j v_i = f_i \rho - \partial_i p + \mu\partial_j \partial_j v_i. \quad (2.27)$$

In vector form, we write

$$\rho\partial_t \vec{v} + \rho(\vec{v} \cdot \nabla)\vec{v} = \rho\vec{f} - \nabla p + \mu\nabla^2 \vec{v}. \quad (2.28)$$

When the only external force acting on the fluid is gravity, we use $\vec{f} = \vec{g}$, with \vec{g} being the gravitational acceleration. In order to solve the equations we need to obtain four functions: three velocity components and one pressure term. The full solution of the system would require solving the dynamical equation along with the incompressibility condition.

2.5 Boussinesq approximation

In the study of convection, experiments show that density gradients cause convection due to buoyancy forces. The NS equation can be studied using the Boussinesq approximation, which assumes that the density is constant except when it multiplies the gravity term [100, 101]

$$\rho_0\partial_t \vec{v} + \rho_0(\vec{v} \cdot \nabla)\vec{v} = \rho_0\vec{g} - \nabla p + \mu\nabla^2 \vec{v}. \quad (2.29)$$

Here ρ_0 is a constant reference density. The variation in density is written as $\rho = \rho_0 + \Delta\rho$. This results in

$$\partial_t \vec{v} + (\vec{v} \cdot \nabla) \vec{v} = \left(1 + \frac{\Delta\rho}{\rho_0}\right) \vec{g} - \frac{1}{\rho_0} \nabla p + \nu \nabla^2 \vec{v}. \quad (2.30)$$

With ν the kinematic viscosity defined as $\nu = \mu/\rho_0$. We define the reduced pressure $p_r = p + \rho_0 g z$, with gravity pointing in the negative z direction as $\vec{g} = -g \hat{\mathbf{k}}$. With these definitions, the NS equation becomes

$$\partial_t \vec{v} + (\vec{v} \cdot \nabla) \vec{v} = \frac{\Delta\rho}{\rho_0} \vec{g} - \frac{1}{\rho_0} \nabla p_r + \nu \nabla^2 \vec{v}. \quad (2.31)$$

2.6 Stream function and vorticity

The incompressibility condition

$$\nabla \cdot \vec{v} = 0, \quad (2.32)$$

allows the use of a vector potential such that

$$\vec{v} = \nabla \times \vec{\psi}. \quad (2.33)$$

The vector $\vec{\psi}$ is referred to as the stream function. We also define the vorticity vector as

$$\vec{\omega} = \nabla \times \vec{v}. \quad (2.34)$$

The vorticity measures the rotation of the fluid velocity and the stream function is associated with mass continuity in an incompressible flow.

The evolution of the velocity field can be expressed in terms of the stream function and vorticity using appropriate vector identities [102]. Introducing the identity

$$\frac{1}{2} \nabla(\vec{v} \cdot \vec{v}) = (\vec{v} \cdot \nabla) \vec{v} + \vec{v} \times (\nabla \times \vec{v}) \quad (2.35)$$

into the NS equation, and considering the definition of vorticity, we find

$$\partial_t \vec{v} + \frac{1}{2} \nabla(\vec{v} \cdot \vec{v}) - \vec{v} \times \vec{\omega} = \nu \nabla^2 \vec{v} - \frac{1}{\rho_0} \nabla p_r - \frac{\Delta\rho}{\rho_0} g \hat{\mathbf{z}}. \quad (2.36)$$

This NS equation takes into account the Boussinesq approximation for the density term. Taking the curl of this equation, we find an evolution equation for the vorticity. The unknown pressure will be eliminated from the vorticity equation since the rotational of a gradient is zero. We make use of the identity

$$\nabla \times (\vec{v} \times \vec{\omega}) = \vec{v} (\nabla \cdot \vec{\omega}) - \vec{\omega} (\nabla \cdot \vec{v}) + (\vec{\omega} \cdot \nabla) \vec{v} - (\vec{v} \cdot \nabla) \vec{\omega}, \quad (2.37)$$

to account for the curl of $\vec{v} \times \vec{\omega}$ appearing in eq. (2.36). This is further simplified to

$$\nabla \times (\vec{v} \times \vec{\omega}) = (\vec{\omega} \cdot \nabla) \vec{v} - (\vec{v} \cdot \nabla) \vec{\omega}, \quad (2.38)$$

using $\nabla \cdot \vec{v} = 0$ and $\nabla \cdot \vec{\omega} = 0$. Finally, we arrive at

$$\partial_t \vec{\omega} + (\vec{v} \cdot \nabla) \vec{\omega} - (\vec{\omega} \cdot \nabla) \vec{v} = \nu \nabla^2 \vec{\omega} - \nabla \times \left(\frac{\Delta \rho}{\rho_0} g \hat{z} \right). \quad (2.39)$$

This equation, known as the vorticity transport equation, expresses the evolution of the vorticity. We observe that the term involving the viscosity ν has the effect of diffusing the vortices. The vorticity transport equation appears to be a modified advection-diffusion equation with extra terms associated with vortex stretching [103].

We can find a relation between the stream and the vorticity by taking the curl to the definition of the stream function

$$\nabla \times \vec{v} = \nabla \times (\nabla \times \vec{\psi}). \quad (2.40)$$

Using vector identities, this reduces to

$$\vec{\omega} = \nabla(\nabla \cdot \vec{\psi}) - \nabla^2 \vec{\psi}. \quad (2.41)$$

We have arrived at two equations, eqs. (2.39) and (2.41), that completely describe the evolution of the vorticity. These equations allow us to obtain ψ and ω without the need for a pressure term. However, they are coupled, involving nonlinear terms. Another disadvantage is the implementation of boundary conditions, which is not always straightforward in terms of the vorticity.

2.7 Two-dimensional flow

The equations for two-dimensional flow in terms of the vorticity and stream functions allow for a simpler description. The first simplification is the reduction of these functions into scalar fields. Since the velocity field corresponds to $\vec{v} = v_x \hat{x} + v_y \hat{y}$, we only need the z component of the vorticity and stream functions. The stream potential has the form $\vec{\psi} = \psi(x, y) \hat{z}$, it depends only on x and y . The vorticity is also reduced to its z component $\omega = \omega(x, y)$.

The stream function defines a geometric property of the flow. The velocity vectors are tangent to the lines of constant stream ψ defined as streamlines. This fact is readily seen from the definition. For a line of constant ψ we have

$$0 = d\psi = \partial_x \psi dx + \partial_y \psi dy. \quad (2.42)$$

The velocity components are now obtained from $v_x = \partial_y \psi$ and $v_y = -\partial_x \psi$. Therefore, the slope of the streamline is given by

$$\frac{dy}{dx} = -\frac{\partial_x \psi}{\partial_y \psi} = \frac{v_y}{v_x}, \quad (2.43)$$

the ratio of the components of the velocity. Consequently, the velocity field is tangent to the streamlines.

The vorticity is obtained from the definition as $\omega = \partial_x v_y - \partial_y v_x$. Since vorticity and stream functions involve only the z component, we can simplify their relation, eq. (2.41), where

$$\omega \hat{z} = \nabla(\nabla \cdot (\psi \hat{z})) - \nabla^2(\psi \hat{z}). \quad (2.44)$$

The first term is zero, as it is evaluated for this case $\partial_z \psi(x, y) = 0$. Therefore, eq. (2.41) becomes a Poisson equation for the vorticity

$$\omega = -\nabla^2 \psi, \quad (2.45)$$

with the laplacian term in two dimensions. We turn now to simplify the vorticity transport for two-dimensional flow with gravity in the negative y direction

$$\partial_t \omega + (\vec{v} \cdot \nabla) \omega - (\omega \partial_z) \vec{v} = \nu \nabla^2 \omega - \nabla \times \left(\frac{\Delta \rho}{\rho_0} g \hat{y} \right), \quad (2.46)$$

where the density term considers the Boussinesq approximation. In this case, the ∂_z on the velocity also evaluates to zero. Then, we have the equation

$$\partial_t \omega + (\vec{v} \cdot \nabla) \omega = \nu \nabla^2 \omega - \nabla \times \left(\frac{\Delta \rho}{\rho_0} g \hat{y} \right). \quad (2.47)$$

Writing the velocity components in terms of the stream function we arrive to

$$\partial_t \omega + \partial_y \psi \partial_x \omega - \partial_x \psi \partial_y \omega = \nu \nabla^2 \omega - \nabla \times \left(\frac{\Delta \rho}{\rho_0} g \hat{y} \right). \quad (2.48)$$

2.8 Euler equations and Stokes flow

The NS equation can be simplified under viscosity assumptions for the system. One usual assumption is that viscosity dominates the evolution. To be precise, we have to define what it means for viscosity to be large. We introduce a natural system of units for a flow problem with the definition of a length scale L and a time scale T . The process of identifying the correct scales for the problem was introduced by Froude [104] and famously used by Taylor [105, 106]. We use the typical example of flow around an object. The length scale depends on the size

of the object. For a sphere, the length scale L is the diameter. The time scale is obtained indirectly, as it is not available from the problem itself. The flow far away from the object is a uniform field of magnitude $|\vec{v}| = U$. We are interested in how the velocity changes with respect to this reference velocity. The time scale for the problem is defined from the reference velocity as $T = L/U$. Introducing the dimensionless variables

$$\tilde{x} = x/L, \quad \tilde{t} = t/T, \quad \tilde{v}_x = v_x/U, \quad \partial_{\tilde{x}} = L\partial_x. \quad (2.49)$$

We find that the incompressible NS equation without gravity becomes

$$\partial_t \vec{v} + (\vec{v} \cdot \nabla) \vec{v} = -\frac{\Delta p}{\rho_0} \frac{T^2}{L^2} \nabla p_r + \nu \frac{T}{L^2} \nabla^2 \vec{v}. \quad (2.50)$$

Where the tilde has been dropped from all variables and we have introduced a reference pressure difference Δp for the units of \tilde{p}_r . The viscosity factor defines the Reynolds number Re as

$$Re = \frac{LU}{\nu}. \quad (2.51)$$

It is a dimensionless number that describes the influence of viscosity in the flow. It gives a description of the strength of the viscosity independent of units. The dimensionless equation becomes

$$\partial_t \vec{v} + (\vec{v} \cdot \nabla) \vec{v} = -\frac{\Delta p}{\rho_0 U^2} \nabla p_r + \frac{1}{Re} \nabla^2 \vec{v}. \quad (2.52)$$

It is in this dimensionless form where we are able to express the limit cases. If the viscosity dominates the evolution of the systems, the Reynolds number will be low [107]. When this is the case, all the terms of the left hand side are considered small. The pressure term depends on the scale of Δp which is not negligible and should not be discarded as it guarantees the incompressibility condition. We finally arrive at a Poisson equation for the velocity

$$\nabla^2 \vec{v} = -\frac{Re \Delta p}{\rho_0 U^2} \nabla p_r, \quad (2.53)$$

which is known as Stokes flow.

On the other hand, we might be interested in a fluid with low viscosity. This case is represented by a high Reynolds number. As before, the pressure term is kept and the laplacian term in the velocity can be dropped to obtain

$$\partial_t \vec{v} + (\vec{v} \cdot \nabla) \vec{v} = -\frac{\Delta p}{\rho_0 U^2} \nabla p_r. \quad (2.54)$$

This is the Euler equation for fluid flow. Since viscosity is low, we observe that the Euler equations describe a fluid without dissipation of energy.

2.9 Darcy's law

Darcy's law relates fluid velocity with the pressure inside a porous medium. This was originally a phenomenological law for groundwater, nevertheless it can be derived from the NS equation. We outline a derivation for this law. It is assumed, following [108], that the forces of the pore resistance, including the viscosity term, can be represented with a resistive force of the form

$$\vec{R} = -\frac{\mu}{C}\vec{v}. \quad (2.55)$$

Therefore, the NS equation can be expressed as

$$\rho\partial_t\vec{v} + \rho(\vec{v} \cdot \nabla)\vec{v} = -\frac{\mu}{C}\vec{v} + \rho\vec{g} - \nabla p. \quad (2.56)$$

Here the constant C is the pore conductance. Assuming a large viscosity, we can use the same approximations that justified Stokes flow (eq. (2.53)), which in this case lead us to Darcy's law

$$\frac{\mu}{C}\vec{v} = -\nabla p + \rho\vec{g}. \quad (2.57)$$

2.10 Flow in a Hele-Shaw cell

Experimental investigations of two-dimensional flow are carried out using a Hele-Shaw cell. This experimental set-up consists of two parallel flat plates separated by a width d . This width is typically very small to allow to approximate the flow as a two-dimensional fluid within the gap. This array is useful to study fluid flow and instabilities analogous to flow in porous medium [109]. When viscosity is high between the fluids and the plates, the flow in the transverse direction between the plates is similar to Poiseuille flow [110]. Taking the average in the transverse direction, the NS equation can be reduced to

$$\vec{v} = -\frac{d^2}{12\mu}(\nabla p - \rho\vec{g}). \quad (2.58)$$

Resulting in a governing equation for flow in a Hele-Shaw cell. The equation is the same as Darcy's law for porous media replacing the pore conductance with $C = d^2/12$. Other models of flow in a Hele-Shaw cell include the fluid viscosity term

$$\frac{\mu}{C}\vec{v} = -\nabla p + \rho\vec{g} + \mu\nabla^2\vec{v}. \quad (2.59)$$

This model is known as the Brinkmann correction [111].

3 Heat transport

Fluid convection arises from density changes due to compositional or thermal gradients. This temperature distribution will be determined by an advective heat equation. In the context of chemical fronts, a reaction taking place at the front will change the temperature depending on its enthalpy. We are interested in studying the evolution of the temperature because convection will affect the shape and speed of the chemical front. The density of the fluid will change due to the thermal dilation or contraction. Density gradients can cause convection due to buoyancy forces present in the fluid. The temperature evolution of the fluid depends on two mechanisms, fluid advection and heat conduction through matter. The latter is determined by Fourier's law of conduction. It describes how heat flows from a high temperature region to a lower temperature region. In this chapter, we develop a heat equation based on this law. For an object at a different temperature with respect to the medium, we will need to describe the heat flow across its boundaries, leading to Newton's cooling law. These equations combined will lead to a diffusion equation for the temperature distribution within the fluid's volume, using appropriate boundary conditions.

3.1 Fourier's Law

Objects at a temperature different from the room temperature will evolve to an equilibrium state. Such equilibrium is attained when there is no thermal flux between the object and the environment. Heat flows from higher to lower temperature according to Fourier's law

$$\vec{q} = -k\nabla T. \quad (3.1)$$

Where the heat flux q is the heat rate per unit area, and k is the thermal conductivity. The property k is assumed to be constant, but it may depend on the temperature gradient ΔT , and the type of material [112].

3.2 Newton's cooling law

Newton's cooling law describes an object in a heat bath of room temperature T_∞ [113]. The heat bath has the property of keeping the room temperature constant. It is considered as the temperature on a region far away from the object. As a simplifying assumption, we consider that the temperature profile of the object is uniform. Its temperature is described by a single value of T which may depend on time. We also ignore the convective transfer of temperature with the surrounding medium. The change of the internal energy of an object can be calculated

accounting for the heat flux through its surface. According to Fourier's law we have

$$\frac{d}{dt}U = \int \vec{q} \cdot d\vec{A} = -\bar{h}A(T - T_\infty). \quad (3.2)$$

Where \bar{h} is a transfer coefficient which depends on the specific characteristics of the problem, such as geometry, materials and heat diffusion in the domain. The object has surface area A . Assuming that the internal energy depends linearly on the temperature, we arrive to Newton's cooling law

$$\rho cV \frac{d}{dt}T = -\bar{h}A(T - T_\infty). \quad (3.3)$$

With ρ the density of the object and V its volume. The relation between energy and temperature is described by the specific heat capacity at constant volume c . This equation can be solved by introducing a dimensionless variable θ such that $T = T_\infty(1 + \theta)$. The resulting equation for θ is

$$\frac{d}{dt}\theta = -\frac{\bar{h}A}{\rho cV}\theta. \quad (3.4)$$

For the time $t = 0$ we consider an initial known value θ_0 , and the differential equation is solved in terms of the exponential function

$$\theta = \theta_0 \exp\left(-\frac{\bar{h}A}{\rho cV}t\right). \quad (3.5)$$

The evolution for θ gives the following result for the temperature

$$T = T_\infty \left(1 + \theta_0 \exp\left(-\frac{\bar{h}A}{\rho cV}t\right)\right) \quad (3.6)$$

Therefore, the temperature decreases exponentially towards the room temperature.

3.3 Heat diffusion-advection in a fluid

We will now describe the evolution of temperature distribution within an object. For this, we set up a volume element and the heat equation on this element. There is heat transfer from this volume element to the outside according to Fourier's law. The heat transfer is measured in terms of the specific internal energy u which measures the energy per unit mass. This internal energy can change only due to changes in temperature $du = cdT$. This approach is valid for incompressible fluids. The Fourier law for a volume element with surface S

$$\frac{d}{dt}U = \frac{d}{dt} \left(\int \rho u dV \right) = - \int (-k\nabla T) \cdot d\vec{A} \quad (3.7)$$

The time derivative is calculated with Reynold's transport theorem (eq. (1.7)), changing the surface integral into a volume integral with the help of Gauss's theorem. We obtain the following equation

$$\int (\partial_t(\rho u) + \nabla \cdot (\rho u \vec{v})) dV = \int (\nabla \cdot (k \nabla T)) dV. \quad (3.8)$$

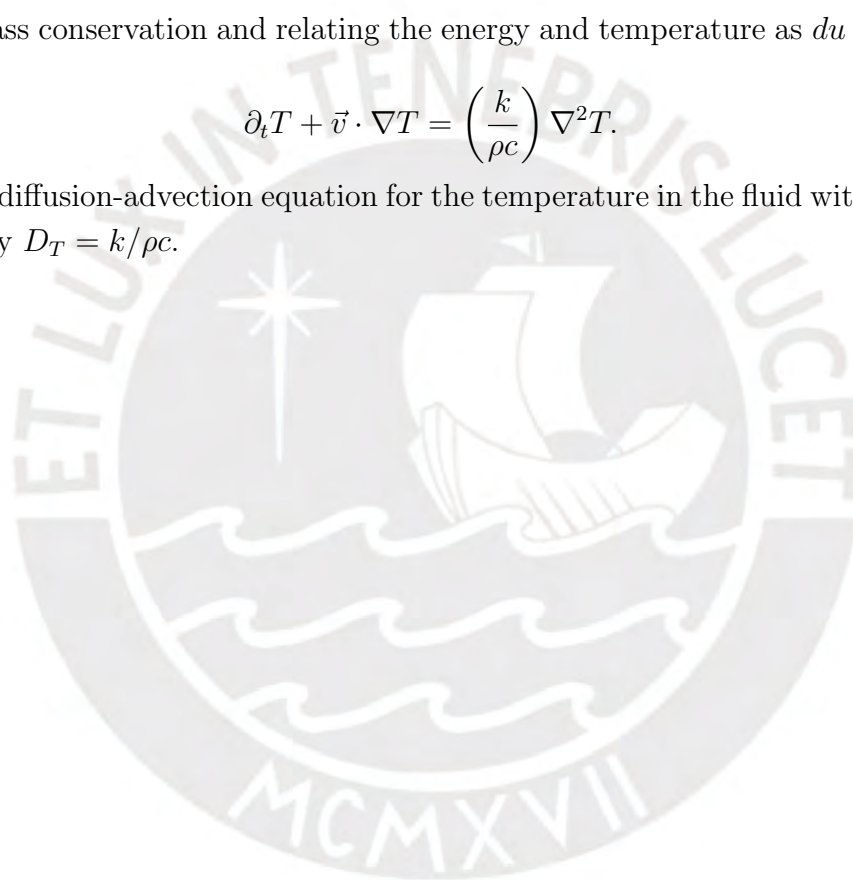
Here \vec{v} is the fluid velocity field, and k the conduction coefficient considered a constant. We obtain a local equation which is valid for any volume element dV as

$$\partial_t(\rho u) + \nabla \cdot (\rho u \vec{v}) = k \nabla^2 T. \quad (3.9)$$

Using mass conservation and relating the energy and temperature as $du = cdT$ we obtain

$$\partial_t T + \vec{v} \cdot \nabla T = \left(\frac{k}{\rho c} \right) \nabla^2 T. \quad (3.10)$$

This is a diffusion-advection equation for the temperature in the fluid with thermal diffusivity $D_T = k/\rho c$.



4 Chemical reaction fronts

In this thesis, we study the evolution of chemical reaction fronts in fluids. We are interested in the interaction between fluid flow and the propagation of reaction fronts. Thus, we develop a theory that couples the reaction-diffusion mechanisms with the dynamics of the heat and momentum transfer of the fluid. An early reaction-diffusion mechanism, describing front propagation without advection, led to the Fisher-Kolmogorov-Petrovsky-Piskunov (FKPP) equation. In reaction-diffusion equations, the concentration transport is described by Fick's law, which is analogous to Fourier's law for temperature. Similarly, Fick's law leads to a diffusion equation for the concentration. Additionally, the concentration of the substance may change due to chemical reactions. The reactive term is what allows for the front dynamics observed in the FKPP equation and other models that followed. In the FKPP model, the reaction term is a quadratic equation joining two steady states. In other systems, such as the iodate-arsenous acid reaction, the model requires a cubic reaction term. These types of reaction-diffusion models require the solution of three-dimensional PDEs for the concentration. An alternative model is to describe the front as an infinitesimally thin interface between reacted and unreacted fluids. This description requires the evolution of a surface, instead of providing the chemical concentration everywhere in the fluid. For example, fronts in the IAA reaction can be modeled with an eikonal relation between the normal front velocity and its curvature. This model is independent of the underlying chemical mechanisms. In other systems, differences in diffusivity between chemical species gives rise to instabilities in the shape and speed of the front. Nevertheless, they can be modeled by the Kuramoto-Sivashinsky (KS) equation, which is a nonlinear fourth order front evolution equation. This equation also appears in the propagation of flame fronts in combustion, allowing for the description of front instabilities.

4.1 Chemical transport by diffusion

Diffusion helps us describe the transport of the concentration of molecules. A high concentration of molecules in a small region of space is thermodynamically unstable due to the high entropy of the distribution. This observation led Fick to establish the law for the flux \vec{J} of concentration c

$$\vec{J} = -D\nabla c, \quad (4.1)$$

where D is a diffusivity constant which depends on the medium where the molecules are free to travel [114]. This is the main process to consider when other external

transport mechanisms are absent, such as advection or external forces like electric fields. The law of mass conservation provides the second Fick's law for the evolution of the concentration c . The change of number of molecules in a test volume depends on the flux outside of this volume as

$$\frac{d}{dt} \int c dV = - \int \vec{J} \cdot d\vec{S}. \quad (4.2)$$

This is equivalent to the mass conservation law in terms of number of molecules. The surface integral of the flux changes to a volume integral with the use of Gauss's theorem, we have

$$\int \partial_t c dV = - \int \nabla \cdot \vec{J} dV. \quad (4.3)$$

Here we do not consider the possibility of advection. For an arbitrary volume element, we get a local equation for the concentration

$$\partial_t c = \nabla \cdot (D \nabla c), \quad (4.4)$$

which corresponds to Fick's second law, also known as the diffusion equation [115]. When the diffusivity is constant, we get the commonly used form of the equation as

$$\partial_t c = D \nabla^2 c. \quad (4.5)$$

This model can also be obtained by considering random walks of the molecules [116]. This allows us to interpret the diffusion coefficient in terms of the microscopic properties of molecular dynamics.

4.2 Quadratic FKPP front equation

Propagating fronts depend on diffusion and a specific reaction mechanism. One of the earliest reactions considered was a model introduced by Fisher to analyze the propagation of a gene in a population [117, 118]. This model involved a quadratic reaction term. Kolmogorov, Petrovskii, and Piskunov studied a similar problem [119]. In the study of chemical waves, we find a two variable quadratic model describing front propagation in the Belousov-Zhabotinsky (BZ) reaction [30]. A reaction-diffusion model for a chemical concentration c considers a function $f(c)$ that describes the reaction mechanism

$$\partial_t c = D \nabla^2 c + f(c). \quad (4.6)$$

As a first example, we consider the FKPP model that involves a quadratic reaction term

$$\partial_t c = D \nabla^2 c + c(1 - c). \quad (4.7)$$

This equation is considered the first model that showed reaction diffusion fronts. The reaction term is similar to the logistic map, which describes the evolution of population subject to a limiting growth factor. Theoretical studies developed analytical forms of solutions for this equation [120, 121]. While this equation arises from population dynamics, R. Luther was the first to propose similar ideas for the propagation of chemical waves [122].

4.3 Cubic autocatalytic reaction front

Another important reaction-diffusion model involves a cubic autocatalytic reaction mechanism. This model explained the conditions for front propagation in the iodate-arsenous acid (IAA) reaction [26]. The equation for a cubic autocatalytic reaction front describing the evolution of the concentration field c in one dimension is

$$\partial_t c = D\partial_x^2 c + \alpha c^2(1 - c). \quad (4.8)$$

The exact distribution of concentration and speed of the front can be obtained by solving the equation for c . We begin by using a reference frame moving with the front. In this frame the concentration is a steady state described by

$$-v\partial_x c = D\partial_x^2 c + \alpha c^2(1 - c), \quad (4.9)$$

where v is the front speed. We consider boundary conditions as $c = 1$ at $x \rightarrow -\infty$ and $c = 0$ at ∞ . This corresponds to having fresh reactants ($c = 0$) far ahead of the front, and products ($c = 1$) far behind. With these conditions, the concentration of products moves towards the positive x axis as the reaction consumes the reactants. We follow the solution as in [28]. Introducing a new variable $G = dc/dx$, eq. (4.9) becomes

$$-vG = DGG' + \alpha c^2(1 - c). \quad (4.10)$$

We substitute the function G using a power series in c of the form $G = \sum a_n c^n$. Because the equation includes terms of at most c^3 , the power series must terminate at degree $n = 2$. This makes the factor GG' a third degree polynomial, therefore G has the form

$$G(c) = a_0 + a_1 c + a_2 c^2, \quad (4.11)$$

which can be simplified by considering that the value of c does not change in regions away from the front. This implies that the function G must be zero far away from the front, thus

$$G = g(1 - c)c, \quad (4.12)$$

with g an undetermined scalar. We introduce this form of G into the original differential equation. Factoring out the $(1 - c)c$ terms, we get an equation for the coefficients

$$0 = (Dg^2 + vg) + c(\alpha - 2Dg^2). \quad (4.13)$$

In this equation, the terms in parentheses must be zero. Since we assume that the front moves in the positive x direction ($v > 0$), this results in a front speed

$$v = \sqrt{\frac{\alpha D}{2}}, \quad (4.14)$$

with the function G being

$$G = \sqrt{\frac{\alpha}{2D}}(c - 1)c. \quad (4.15)$$

Since G is the derivative of c , we obtain after doing the integration

$$c(x) = \frac{1}{1 + \exp(\sqrt{\frac{\alpha}{2D}}(x - x_0))}. \quad (4.16)$$

This is the concentration profile in the moving reference frame. In two dimensions, curved fronts will show dependence on y and z , which may be unstable states for this system. In the presence of fluid flow, these fronts obey a reaction-diffusion-advection equation that involves the local fluid velocity \vec{v}

$$\partial_t c + \vec{v} \cdot \nabla c = D\nabla^2 c + \alpha c^2(1 - c). \quad (4.17)$$

The flat front solution corresponds to the one-dimensional solution discussed above. In this thesis, we study the stability of these flat fronts interacting with gravitationally driven fluid motion.

4.4 Fronts in the IAA reaction

The cubic autocatalytic reaction-diffusion equation describes the evolution of fronts in the IAA reaction. The reaction describes the oxidation of arsenous acid by iodate



This form of the reaction takes place when the concentration of arsenous acid is much higher than the concentration of iodate. The kinetics of this reaction follows a combination of the kinetics of the Dushman and Roebuck reactions [26, 123]. The evolution of the normalized iodide (I^-) concentration $c = [\text{I}^-]/[\text{IO}_3^-]$ in one dimension is given by

$$\partial_t c = D\partial_x^2 c + \alpha c(c + c_s)(1 - c). \quad (4.19)$$

A typical value of the constant c_s is 0.0027, which is small and can be ignored [41]. The theoretical characterization of the fronts with and without c_s are equivalent when $c_s < 0.5$ [124]. The experimental front speed for this reaction is about $23.6\mu\text{m/s}$, in agreement with the theoretical value [26]. The presence of advection changes the shape and speed of the front as observed in experiments [40].

4.5 Thin front approximation

Experiments and theory for fronts in the IAA reaction show that the region separating reacted from unreacted substances is very thin. For flat fronts, this region is quantified defining a mixing length as the distance between the positions where $c = 0.01$ and $c = 0.99$ across the front [125]. Using the analytic solution for a cubic front, the mixing length can be estimated to be about $L_m = 13\sqrt{D/\alpha}$. The value of α can be estimated from the experimental flat front speed. The diffusion coefficient D corresponds to the molecular diffusivity of water. The width of the region is approximately 0.06cm for the parameters of the IAA reaction [126]. If this transverse length is smaller than the longitudinal wave of the front or other dimensions in the experiment, we may consider the front as being infinitesimally thin. This interface corresponds to a mathematical surface in three-dimensional space. The problem of front propagation requires the solution of the chemical concentration c all over the space. Using a thin front approximation, we focus on a level set surface that describes the front. Fronts that are nearly flat can be described by a height function H . If the front propagates along the z direction, we can write the height function as $z = H(x, y, t)$, describing the surface that separates reacted from unreacted fluids. The evolution of the height has been studied in the context of propagation of front instabilities [127]. A very useful approximation for fronts in the IAA reaction and the BZ reaction is the eikonal relation. This relation provides a normal front velocity as a function of the flat front speed and its curvature [128, 129]. This approximation has been useful in predicting convective instabilities due to a density discontinuity across the front [126]. The results of the thin front approximation compare well to results obtained using a reaction-diffusion equation for front propagation [130, 58, 131].

We show an outline of a derivation for the eikonal relation in the context of reaction-diffusion fronts [132]. Consider the most general relation

$$\partial_t c = D\nabla^2 c + f(c). \quad (4.20)$$

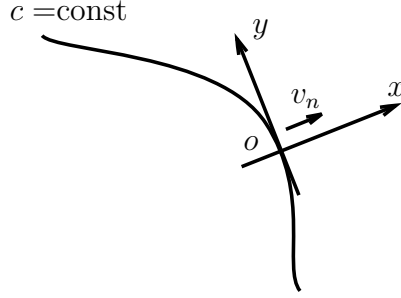


Figure 1: Coordinate system, with origin o , on a level set that represents the convex chemical front propagating with normal speed v_n .

For simplicity, we only consider propagation in a two dimensional domain. The coordinate system with origin o is shown in fig. 1. The direction of x is normal to the front and y is along a tangent. As a first approximation, the front is considered to be nearly flat. The local evolution in the flat front approximation is

$$\partial_t c = D \partial_x^2 c + f(c). \quad (4.21)$$

We set a moving frame o' moving with the flat front speed v_0 . Therefore, the equation becomes

$$\partial_t c = v_0 \partial_{x'} c + D \partial_{x'}^2 c + f(c). \quad (4.22)$$

In this reference frame, the concentration does not change with time, then

$$-v_0 \partial_{x'} c = D \partial_{x'}^2 c + f(c). \quad (4.23)$$

The first correction to the flat front approximation follows from considering a slight curvature to the front.

The front is approximated with a circle of radius R related to the local curvature κ of the front. This is defined as the osculating circle and the radius is related to the curvature as $R = |\kappa|^{-1}$. In fig. 2, the coordinate system o'' is set at the center of the circle. Using polar coordinates centered in o'' the evolution of the concentration is given by

$$\partial_t c = D (\partial_r^2 c + r^{-2} \partial_\theta^2 c + r^{-1} \partial_r c) + f(c). \quad (4.24)$$

Around the original coordinate system o , centered at the level set, the equation can be described with $r = R$. The equation is equivalent to

$$\partial_t c = D (\partial_x^2 c + |\kappa| \partial_x c + |\kappa|^2 \partial_\theta^2 c) + f(c). \quad (4.25)$$

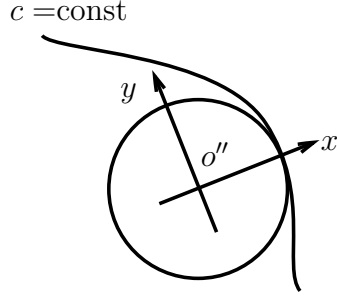


Figure 2: Coordinate system centered in the osculating circle for a convex front.

Assuming small curvatures, we can neglect terms of order $|\kappa|^2$ and higher. This leads to

$$\partial_t c = D (\partial_x^2 c + |\kappa| \partial_x c) + f(c). \quad (4.26)$$

We can rewrite this equation as

$$\partial_t c - D|\kappa| \partial_x c = D\partial_x^2 c + f(c), \quad (4.27)$$

which shows that the curvature acts like an advective term. This front moves with speed v_n . In the reference frame moving with the slightly curved front, we have

$$-v_n \partial_x c - D|\kappa| \partial_x c = D\partial_x^2 c + f(c). \quad (4.28)$$

The right hand side is related to the flat front speed from eq. (4.23). This results in the eikonal relation for the normal velocity

$$v_n = v_0 - D|\kappa|. \quad (4.29)$$

This equation has been derived for a convex front, we will assume the convention followed by Edwards [126], where they assume that the center of curvature is in the unreacted fluid. Therefore, since $|\kappa| = -\kappa$, the equation becomes

$$v_n = v_0 + D\kappa. \quad (4.30)$$

Here, v_0 is the speed of the flat front, D corresponds to the diffusivity and κ is the curvature. In this case, the curvature decreases the normal velocity of the front because diffusion in the tangential direction tends to flatten the front.

The eikonal relation is used to construct an equation for the evolution of the height function $H = H(x, t)$ in the presence of fluid velocity \vec{v} . The normal front velocity v_n relative to the moving fluid is related to H as

$$v_n = \hat{n} \cdot \hat{y} \partial_t H - \hat{n} \cdot \vec{v}. \quad (4.31)$$

Using the eikonal approximation (eq. (4.30)), we have

$$\hat{n} \cdot \hat{y} \partial_t H = v_0 + D\kappa + \hat{n} \cdot \vec{v}. \quad (4.32)$$

In two dimensions, we consider a normal vector to the height function $H(x, t)$ as

$$\hat{n} = \frac{\hat{y} - \hat{x} \partial_x H}{\sqrt{1 + (\partial_x H)^2}}, \quad (4.33)$$

and the local curvature can be calculated in terms of H as

$$\kappa = \frac{\partial_x^2 H}{(1 + (\partial_x H)^2)^{3/2}}. \quad (4.34)$$

Then we arrive at the following evolution equation for the front height

$$\partial_t H = v_0 (1 + (\partial_x H)^2)^{1/2} + D \frac{\partial_x^2 H}{1 + (\partial_x H)^2} + v_y - v_x \partial_x H. \quad (4.35)$$

We can further simplify this equation by considering that the front curves only slightly, therefore $\partial_x H$ is small. In this approximation, we keep terms up to order $(\partial_x H)^2$ to obtain

$$\partial_t H = v_0 + D \partial_x^2 H + \frac{v_0}{2} (\partial_x H)^2 + v_y - v_x \partial_x H. \quad (4.36)$$

This evolution, without fluid flow, has the form of a deterministic Kardar-Parisi-Zhang (KPZ) equation [133].

4.6 Thin front KS equation

In the previous description, it was assumed that the reaction can be represented by a uniform diffusivity D , independent of the chemical species. However, reactions may involve two or more chemical species with different diffusivities. This may lead to instabilities, such as the case of the Turing instability [8]. Different diffusivities can also lead to front instabilities, such as the case of the IAA reaction inside gels [61]. This system can be studied using reaction-diffusion equations, but it can also be described with a thin front approximation. In this case, the front evolves following the Kuramoto-Sivashinsky (KS) equation [63, 134, 110]. In terms of the height function H , the KS equation in a moving fluid corresponds to

$$\partial_t H = v_0 + \mathcal{V} \partial_x^2 H - \mathcal{K} \partial_x^4 H + \frac{v_0}{2} (\partial_x H)^2 + \hat{n} \cdot \vec{v} \quad (4.37)$$

The value of \mathcal{V} can be either positive or negative. Its value, as well as the value of \mathcal{K} , depends on the details of the reaction. The height function describes a flat front solution of speed v_0 and includes advection of the fluid with velocity \vec{v} . The

sign of \mathcal{V} determines the instability of the flat front solution in the absence of convection. The diffusive term stabilizes the solutions when it is positive, as in the case of the diffusion equation. However, when it is negative, the term acts as a feedback term which makes places with high concentration to accumulate even more concentration. In the KS equation, the negative diffusion is stabilized by the fourth derivative term. The competition of these two mechanisms depends on the wavelength of the perturbations, resulting in instabilities for large wavelengths. The KS equation describes a stable flat fronts in confined domains. It can also show steady patterns, oscillatory fronts, and spatiotemporal chaos [135].

4.7 Temperature distribution for a thin flat front

In the thin front approximation, the temperature distribution for a flat front moving with constant velocity can be obtained in analytic form. In this case, a one dimensional equation describes the temperature of the medium as the concentration c varies

$$\partial_t T = D_T \partial_x^2 T + Q f(c). \quad (4.38)$$

This is described in terms of two constants, the thermal diffusivity $D_T = k/\rho\tilde{c}$ and $Q = \Delta U/\rho\tilde{c}\Delta t$. Where k is the conductivity, ρ the density, \tilde{c} the specific heat capacity, and $\Delta U/\Delta t$ is the heat rate given by the reaction. The thin front approximation assumes that the reaction takes place exactly at the location of the height function $H(x, t)$. This is modeled using a delta function centered at the front as the heat source

$$\partial_t T = D \partial_x^2 T + Q \delta(x - H). \quad (4.39)$$

We use a moving reference frame with speed equal to v_0 , the flat front speed. These coordinates transform as $x' = x - v_0 t$, with $H = v_0 t$. Accordingly, we transform the differential equation (eq. (4.39)) and drop the primes for convenience

$$-v_0 \partial_x T = D \partial_x^2 T + Q \delta(x). \quad (4.40)$$

As the front travels, it heats the fluid behind it. Far behind the front the boundary condition will consider no heat flow $\partial_x T = 0$. On the other extreme of the domain, we consider that the fresh unreacted fluid is at an ambient temperature T_0 . The equation eq. (4.40) is equal to

$$-v_0 \partial_x T = D \partial_x^2 T, \quad (4.41)$$

everywhere except at $x = 0$, due to the Dirac delta function. The delta function introduces a discontinuity at $x = 0$. We obtain the discontinuity integrating

eq. (4.39) from $x = -\epsilon$ to $x = \epsilon$, with $\epsilon \rightarrow 0$, leading to

$$-v[T] = D[\partial_x T] + Q. \quad (4.42)$$

Here $[f] = (f_+ - f_-)$, with f_+ and f_- are the functions evaluated just above and just below $x = 0$ respectively. The general solution of eq. (4.41) is

$$T(x) = A + B \exp\left(-\frac{v}{D}x\right), \quad (4.43)$$

with A and B arbitrary constants, which can be different in each part of the domain. For $x < 0$ we require a bounded solution, therefore

$$T_- = A. \quad (4.44)$$

For $x > 0$, the ambient temperature condition gives the solution for T_+ as

$$T_+ = T_0 + B \exp\left(-\frac{v}{D}x\right). \quad (4.45)$$

Since the temperature is continuous, we have $[T] = 0$. Using the discontinuity of the derivative from eq. (4.42), we have

$$[\partial_x T] = \left(-B\frac{v}{D} - 0\right) = -\frac{Q}{D}. \quad (4.46)$$

The full solution for $T(x)$ is

$$T(x) = \begin{cases} T_0 + \frac{Q}{v} & x < 0 \\ T_0 + \frac{Q}{v} \exp\left(-\frac{v}{D}x\right) & x \geq 0 \end{cases} \quad (4.47)$$

In this solution, we find that the temperature behind the front is higher by $\Delta T = Q/v$. This relation allows the identification of Q with the temperature.

4.8 Front propagation with heat loss

4.8.1 Equations of motion

We study the propagation of a chemical reaction front in a liquid confined in a two dimensional rectangular domain resembling a narrow tube. This domain is placed vertically, with the acceleration of gravity pointing in the negative y direction. In this chapter, we will study both vertical and horizontal propagation. In the former, the front propagates upwards against gravity and, in the latter, the front propagates sideways along the length of the domain.

As the front propagates inside the fluid, the chemical concentration $c(x, y, t)$ follows an advection-reaction-diffusion equation. In this chapter, we consider a cubic

reaction term describing fronts in the IAA reaction [136, 137]. For the corresponding equation

$$\partial_t c + \vec{V} \cdot \nabla c = D \nabla^2 c + \alpha c^2 (1 - c), \quad (4.48)$$

an initial concentration $c = 0$ becomes a normalized concentration $c = 1$ as the front propagates [138]. The parameter D is the diffusion coefficient for the chemical reactants, and α measures the chemical reaction rate. The advection term couples the reactant concentration with the fluid velocity \vec{V} . In the absence of fluid flow, the equation has an analytical solution describing a flat front propagating with constant speed $v_f = \sqrt{D\alpha/2}$ [136].

The fluid temperature $T(x, y, t)$ changes across the front due to heat released by the reaction. In our model, we consider a thermal advection-diffusion equation with a heat source generated by the reaction. The corresponding equation is

$$\partial_t T + \vec{V} \cdot \nabla T = D_T \nabla^2 T + Q c^2 (1 - c), \quad (4.49)$$

where D_T is the thermal diffusivity and Q measures the amount of heat released by the reaction [136].

The fluid velocity $\vec{V}(x, y, t)$ evolves due to buoyancy forces caused by density gradients. In the Boussinesq approximation, the density changes affect only the large gravity term [139]. Consequently, the fluid velocity is determined by the Navier-Stokes equation

$$\partial_t \vec{V} + \vec{V} \cdot \nabla \vec{V} = \nu \nabla^2 \vec{V} - \frac{1}{\rho_0} \nabla P - \frac{\rho}{\rho_0} g \hat{y}, \quad (4.50)$$

and the continuity equation for velocity

$$\nabla \cdot \vec{V} = 0. \quad (4.51)$$

Here ν is the kinematic viscosity and ρ_0 is the density of the fluid at constant ambient temperature T_0 . The density depends on the temperature as $\rho = \rho_0(1 - \alpha_T(T - T_0))$, where α_T is the coefficient of thermal expansion. Introducing the temperature dependence and the reduced pressure $P_r = P + \rho_0 g y$, we get the equation

$$\partial_t \vec{V} + \vec{V} \cdot \nabla \vec{V} = \nu \nabla^2 \vec{V} - \frac{1}{\rho_0} \nabla P_r + \alpha_T g (T - T_0) \hat{y}. \quad (4.52)$$

We analyze the equations introducing dimensionless variables arising from the chemical properties of the front. The unit of length corresponds to $L = \sqrt{D/\alpha}$ and the unit of time is $\tau = 1/\alpha$. In these units, the dimensionless velocity is $\vec{v} = \tau \vec{V}/L$.

Therefore, the corresponding dimensionless advection-reaction-diffusion equation becomes

$$\partial_t c + \vec{v} \cdot \nabla c = \nabla^2 c + c^2(1 - c). \quad (4.53)$$

For the local fluid temperature, we introduce a dimensionless variable θ such that $T = T_0 + \Delta T \theta$. The factor $\Delta T = Q\tau$ corresponds to the temperature difference between reacted and unreacted fluid for a flat convectionless front. With these variables, the evolution for the dimensionless temperature θ becomes

$$\partial_t \theta + \vec{v} \cdot \nabla \theta = \text{Le} \nabla^2 \theta + c^2(1 - c). \quad (4.54)$$

Where $\text{Le} = D_T/D$ is the Lewis number. The Navier-Stokes equation (4.52) becomes

$$\partial_t \vec{v} + \vec{v} \cdot \nabla \vec{v} = \text{Sc}(\nabla^2 \vec{v} - \nabla \tilde{P} + \text{Ra} \theta \hat{y}). \quad (4.55)$$

Here Sc and Ra are two dimensionless numbers defined as the Schmidt number $\text{Sc} = \nu/D$ and the Rayleigh number $\text{Ra} = D\alpha_T g \Delta T \tau^2 / \nu L$. The dimensionless reduced pressure \tilde{P} is measured in units of $\nu \rho_0 / L \tau$. We consider a system where the Schmidt number is large [126], therefore equation (4.68) simplifies to the Stokes equation

$$\nabla^2 \vec{v} = \nabla \tilde{P} - \text{Ra} \theta \hat{y}. \quad (4.56)$$

Because of the continuity equation (4.51), we can introduce a stream function ψ , such that the components of the velocity correspond to $v_x = \partial_y \psi$, and $v_y = -\partial_x \psi$. Defining a vorticity function ω such that

$$\nabla^2 \psi = -\omega, \quad (4.57)$$

will allow us to eliminate the pressure by taking the curl of equation (4.56). This leads to an equation for the vorticity involving the dimensionless temperature

$$\nabla^2 \omega = -\text{Ra} \partial_x \theta. \quad (4.58)$$

The evolution of the system obeys equations (4.53), (4.54), (4.57) and (4.58) simultaneously. In this model, we set stress free boundary conditions for the fluid velocity, this allows us to make the stream function and the vorticity equal to zero at the boundaries.

The reaction front propagates along the length of a narrow rectangular domain. The boundary conditions for the concentration correspond to reacted fluid $c = 1$ behind the front and fresh reactants $c = 0$ ahead of the front. For the long sides

across the width of the domain, there is no concentration flow. Therefore, the normal derivatives of the concentration are zero $\partial_n c = 0$.

For the temperature, we consider a constant room temperature $\theta = 0$ at the domain side ahead of the front, and no heat flow $\partial_n \theta = 0$ on the side behind the front. On the long sides confining the fluid layer, we allow for heat losses through the walls, leading to conductive boundary condition for T

$$-k\partial_n T = h(T - T_0), \quad (4.59)$$

where the normal n direction points outside of the domain. This equation characterizes transfer of heat using a conductivity k and a transfer coefficient h [140]. In dimensionless units, this boundary condition becomes

$$-\partial_n \theta = \text{Bi}\theta. \quad (4.60)$$

This equation introduces a dimensionless Biot number $\text{Bi} = hL/k$. The boundary condition describes insulating walls when $\text{Bi} = 0$, with no heat flowing to the environment. For large values of Bi , the high conductivity will fix the temperature at the walls to the ambient temperature. In the case of insulating walls without convection, the temperature changes across the front, depending only on the length of the domain, without gradients in the transverse direction. In contrast, for conducting walls, the temperature near the front will be higher halfway between the walls. As the front propagates, the temperature far behind the front is constant, having a higher temperature for insulating walls, while having a temperature equal to the ambient temperature otherwise.

4.8.2 Numerical methods

We solve the governing equations using a finite difference approximation for the spatial derivatives in a rectangular grid. To describe a front propagating in the vertical direction, we use a rectangular domain with a narrow horizontal width. Cartesian coordinates are set with the x axis along the horizontal direction, and the acceleration of gravity pointing in the negative y direction. We define the axis as the line parallel to the length of the domain going through the center of the rectangle. The relatively high value of the thermal diffusivity requires the use of a large domain in the direction of propagation, therefore its length is set to $L_p = 1050$. We vary the width on the transverse direction to study convection for different dimensions of the domain. Vertical propagation corresponds to propagation along the length of the domain in the y direction, while the x direction becomes the transverse direction. For horizontal propagation, the rectangle is rotated such that the x axis is now along its length. The domain is discretized with

uniform grid size $\Delta x = \Delta y = 0.35$. The evolution is carried out using an Euler algorithm with $\Delta t = 0.01$. We use a five point discretization for the laplacian, which is accurate to order Δx^2 . The Euler algorithm is of order Δt . To avoid numerical instabilities from the advective terms, we implement an upwind scheme of order Δx . For the numerical instabilities arising from the diffusive term, we use an alternate direction implicit (ADI) method for the evolution of the temperature and the chemical concentration [90]. We tested the results for different values of Δx and Δt without much variation in the front velocities. A relaxation technique provides solutions for the stream function and vorticity, eqs. (4.57) and (4.58) respectively. For insulating walls, we use as the initial condition for the concentration the analytic solution of eq. (4.53) for a flat front without convection [141], while for the temperature we use an exponential decay function based on a thin front approximation [126]. To allow the fronts to reach an asymptotic state, we let them propagate for a small finite time and shift the front backwards, keeping its average position away from the top and bottom boundaries. After shifting the front, we fill the top of the domain with unreacted fluid at the ambient temperature. In this manner, we avoid interactions between the front and the fixed boundaries. For highly conductive walls, a zero temperature initial condition is set because heat losses lead to a low temperature state. The stability of the flat front is tested by adding random small perturbations to the variables near the front. In this chapter, we fix the value of the Rayleigh number to $Ra = 0.2$, estimated from constants in IAA experiments [126]. In all calculations, the corresponding value of the Lewis number is set to $Le = 72$ [126]. As Biot numbers are varied successively, the solutions previously obtained become the initial conditions for a new Biot number.

4.9 Thin front with thermal and compositional gradients

4.9.1 Equations of motion

In this chapter, we consider a thin reaction front propagating in a two-dimensional fluid. The spatial domain is described using Cartesian coordinates with the x axis along the horizontal direction and the y axis pointing in the upward vertical direction. A height function $H = H(x, t)$ describes the position of the front at time t , without fluid motion the normal front velocity C_n is a function of H and its derivatives. When fluid motion is present, the normal fluid velocity adds to C_n . Here, we study fronts described by the Kuramoto-Sivashinsky (KS) equation in the presence of fluid flow

$$\partial_t H = C_0 + \mathcal{V} \partial_x^2 H - \mathcal{K} \partial_x^4 H + \frac{C_0}{2} (\partial_x H)^2 + \hat{n} \cdot \vec{V}|_{y=H}, \quad (4.61)$$

with the fluid velocity \vec{V} evaluated at the front. Here \hat{n} corresponds to the unit normal vector to the front and C_0 is the convectionless flat front speed. In this equation, the values of \mathcal{V} and \mathcal{K} depend on the specific characteristics of the physical system. For fronts exhibiting diffusive instabilities, these parameters involve reaction rates and different diffusion coefficients. [63] We focus our work on instabilities that take place when the coefficient \mathcal{V} is negative.

Density gradients near the propagating front can lead to convective fluid motion. We describe the velocity field using the Navier-Stokes equation in the Boussinesq approximation

$$\partial_t \vec{V} + \vec{V} \cdot \nabla \vec{V} = \nu \nabla^2 \vec{V} - \frac{1}{\rho_0} \nabla P - \frac{\rho}{\rho_0} g \hat{y}, \quad (4.62)$$

with mass conservation given by

$$\nabla \cdot \vec{V} = 0. \quad (4.63)$$

Where ν is the kinematic viscosity of the fluid and ρ is the density of the fluid. In our system, we consider small density variations with respect to a reference density ρ_0 . The density of the fluid is affected by the fluid temperature $T(x, y, t)$ and the composition of the reactants. In this chapter, we assume that the fluid density depends linearly on the temperature through an expansion coefficient α_T . [126] The front separates reacted from unreacted fluids of different composition, resulting in an additional density difference $\Delta\rho = \alpha_C \rho_0$ across the front. The equation for the density ρ becomes

$$\rho = \rho_0(1 - \alpha_T(T - T_0) + \alpha_C \Theta(y - H)). \quad (4.64)$$

Here $\Theta(y)$ is the Heaviside unit step function, taking the value of 1 when $y > 0$ and 0 otherwise. [81] Inserting this expression for the density in Eq. 4.62 we obtain

$$\partial_t \vec{V} + \vec{V} \cdot \nabla \vec{V} = \nu \nabla^2 \vec{V} - \frac{1}{\rho_0} \nabla P_r + \alpha_T g (T - T_0) \hat{y} - \alpha_C g \Theta(y - H) \hat{y}. \quad (4.65)$$

In this equation, we introduced the reduced pressure $P_r = P + \rho_0 g y$. Since the chemical reaction releases or absorbs heat at the front, the temperature obeys a heat diffusion-advection equation with a source term proportional to a Dirac delta function centered at the front $y = H$

$$\partial_t T + \vec{V} \cdot \nabla T = D_T \nabla^2 T + Q \delta(y - H). \quad (4.66)$$

Here D_T corresponds to the thermal diffusivity and Q is proportional to the amount of heat required for the temperature change ΔT behind a convectionless front. The value of Q corresponds to $C_0 \Delta T$.

We use dimensionless variables using a length scale $L = D_T/C_0$ and a time scale $\tau = D_T/C_0^2$. The temperature is measured using a dimensionless variable θ , such that $T = T_0 + \Delta T\theta$, where T_0 is the ambient temperature. The equation for θ is

$$\partial_t \theta + \vec{v} \cdot \nabla \theta = \nabla^2 \theta + \delta(y - h). \quad (4.67)$$

In this system of units, lowercase $\vec{v} = \vec{V}\tau/L$ and $h = H/L$ are the velocity and height function respectively. The evolution equation for the velocity in dimensionless variables becomes

$$\partial_t \vec{v} + \vec{v} \cdot \nabla \vec{v} = \mathcal{P} \nabla^2 \vec{v} - \nabla \tilde{P}_r + \mathcal{P} \mathcal{R}_T \theta \hat{y} - \mathcal{P} \mathcal{R}_C \Theta(y - h) \hat{y}. \quad (4.68)$$

Here we have introduced three dimensionless numbers: a Prandtl number $\mathcal{P} = \nu/D_T$, compositional Rayleigh number $\mathcal{R}_C = \alpha_C g D_T^2 / C_0^3 \nu$, and a thermal Rayleigh number $\mathcal{R}_T = \alpha_T g \Delta T D_T^2 / C_0^3 \nu$. The reduced pressure \tilde{P}_r is measured in units of $\rho_0 C_0^3 / D_T$. Since the velocity field is divergenceless, we introduce a stream function ψ which relates to the velocity in terms of $v_x = \partial_y \psi$ and $v_y = -\partial_x \psi$. We also define the vorticity ω as

$$\nabla^2 \psi = -\omega. \quad (4.69)$$

Taking the curl of Eq. 4.68, we can eliminate the reduced pressure leading to

$$\partial_t \omega = -\partial_y \psi \partial_x \omega + \partial_x \psi \partial_y \omega + \mathcal{P} (\nabla^2 \omega + \mathcal{R}_T \partial_x \theta + \mathcal{R}_C \partial_x h \delta(y - h)). \quad (4.70)$$

The front evolution in dimensionless form is

$$\partial_t h = 1 + \frac{\mathcal{V}}{D_T} \partial_x^2 h - \frac{\mathcal{K}}{D_T L^2} \partial_x^4 h + \frac{1}{2} (\partial_x h)^2 + \hat{n} \cdot \vec{v}. \quad (4.71)$$

The parameter \mathcal{V} for diffusive instabilities is a negative linear combination of different diffusion coefficients, therefore we define a positive Lewis number $\mathcal{L} = D_T/|\mathcal{V}|$. We choose \mathcal{K} to investigate the case of the KS equation where the coefficient of the second and fourth spatial derivatives are equal. The resulting front equation for this system is

$$\partial_t h = 1 - \frac{1}{\mathcal{L}} \partial_x^2 h - \frac{1}{\mathcal{L}} \partial_x^4 h + \frac{1}{2} (\partial_x h)^2 + \hat{n} \cdot \vec{v}. \quad (4.72)$$

We choose the Prandtl and the Lewis number from values used for the iodate-arsenous acid reaction. [142] We will study the stability and the evolution of the system in terms of different Rayleigh numbers, while keeping the fixed values $\mathcal{P} = 6.34$ and $\mathcal{L} = 72.5$.

4.9.2 Linear stability analysis

The equations of motion allow a flat front solution unbounded in the horizontal x direction. This convectionless front propagates upwards in the vertical y direction with a constant speed equal to one. In this section, we use a superindex 0 to designate a zeroth order solution for the unperturbed front

$$h^{(0)} = t. \quad (4.73)$$

The associated velocity field is equal to $\vec{v}^{(0)} = 0$, while the temperature corresponds to

$$\theta^{(0)} = \begin{cases} 1 & \text{if } y < 0, \\ \exp(-y) & \text{if } y \geq 0. \end{cases} \quad (4.74)$$

We will determine the stability of this solution by analyzing the evolution of small perturbations. We set a reference frame co-moving with the flat front defined by $y' = y - t$ and then drop the prime. Introducing small perturbations to all variables and neglecting terms of order two or higher, we arrive at a set of linear equations for the perturbed variables

$$\partial_t h^{(1)} = -\frac{1}{\mathcal{L}} \partial_x^2 h^{(1)} - \frac{1}{\mathcal{L}} \partial_x^4 h^{(1)} + v_y^{(1)}|_{y=0}, \quad (4.75a)$$

$$\partial_t \theta^{(1)} + \vec{v}^{(1)} \cdot \nabla \theta^{(0)} - \partial_y \theta^{(1)} = \nabla^2 \theta^{(1)} - h^{(1)} \delta'(y), \quad (4.75b)$$

$$\partial_t \omega^{(1)} - \partial_y \omega^{(1)} = \mathcal{P} \nabla^2 \omega^{(1)} + \mathcal{P} \mathcal{R}_T \partial_x \theta^{(1)} + \mathcal{P} \mathcal{R}_C \partial_x h^{(1)} \delta(y), \quad (4.75c)$$

$$\nabla^2 \psi^{(1)} = -\omega^{(1)}. \quad (4.75d)$$

Here the superindex (1) represents the first order perturbation to the corresponding variable. We combine equations 4.75c and 4.75d into a single equation for the y component of the velocity $w \equiv v_y = -\partial_x \psi$. This results in

$$\partial_t \nabla^2 w^{(1)} - \partial_y \nabla^2 w^{(1)} = \mathcal{P} \nabla^2 \nabla^2 w^{(1)} + \mathcal{P} \mathcal{R}_T \partial_x^2 \theta^{(1)} + \mathcal{P} \mathcal{R}_C \partial_x^2 h^{(1)} \delta(y). \quad (4.76)$$

The linearized system of equations admits plane wave solutions of the form $\exp(iqx + \sigma t)$, defining a wavenumber q and a growth rate σ . The perturbations are written as

$$h^{(1)} = \tilde{h} \exp(iqx + \sigma t), \quad (4.77a)$$

$$\theta^{(1)} = \tilde{\theta}(y) \exp(iqx + \sigma t), \quad (4.77b)$$

$$w^{(1)} = \tilde{w}(y) \exp(iqx + \sigma t). \quad (4.77c)$$

Substituting these perturbations in Eqs. 4.75a, 4.75b and 4.76. we obtain a set of equations for the variables \tilde{h} , $\tilde{\theta}$ and \tilde{w} . Dropping the y from the derivative $\partial_y = \partial$, we obtain

$$(\partial^2 - q^2)(\mathcal{P} \partial^2 + \partial - \mathcal{P} q^2 - \sigma) \tilde{w} - q^2 \mathcal{P} \mathcal{R}_T \tilde{\theta} - q^2 \mathcal{P} \mathcal{R}_C \tilde{h} \delta(y) = 0, \quad (4.78a)$$

$$(\partial^2 - \partial - q^2 - \sigma)\tilde{\theta} - \tilde{w}\partial\theta^{(0)} - \tilde{h}\delta'(y) = 0, \quad (4.78b)$$

$$\tilde{w}(0) = \left(\sigma - \frac{q^2}{\mathcal{L}} + \frac{q^4}{\mathcal{L}} \right) \tilde{h}. \quad (4.78c)$$

Integrating the equations just above and just below the front, we replace the delta functions with a set of jump conditions for the corresponding variables. Therefore, the equations become

$$(\partial^2 - q^2)(\mathcal{P}\partial^2 + \partial - \mathcal{P}q^2 - \sigma)\tilde{w} - q^2\mathcal{P}\mathcal{R}_T\tilde{\theta} = 0, \quad (4.79a)$$

$$(\partial^2 - \partial - q^2 - \sigma)\tilde{\theta} - \tilde{w}\partial\theta^{(0)} = 0, \quad (4.79b)$$

$$\tilde{w}(0) = \left(\sigma - \frac{q^2}{\mathcal{L}} + \frac{q^4}{\mathcal{L}} \right) \tilde{h}, \quad (4.79c)$$

with jump conditions

$$[\tilde{w}] = 0, \quad (4.80a)$$

$$[\partial\tilde{w}] = 0, \quad (4.80b)$$

$$[\partial^2\tilde{w}] = 0, \quad (4.80c)$$

$$[\partial^3\tilde{w}] = q^2\mathcal{R}_C\tilde{h}, \quad (4.80d)$$

$$[\tilde{\theta}] = \tilde{h}, \quad (4.80e)$$

$$[\partial\tilde{\theta}] = -\tilde{h}. \quad (4.80f)$$

The jumps at $y = 0$ for an arbitrary function f are represented as

$$[f] = \lim_{\epsilon \rightarrow 0^+} f(\epsilon) - \lim_{\epsilon \rightarrow 0^-} f(\epsilon). \quad (4.81)$$

We eliminate $\tilde{\theta}$ by combining equations 4.79a and 4.79b to obtain an equation only for the velocity \tilde{w}

$$(\partial^2 + \partial - q^2 - \sigma)(\partial^2 - q^2)(\mathcal{P}\partial^2 + \partial - \mathcal{P}q^2 - \sigma)\tilde{w} - q^2\mathcal{P}\mathcal{R}_T\partial\theta^{(0)}\tilde{w} = 0, \quad (4.82)$$

and the jump conditions for the temperature (Eqs. 4.80e and 4.80f) are replaced as conditions for the derivatives of \tilde{w} . These are

$$[\partial^4\tilde{w}] = \left(\mathcal{R}_T - \frac{\mathcal{R}_C}{\mathcal{P}} \right) q^2, \quad (4.83a)$$

$$[\partial^5\tilde{w}] = \left(\frac{1}{\mathcal{P}^2} + \frac{\sigma}{\mathcal{P}} + 2q^2 \right) q^2\mathcal{R}_C - \left(\frac{1}{\mathcal{P}} + 1 \right) q^2\mathcal{R}_T. \quad (4.83b)$$

Requiring a non-trivial solution for the equations, we arrive to a dispersion relation between a wavenumber q and growth rate σ . For $y < 0$, $\theta^{(0)}$ is constant, therefore

the solution for \tilde{w} consists of a linear combination of exponential functions. Since the solution must remain finite in this region, we obtain

$$\tilde{w} = A \exp(k_4 y) + B \exp(k_5 y) + C \exp(k_6 y), \quad (4.84)$$

where

$$k_4 = q, \quad (4.85a)$$

$$k_5 = -\frac{1}{2} + \left(\frac{1}{4} + q^2 + \sigma \right)^{1/2}, \quad (4.85b)$$

$$k_6 = -\frac{1}{2\mathcal{P}} + \left(\frac{1}{4\mathcal{P}} + q^2 + \frac{\sigma}{\mathcal{P}} \right)^{1/2}. \quad (4.85c)$$

For the region $y > 0$, the temperature $\theta^{(0)}$ decreases exponentially in the vertical direction. We proceed to construct a power series of exponential functions as described in [142], therefore \tilde{w} is written as

$$\tilde{w} = \sum_{i=1}^3 \sum_{m=0}^{\infty} D_m(k_i) \exp((k_i - m)z). \quad (4.86)$$

The series uses exponential terms with coefficients $k_1 = -q$, $k_2 = -1 - k_5$ and $k_3 = -1/\mathcal{P} - k_6$. The coefficients $D_m(k_i)$ are obtained from a recursion relation

$$D_m(k_i) = \frac{-q^2 \mathcal{P} D_{m-1}(k_i)}{((m + k_i)^2 - q^2) F(\mathcal{P}, m, k) F(1, m, k)}. \quad (4.87)$$

Where the F is shorthand for

$$F(\mathcal{P}, m, k) = (\mathcal{P}(m + k_i)^2 - (m + k_i) - \mathcal{P}q^2 - \sigma). \quad (4.88)$$

These solutions are valid as long as k_1, k_2 , and k_3 are distinct and do not differ by an integer. Any solution with these properties will be excluded from the results. The velocity \tilde{w} and its derivatives must satisfy the jump conditions at $y = 0$, given by Eqs. 4.80 and 4.83. Using the expressions of \tilde{w} from Eq. 4.84 and 4.86, we find a linear system of equations for the coefficients $A, B, C, \tilde{H}, D_0(k_1), D_0(k_2)$, and $D_0(k_3)$. These equations take the form $\mathbf{L}U = 0$ with

$$\mathbf{L} = \begin{bmatrix} a_0 & b_0 & c_0 & 0 & 0 & 0 & L_{1,7} \\ -a_0 & -b_0 & -c_0 & 1 & 1 & 1 & 0 \\ -a_1 & -b_1 & -c_1 & k_4 & k_5 & k_6 & 0 \\ -a_2 & -b_2 & -c_2 & k_4^2 & k_5^2 & k_6^2 & 0 \\ -a_3 & -b_3 & -c_3 & k_4^3 & k_5^3 & k_6^3 & L_{5,7} \\ -a_4 & -b_4 & -c_4 & k_4^4 & k_5^4 & k_6^4 & L_{6,7} \\ -a_5 & -b_5 & -c_5 & k_4^5 & k_5^5 & k_6^5 & L_{7,7} \end{bmatrix}, \quad (4.89)$$

and

$$U = \begin{bmatrix} D_0(k_1) \\ D_0(k_2) \\ D_0(k_3) \\ A \\ B \\ C \\ \tilde{H} \end{bmatrix}. \quad (4.90)$$

The matrix requires evaluating the series

$$a_n = \sum_{m=0}^{\infty} (-1)^n (k_1 + m)^n D_n(k_1), \quad (4.91a)$$

$$b_n = \sum_{m=0}^{\infty} (-1)^n (k_2 + m)^n D_n(k_2), \quad (4.91b)$$

$$c_n = \sum_{m=0}^{\infty} (-1)^n (k_3 + m)^n D_n(k_3), \quad (4.91c)$$

and the remaining terms in the last column of the matrix \mathbf{L} correspond to

$$L_{1,7} = - \left(\sigma - \frac{1}{\mathcal{L}} (q^2 - q^4) \right), \quad (4.92a)$$

$$L_{5,7} = \mathcal{R}_C q^2, \quad (4.92b)$$

$$L_{6,7} = \left(\mathcal{R}_T - \frac{\mathcal{R}_C}{\mathcal{P}} \right) q^2, \quad (4.92c)$$

$$L_{7,7} = \left(\frac{1}{\mathcal{P}^2} + \frac{\sigma}{\mathcal{P}} + 2q^2 \right) q^2 \mathcal{R}_C - \left(\frac{1}{\mathcal{P}} + 1 \right) q^2 \mathcal{R}_T. \quad (4.92d)$$

The determinant of \mathbf{L} should vanish to allow a nontrivial solution to the linear set of equations. This condition leads to a dispersion relation between the wavenumber q and the growth rate σ , which can be a complex number. The dispersion relation determines the stability of the front, if the real part of σ is positive for certain Rayleigh numbers, the front is unstable. We explore the dispersion relation for different values of the Rayleigh numbers, calculating the determinant numerically using routines from LAPACK [143].

4.9.3 Weakly nonlinear regime

We study the nonlinear front propagation in a narrow rectangular domain resembling a two-dimensional tube. It is helpful to define a moving coordinate system $y' = y - \bar{h}(t)$, where $\bar{h}(t)$ is the spatial front average. The mean front velocity

is $v_h = d\bar{h}/dt$, while the front height corresponds to $h' = h - \bar{h}$. We focus on the propagation of the front near the onset of convection, therefore we expand the corresponding equations to include only terms up to order $o(h'^2)$. The weakly nonlinear equations correspond to

$$\partial_t h = 1 - v_h - \frac{1}{\mathcal{L}} \partial_x^2 h - \frac{1}{\mathcal{L}} \partial_x^4 h + \frac{1}{2} (\partial_x h)^2 - \partial_x \psi|_{y=0} - \partial_x h \partial_y \psi|_{y=0}, \quad (4.93a)$$

$$\partial_t \theta = \nabla^2 \theta - \partial_y \psi \partial_x \theta + \partial_x \psi \partial_y \theta + v_h \partial_y \theta + \delta(y) - \delta'(y) h + \frac{1}{2} \delta''(y) h^2, \quad (4.93b)$$

$$\partial_t \omega = \mathcal{P} \nabla^2 \omega - \partial_y \psi \partial_x \omega + \partial_x \psi \partial_y \omega + v_h \partial_y \omega + \mathcal{P} \mathcal{R}_T \partial_x \theta + \mathcal{P} \mathcal{R}_C \partial_x h (\delta(y) - h \delta'(y)), \quad (4.93c)$$

where we dropped the primes. The stream function ψ follows from the vorticity (Eq. 4.69). The vertical walls are insulating boundaries with no chemical flow. We consider stress-free boundaries for the fluid velocity, this allows to compare the transition to convection from the previous linear stability analysis. These boundaries allow the use of Fourier series to expand the corresponding variables

$$h = \sum_{n=1}^{\infty} h_n(t) \cos(nqx), \quad (4.94a)$$

$$\theta = \sum_{n=1}^{\infty} \theta_n(y, t) \cos(nqx), \quad (4.94b)$$

$$\psi = \sum_{n=1}^{\infty} \psi_n(y, t) \sin(nqx), \quad (4.94c)$$

$$\omega = \sum_{n=1}^{\infty} \omega_n(y, t) \sin(nqx). \quad (4.94d)$$

These series are introduced into the system and projected into the corresponding basis functions. This procedure leads to a system of equations for the Fourier coefficient that depend on y . We use a finite difference method on a uniform grid to evaluate the spatial derivatives, as well as the expressions for the delta function and its derivatives. [84] The evolution of the coefficients is evaluated using implicit and explicit forms of the Euler method. [90]

5 Exothermic reaction fronts in liquids confined between conductive walls

Exothermic autocatalytic reaction fronts propagating between two conductive walls shows an increase of speed and change in shape due to buoyancy driven convection. We modeled the system using reaction-diffusion-advection equations for chemical concentration and temperature. In these equations, a cubic autocatalytic exothermic reaction leads to a propagating front. The fluid flow is determined by the Stokes equation allowing for density changes due to thermal expansion. The front propagates in a liquid confined in a narrow rectangular domain resembling a two dimensional tube. Fluid motion enhances the front speed and modifies its curvature. In vertical domains, a transition to a nonaxisymmetric front takes place as the width increases. Heat conductivity across the walls delays the transition to larger critical widths. We find regions of bistability between nonaxisymmetric fronts and lower speed fronts at different values of conductivity. Heat losses diminish convection in horizontal tubes, resulting in a decrease of front speed.

Chemical reaction fronts propagate in liquids generate density gradients across the front. These gradients arise due to changes in temperature and chemical composition that may lead to convection. Several experiments have established the presence of fluid convection near reaction fronts. Heat release in polymerization fronts leads to density gradients that generate buoyancy driven convection [144, 15]. In the IAA reaction, the propagating front is a thin interface that separates reacted from unreacted fluid. Experiments in thin vertical cylinders show that this interface can have a symmetric or nonaxisymmetric shape with respect to the longitudinal axis of the cylinder [60]. In the case of the symmetric shape, the highest position of the interface (its maximum height), lies on the longitudinal axis. Whereas in the non-axisymmetric shape, the maximum height is near the wall. These experiments show a transition between these two types of fronts as the diameter of the tube increases. These results can be accounted for in the limit of infinite thermal diffusivity, where the unreacted fluid is set at the higher temperature of the reacted fluid [126, 145]. The effects of heat release in the IAA reaction led to the formation of three dimensional structures traveling in horizontal channels [146]. Experiments for the chlorite-tetrathionate (CT) reaction in Hele-Shaw cells observed fingering due to thermal and multicomponent convection [147, 148]. Three dimensional structures propagating in the CT reaction developed their shape due to thermal and compositional convection [46].

Theoretical work analyzed the effect of combined heat and compositional changes. A linear stability analysis of flat fronts propagating vertically showed thermal and compositional driven convection with unexpected configurations of density gradients [49, 141]. In horizontal layers, exothermic fronts can exhibit oscillations due to convection [136]. Theories on thin reaction fronts with heat release showed instabilities leading to an increase in front speed [149]. Mukherjee and Paul explored autocatalytic front propagation with compositional and thermal gradients traveling in steady and chaotic flows [150, 151].

Heat losses play an important role in the propagation of exothermic reaction fronts in liquids. Experiments by Martin et al. measuring the temperature profile of reaction fronts in the CT reaction showed good agreement with a model that included heat losses [48]. Studies of polymerization fronts including convective heat losses showed an extended range of more complex instabilities for front propagation [152]. Theoretical studies in Hele-Shaw cells used Darcy's law hydrodynamics and Newton's cooling law to account for heat losses. In these theories, a linear stability analysis showed that heat losses modify the stability of a system with perfectly insulating walls depending on the density gradients and the direction of front propagation [153]. In the nonlinear regime, heat losses led to tip splitting for fingering in reaction fronts [154, 155]. Further experimental and theoretical work in the IAA reaction analyzed the velocity field during tip splitting [156]. These studies showed new instabilities and complex behaviors generated by heat loss.

In this chapter, we consider an exothermic autocatalytic reaction front propagating in a fluid confined between conductive walls. In our case, heat flows through the boundaries, leading to a temperature gradient between the walls. The hydrodynamics is modeled using the Stokes equations in a two dimensional domain that resembles a long tube. In vertical tubes, convection always take place due to a horizontal density gradient induced by heat losses. We will show that a state of low convective flow will lose stability to a nonaxisymmetric state as the distance between the walls increases. Fronts propagating in horizontal layers will change their speed and shape due to convection.

5.1 Results

5.1.1 Vertical propagation

A convectionless flat front progataing between insulating walls (with Biot number $Bi = 0$) can become unstable due to density gradients across the front. This

buoyancy driven convection appears when the width is increased beyond a critical value. Beyond this threshold, convection sets in, leading to an asymptotic state, consisting of a nonaxisymmetric curved front of constant shape, traveling with a constant speed higher than the speed of the flat front (Fig. 3). In the asymptotic state, since the front propagates with constant speed along the y direction, we can obtain this speed calculating $v_f = -\partial_t c / \partial_y c$ near $c = 0.5$. The front is not symmetric with respect to a vertical line through the middle of the domain width, defined here as the axis. The convective fluid flow consists of two counter rotating rolls one above the other, with the reaction front inserted between the two rolls, as shown in Fig. 4.

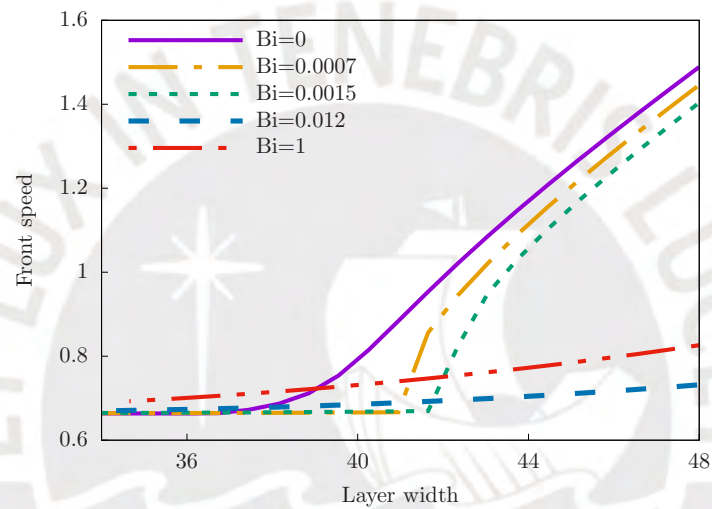


Figure 3: Front speed as a function of width for vertical propagation, using walls of different conductivities (different Bi values).

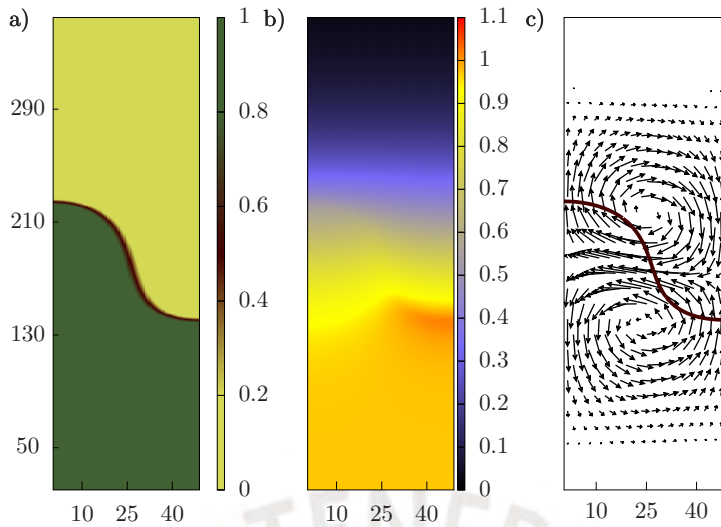


Figure 4: Concentration (a), temperature (b) and velocity fields (c) for width of $L_x = 49$. The boundary condition corresponds to insulating walls ($Bi=0$).

For non-zero Biot numbers, there is always a horizontal thermal gradient due to heat flow across the confining walls. This leads to a horizontal density gradient, resulting in convection, inhibiting the formation of a flat front. For small Biot numbers and very narrow widths, convection will be very small due to fluid viscosity, thus its shape is nearly flat. In this case, the speed of the front is very close to the speed of the flat front, as shown in Fig. 3. Increasing the width will also result in a transition to nonaxisymmetric convection, however this takes place at higher width values. In the case of insulating walls the transition takes place at around $L_x = 38$, while for $Bi = 0.0015$ it is close to $L_x = 42$, indicating that a small Biot number will have a high impact in this critical value. The speed of the nonaxisymmetric fronts increase rapidly as a function of width. For larger widths, the front becomes very elongated, requiring the use of a much larger computational domain, therefore we study fronts for widths up to $L_x = 49$. Using these widths, we found no transitions to nonaxisymmetric fronts for Biot numbers larger than $Bi = 0.012$. Before the transition, the speed of the front is close to the flat front speed, increasing as the Biot number is increased. This increment is significant for $Bi = 1.0$, with the speed also increasing as a function of width, as seen in Fig. 3. The speed of the fronts does not change significantly for Biot numbers larger than one. In this cases, the wall temperature becomes very close to the ambient temperature. The region where the deformation of the front is more pronounced and the flow more intense can be described with the mixing length [157, 158]. In Fig. 5 we show the mixing length as a function of domain width for different Biot numbers. We notice large increase of mixing length in the case of insulating

walls. The increase is smaller for large Biot numbers, which shows less intense convective flow. The values of the mixing length range from about 13 for the convectionless flat front to about 90 for the nonaxisymmetric front. These values are small compared to the length of the computational domain ($L_y = 1050$). The behavior of mixing length as a function of width is similar to the description of the front velocity with respect to the width as shown in Fig. 3.

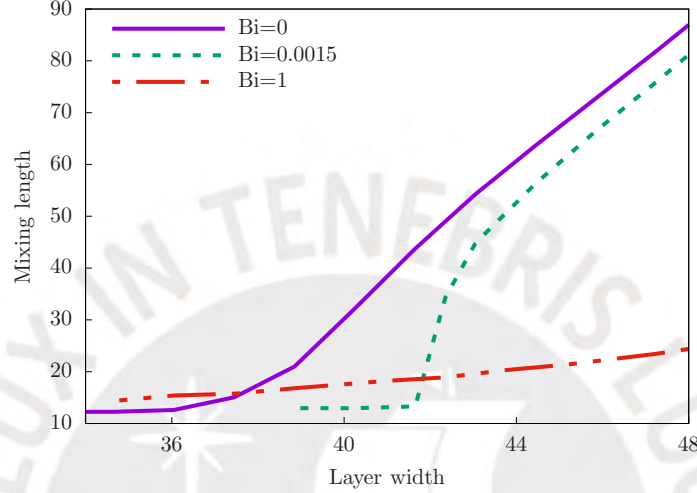


Figure 5: Mixing length as a function of width for vertical propagation, using walls of different conductivities (different Bi values).

The speed and shape of the fronts for a fixed width depends on the Biot number. In fig. 6, we display the speed of the front as a function of Biot number for a fixed width of $L_x = 40.6$. This figure shows an initial nonaxisymmetric front for insulating walls ($Bi = 0$) displaying a decrease of speed as the Biot number increases. This behavior continues until it reaches a value where the front curvature becomes small, with a maximum height near the axis, and a speed close to the flat front speed. Increasing the Biot number further increases the speed of the front, without changing the characteristics of the shape. Fixing the length to $L_x = 43.4$, also results in an initial nonaxisymmetric front for insulating walls which reduces its speed as the Biot number increases as shown in Fig. 7. The front changes speed abruptly at $Bi = 0.0022$, where it becomes a low curvature front. Further increases in Biot number increases the speed only slightly. The abrupt change corresponds to a region of bistability between the two types of fronts. Starting above the transition, and then reducing the Biot number leads to a stable front of low curvature, with a lower speed. This takes place until $Bi = 0.0019$, where there is a transition to the nonaxisymmetric front. The same behavior is observed

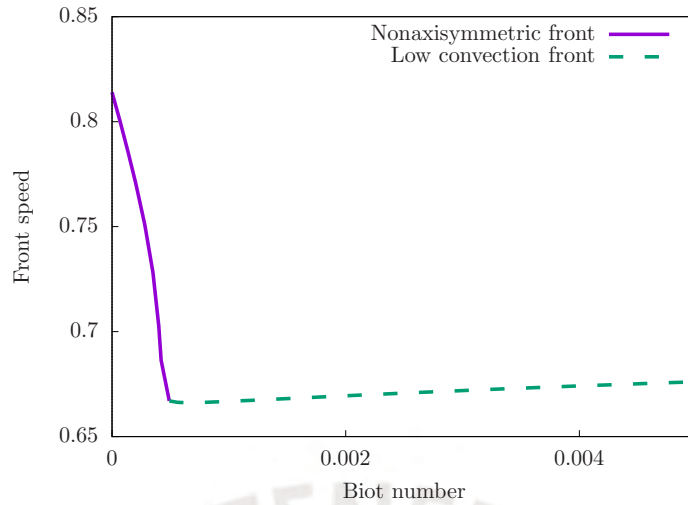


Figure 6: Front speed in vertical propagation for varying Bi numbers and fixed width $L_x=40.6$.

at $L_x = 49$, showing a region of bistability between the two types of fronts (Fig. 8). However, in this case the region of bistability is wider, taking place at higher Biot numbers.

We display the different front shapes in the bistable region together with their associated fluid velocities in Figs. 9 and 10. Both types of front appear for the same width and Biot number but using different initial conditions. The nonaxisymmetric front in Fig. 9 resembles the front for insulating walls of Fig. 10. In both cases, the fronts have a maximum height on one side of the domain and a minimum on the opposite side. However, the distance between the maximum and minimum heights is smaller for the front with non-zero Biot number due to heat losses. In both cases, the fluid velocity field consists of two counter rotating rolls supporting a similar nonaxisymmetric shape. For insulating walls, the temperature far behind the front takes a constant value higher than the ambient temperature. While for conductive walls, the temperature behind the front eventually decays to the ambient temperature. The overall maximum local temperature within the domain is higher for insulating walls $T = 1.018$, compared to $T = 0.310$ for conductive walls. We also notice a hotspot on the lower side of the front with insulating walls (Fig. 4), but for a finite Biot number the hotspot appears near the middle of the domain, away from the wall. We display in Fig. 10 the other stable front for the same parameters in the bistable region. In this case, the front is higher near the domain axis, having a local minimum on each wall. The distance between these maximum and minimum heights is small compared to the nonaxisymmetric case.

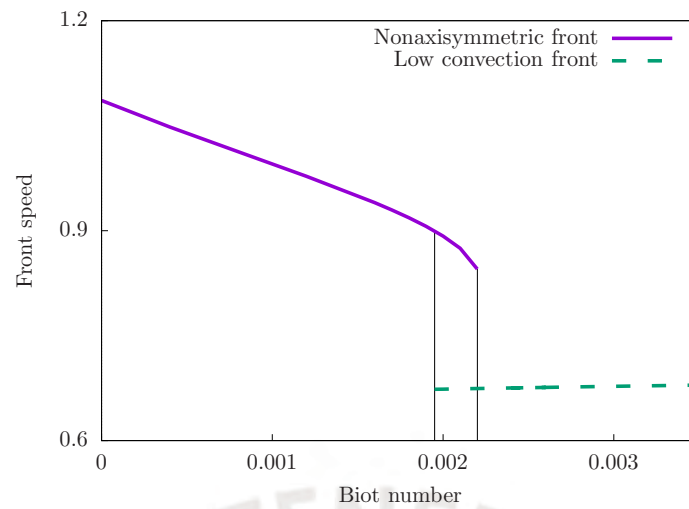


Figure 7: Front speed in vertical propagation for varying Bi numbers and fixed width $L_x=43.4$. Vertical lines describe the region of bistability

The fluid velocity field near the front consists of counter rotating rolls one next to the other. The fluid rises along the axis and falls on the sides, shaping the front. Below the front, we notice smaller convective rolls underneath the rolls previously discussed. As in the previous case, the temperature far behind the front becomes the ambient temperature due to heat losses. The maximum temperature in the domain takes place near the middle ($T = 0.238$), which is lower than the one obtained for the nonaxisymmetric front.

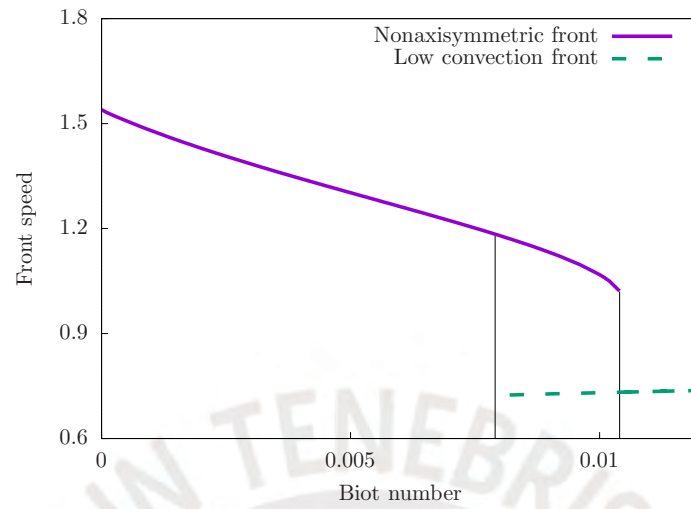


Figure 8: Front speed in vertical propagation for varying Bi numbers and fixed width $L_x=49$. Vertical lines describe the region of bistability

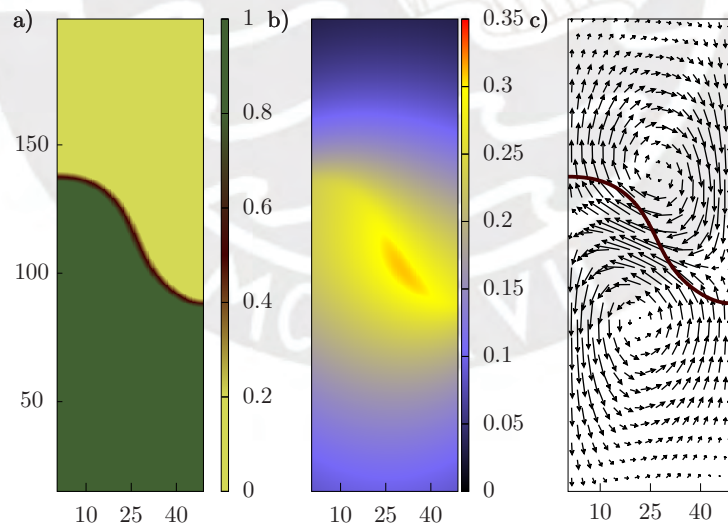


Figure 9: Concentration (a), temperature (b) and velocity fields (c) for width of $L_x = 49$. The boundary condition includes heat loss ($Bi=0.01$). These parameters allow bistability.

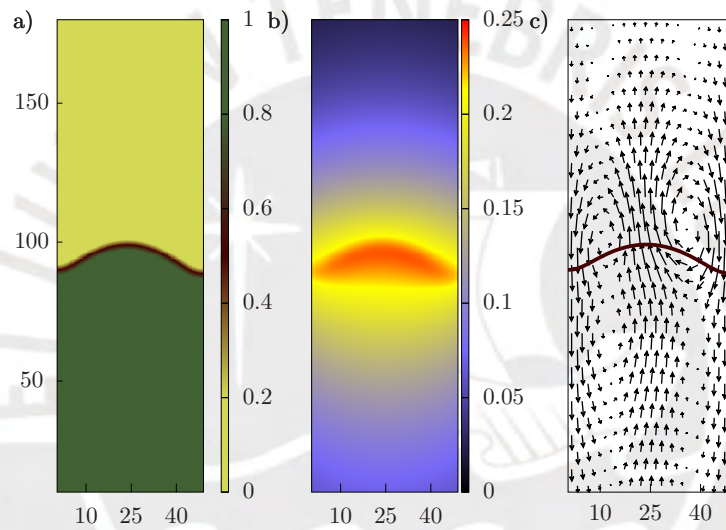


Figure 10: Concentration (a), temperature (b) and velocity fields (c) for width of $L_x = 49$. The boundary condition includes heat loss ($Bi=0.01$). These parameters allow bistability.

5.1.2 Horizontal propagation

As the front propagates horizontally, convection will always be present enhancing the speed of the front. In very narrow tubes, this effect is negligible because the fluid viscosity sets a weak convective flow. When the width L_y increases, convection becomes significant, increasing the speed of the front as shown in fig. 11. The speed increases faster for insulating walls ($Bi = 0$). For conductive

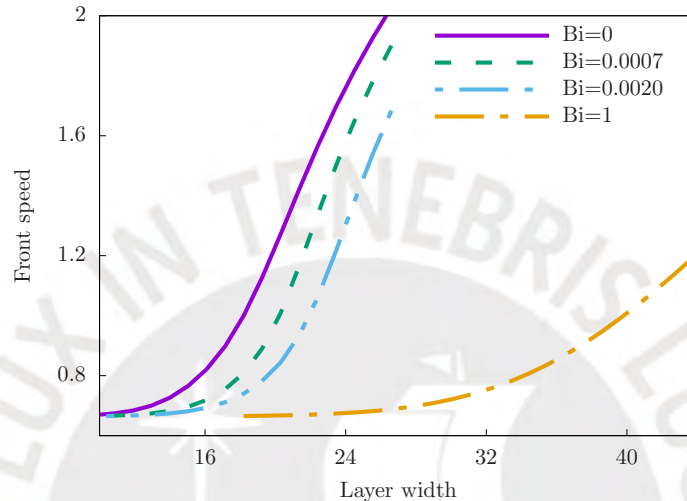


Figure 11: Front speed as a function of width for horizontal propagation using walls of different conductivities (different Bi values).

walls having non-zero Biot numbers, the increase of speed is slower for larger Biot numbers. For $Bi = 1$, the temperature of the walls are nearly at the ambient temperature as shown in Fig. 12. Therefore this result is similar to setting the boundaries at the ambient temperature. The temperature far behind the front corresponds to the ambient temperature, due to heat losses through the walls. The temperature is higher close to the axis of the domain, with a local maximum of $T = 0.078$. This value is smaller than $\Delta T = 1$, the change in temperature across a convectionless fronts. The front has a leading edge at the top boundary, placing reacted fluid above unreacted fluid. The velocity field consists of two counter rotating rolls travelling with the front (fig. 12). Although the jump in temperature is small, the convective flow is strong enough to support a significant curvature.

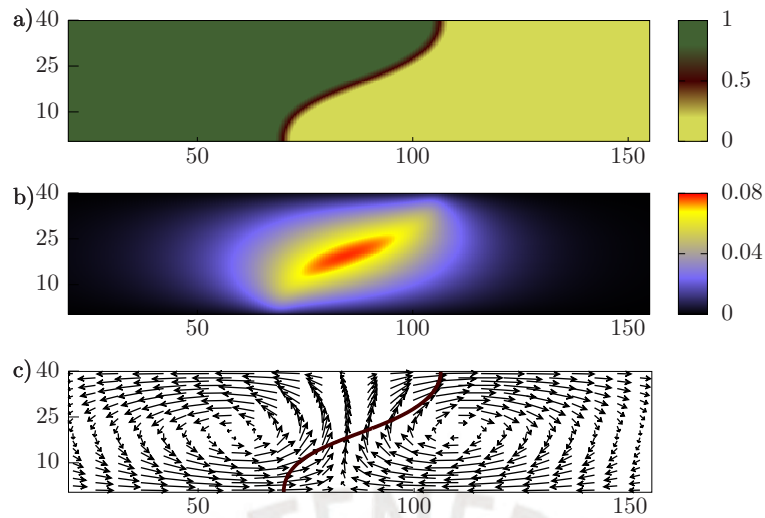


Figure 12: Concentration (a), temperature (b) and velocity fields (c) for width of $L_y=40$. The boundary condition includes heat loss ($Bi=0.01$). These parameters allow bistability.

5.2 Summary and discussion

In this chapter, we analyzed transitions between convective fronts propagating in narrow two-dimensional rectangular domains, accounting for heat losses. We considered convection arising from temperature gradients due to exothermic chemical reaction fronts. In the case of a vertical domain with insulating walls, a flat front can propagate without convection, however this is not possible for conductive walls. Heat losses imply that the fluid near the axis is at a higher temperature than near the walls. This provides a horizontal density gradient, which always leads to convection. If the width is small, the front is slightly curved, and its speed is close to the flat front speed. For a vertical rectangular domain with insulating walls, increasing the width beyond a critical value results in a transition to convection. For widths above the transition, the front acquires a nonaxisymmetric shape due to convection. The transition to this state is modified due to heat losses, with the critical width changing significantly even for small Biot numbers. We found no transition considering Biot numbers larger than $Bi = 1$ for widths below $L_x = 48$. For conductive walls, the fluid temperature far behind the front becomes the ambient temperature as heat dissipates through the walls. We observe regions of bistability between nonaxisymmetric fronts and low curvature fronts for vertical propagation. This bistability appears only for large enough widths, over a range of Biot numbers.

For horizontal propagation, we find that the speed of the front will always increase as we increase the width. However, the increase of speed as a function of width is smaller for large Biot numbers. In these cases, fluid velocities will be smaller due to heat losses, resulting in lower temperatures driving convection. The fronts always have a nonaxisymmetric shape, with a leading edge on the top boundary.

Our calculations showed the importance of conductive boundaries in analyzing experiments for exothermic reaction fronts. Particularly because the inner region of the domain is warmer than the walls, setting a density gradient between the walls. The transition between states can be explored in experiments using narrow tubes using materials of different conductive properties. Future work can include a detailed comparison between theory and experiment, which requires new calculations to account for three dimensional effects.



6 Front instabilities in the presence of convection due to thermal and compositional gradients

Reaction fronts separate fluids of different densities due to thermal and compositional gradients that may lead to convection. The stability of convectionless flat fronts propagating in the vertical direction depends not only on the fluid properties, but also in the dynamics of a front evolution equation. In this chapter, we analyze fronts described by the Kuramoto-Sivashinsky (KS) equation coupled to hydrodynamics. Without density gradients, the KS equation has a flat front solution that is unstable to perturbations of long wavelengths. Buoyancy enhances this instability if a fluid of lower density is underneath a denser fluid. In the reverse situation, with the denser fluid underneath, the front can be stabilized with the appropriate thermal and compositional gradients. However, in this situation, a different instability develops for large enough thermal gradients. We also solve numerically the nonlinear KS equation coupled to the Navier-Stokes equations to analyze the front propagation in two-dimensional rectangular domains. As convection takes place, the reaction front curves, increasing its velocity.

Propagating reaction fronts in fluids separate reacted from unreacted substances. The fronts can be considered as thin interfaces subject to a particular front evolution equation. We study the effects of convection on front instabilities described by the Kuramoto-Sivashinsky (KS) equation. Across a front, density gradients develop due to changes in temperature and chemical composition. These gradients may lead to convective fluid motion, which modifies the front shape and speed. Without fluid flow, the flat front solutions described by the KS equation are unstable, but in fluids they can be stabilized with a fluid of lower density above the front. However, even in this case, instabilities can appear if the thermal density gradient is strong enough. We also solve numerically the nonlinear equations to determine the changes in front shape and speed.

Reaction fronts propagating in liquids generate density gradients leading to convection. Several experiments in capillary tubes and Hele-Shaw cells have determined the influence of fluid flow in the shape and speed of the fronts. [60, 159, 160] The density gradients arise from the different chemical compositions between reacted and unreacted fluids, or from temperature changes across the front. In narrow tubes, convective fronts of constant shape travel with a speed faster than flat fronts without convection. [60] Experiments for horizontally travelling fronts in

the CT reaction confined in Hele-Shaw cells reveal spatiotemporal dynamics due to thermal and compositional effects on density gradients. [161] Experiments and theory in a three-dimensional medium revealed the influence of thermal effects on convective front propagation. [46]

Theoretical work using thin front approximations and reaction-diffusion-advection equations accounted for the front instabilities and increase of speed in the IAA reaction. [126, 59, 162, 163] These studies approximated the heat effects using the limit of infinite thermal diffusivity. Further theoretical studies for reaction-diffusion-advection fronts involving heat resulted in novel types of hydrodynamic instabilities. [164] Heat loss explained finger splitting in exothermic reaction-diffusion-advection fronts inside Hele-Shaw cells. [165] Front propagation in horizontal layers depends on whether convection is driven by compositional or thermal gradients. [150] Diffusive instabilities in reaction fronts are inhibited in a liquid if the less dense fluid is above the front. [166] Instabilities in thin reaction fronts without convection can lead to steady shapes, oscillatory instabilities, and chaos due to compositional gradients across the front. [67, 167, 168]

In this chapter, we consider reaction fronts described by the Kuramoto-Sivashinsky (KS) equation inside a fluid. In the absence of convection, the KS equation allows for a flat front solution that is unstable for perturbations of large wavelength. This equation can be applied to several physical systems such as combustion flames [12], chemical waves [169], or reaction-diffusion-advection fronts with diffusive instabilities. [63, 170] Recent applications of the KS equation involving hydrodynamics include falling film flows [171], Rayleigh-Bénard instabilities in the Earth's upper mantle [172], and a network analysis for the Rayleigh-Taylor instability. [173] Fronts propagating in liquids can lead to density gradients caused by thermal or chemical composition, resulting in convection. As these fronts propagate in liquids, they can lead to density gradients caused by thermal or chemical composition, resulting in convection. The instability of flat fronts in the KS equation is enhanced by buoyant compositional density gradients, as the front separates fluids of different density. In addition, curved fronts and extended structures can be stabilized with decreasing density in the upward vertical direction. [67] For Navier—Stokes hydrodynamics, oscillatory transitions to convection can appear due to a change in composition across the front. [168] Here we will explore the influence of thermal and compositional driven convection on fronts described by the KS equation. Our results will show that if the lighter fluid is underneath a heavier fluid, the front will always be unstable. However, in the opposite case, an instability can also appear driven by thermal effects. This work also includes the

nonlinear propagation for fronts near the onset of the instabilities inside narrow rectangular domains.

6.1 Results

6.1.1 Linear stability analysis

The growth rate σ determines the stability of a perturbation with a fixed wavenumber q . If the real part of σ is positive, the amplitude of the perturbation will grow, otherwise it will decay. We obtain a dispersion relation σ vs q requiring that the determinant of the matrix \mathbf{L} vanishes (Eq. 4.89). This condition leads to several solutions for σ , some of them may even be complex. Therefore, the front stability is determined by the largest real part of the growth rate

The KS equation without advection exhibits instabilities for wavenumbers $q < 1$ as shown in Fig. 13. The presence of density driven flow will alter the corresponding dispersion relation. We show two cases, one with convection driven only by thermal expansion, and the other only by a compositional density gradient. In both cases we use small positive Rayleigh numbers indicating a lower density fluid below a higher density fluid. In the case of compositional density gradient, the range of wavenumbers with positive growth rate increases significantly. Whereas, for thermal density gradients, the range of wavenumbers with positive growth rate is similar to the convectionless KS front. In both cases, the maximum growth rate becomes larger at a lower wavenumber q . In this chapter, we analyze the interactions between thermal and compositional density changes as represented by the Rayleigh numbers \mathcal{R}_T and \mathcal{R}_C . If both Rayleigh numbers have the same sign, the system is referred to as cooperative, while opposite signs are referred to as antagonistic. [174] In figure 13 we identify the stability of the flat fronts for different values of the Rayleigh numbers \mathcal{R}_T and \mathcal{R}_C . Near the origin, the flat front is unstable, which is also the case of the instability in the convectionless KS equation. In the case of $\mathcal{R}_T = 0$, the front is unstable for positive \mathcal{R}_C , but decreasing \mathcal{R}_C below a negative threshold will stabilize the front. In the latter case, having the lower density fluid on top presents a stabilizing mechanism. Similarly, for $\mathcal{R}_C = 0$, the front is unstable for positive \mathcal{R}_T , but decreasing \mathcal{R}_T below a negative threshold stabilizes the front. If \mathcal{R}_T is decreased further, below a second negative threshold, the front becomes unstable again. This unexpected result also appears in buoyancy driven instabilities for propagating reaction-diffusion-advection fronts with hydrodynamics described by Darcy's law. [164]

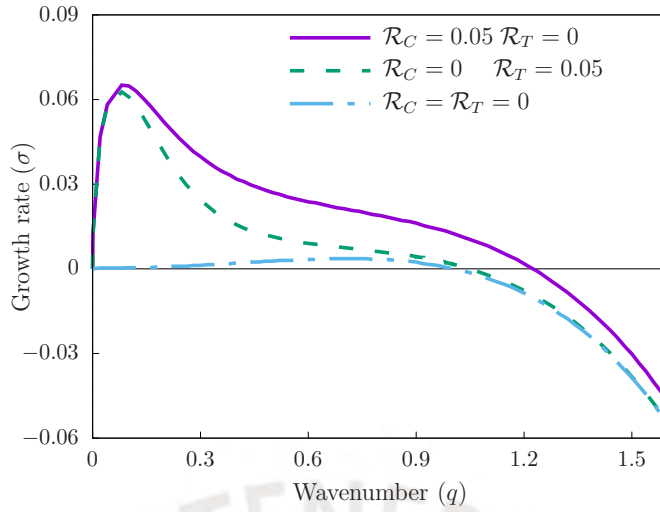


Figure 13: Dispersion relations for different positive Rayleigh numbers. Without density gradients ($\mathcal{R}_T = \mathcal{R}_C = 0$), the front is unstable for perturbations of small wavenumbers q . Positive Rayleigh numbers enhance the instability of the front

The combined effects of the thermal and compositional Rayleigh numbers on the front stability can be classified according to their signs. When both Rayleigh numbers are positive (corresponding to values in the first quadrant of Fig. 14.), their combined effect is cooperative. In each case, they represent positive density gradients in the vertical direction, where a lower density fluid is underneath a denser fluid. In this quadrant, the maximum growth rate for a fixed value of the Rayleigh numbers is real and positive. Therefore, all fronts in this quadrant are unstable, with buoyancy forces contributing to the instability. In the fourth quadrant of Fig. 14, where \mathcal{R}_T is positive and \mathcal{R}_C is negative, the stability of the front depends on the particular values of the Rayleigh numbers. In this quadrant, a negative \mathcal{R}_C will tend to stabilize the convectionless KS front. A stabilized front with a negative \mathcal{R}_C can be destabilized by increasing \mathcal{R}_T beyond a critical value. This positive \mathcal{R}_T represents the destabilizing buoyancy forces induced by thermal gradients. Increasing the magnitude of negative \mathcal{R}_C requires a larger \mathcal{R}_T to destabilize the front. When both Rayleigh numbers are negative (third quadrant of Fig. 14, their cooperative effect indicates a fluid of lower density above the front. However, in this quadrant, instability reappears for negative values of \mathcal{R}_T with magnitude larger than 0.985. This counterintuitive result was previously shown in reaction-diffusion-advection fronts of finite thickness, in our case the front is infinitesimally thin evolving under the KS equation. [164] In the second quadrant (where \mathcal{R}_C is positive and \mathcal{R}_T is negative), the fronts are unstable for large enough \mathcal{R}_C , regardless of the value of \mathcal{R}_T . Similarly, for large enough

magnitudes of negative \mathcal{R}_T the fronts will be unstable. However, if \mathcal{R}_C is small enough, there is a range of values of \mathcal{R}_T that can stabilize the front.

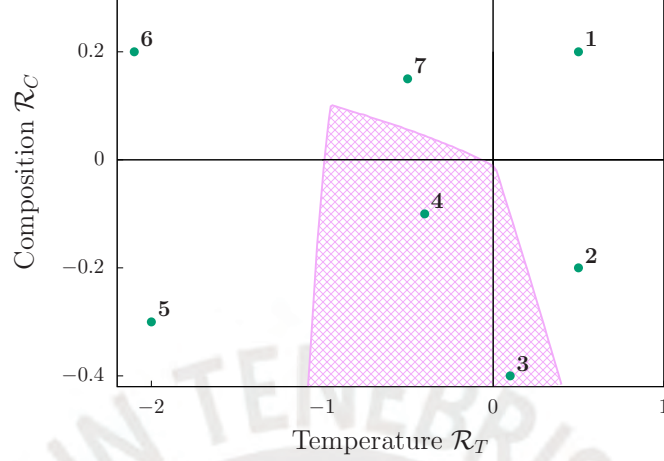


Figure 14: Stability map for flat fronts. The shaded region corresponds to stable flat fronts. The numbers correspond to selected values of Rayleigh numbers for dispersion relations shown in in Figs. 15 and 16.

We show dispersion relations for some values of Rayleigh numbers in Fig. 15, keeping \mathcal{R}_T positive. These values are labeled with numbered points in the stability map (Fig. 14), corresponding to numbered dispersion relations shown in Fig. 15. In the first quadrant, we chose $\mathcal{R}_T = 0.5$ and $\mathcal{R}_C = 0.2$, corresponding to point 1 in the stability map. Curve 1 (Fig. 14) indicates real maximum growth rates as a function of the wavenumber q . The growth rate is positive for q close to zero, increasing to a maximum value as q increases. Increasing q further, the growth rate decreases, reaching negative values for large q . There is a critical wavenumber q_c where the growth rate is zero. Perturbations with a wavenumber above q_c will decay. In the fourth quadrant, we chose $\mathcal{R}_T = 0.5$ and $\mathcal{R}_C = -0.2$, corresponding to point 2 in the stability map. Curve 2 (Fig. 15) shows a similar behavior as curve 1, but with smaller growth rates and a smaller critical wavenumber q_c . The antagonistic effect of negative \mathcal{R}_C tends to stabilize the front. For curve 3 ($\mathcal{R}_T = 0.1$ and $\mathcal{R}_C = -0.4$), the maximum real part of the growth rate is always negative, represented by the solid curve. These growth rates have a non-zero imaginary part for small q , becoming real numbers for larger q . The dotted line represents only the positive imaginary part, with its complex conjugate also present in the dispersion relation.

In Fig.16 we show dispersion relations for some selected values of Rayleigh numbers

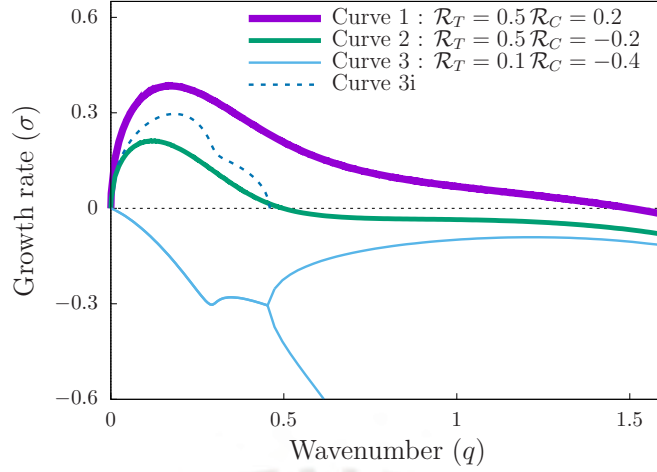


Figure 15: Dispersion relations for different values of \mathcal{R}_C and positive \mathcal{R}_T . The numbers correspond to different points in Fig. 2. The solid lines are the largest real part of the growth rate. Line 3 also displays the second largest real part of the growth rate. The dotted line 3i displays the non-zero imaginary part of the growth rate for point 3.

with \mathcal{R}_T negative. When the magnitude of negative \mathcal{R}_T is small, a negative \mathcal{R}_C value leads to a stable front, as shown in the dispersion relation for $\mathcal{R}_C = -0.4$ and $\mathcal{R}_T = -0.1$ (curve 4). Keeping the magnitude of \mathcal{R}_T small, the front can become unstable with a large enough \mathcal{R}_C as displayed in curve 7 ($\mathcal{R}_T = -0.5$ and $\mathcal{R}_C = 0.15$). In this curve, we find negative growth rates for small q and positive growth rates in a finite range of wavenumbers. The stable front can also become unstable if \mathcal{R}_T is large enough regardless of the value of \mathcal{R}_C , as shown in curves 5 and 6. The values of the Rayleigh numbers for curve 5 are $\mathcal{R}_T = -2$ and $\mathcal{R}_C = -0.3$, and for curve 6 they are $\mathcal{R}_T = -2.1$ and $\mathcal{R}_C = 0.2$. In both curves, we find positive growth rates near $q = 0$, with each curve having two relative maximums. The maximum closer to $q = 0$ is positive in both curves. The other maximum is positive only in curve 6, setting an additional range of positive growth rates.

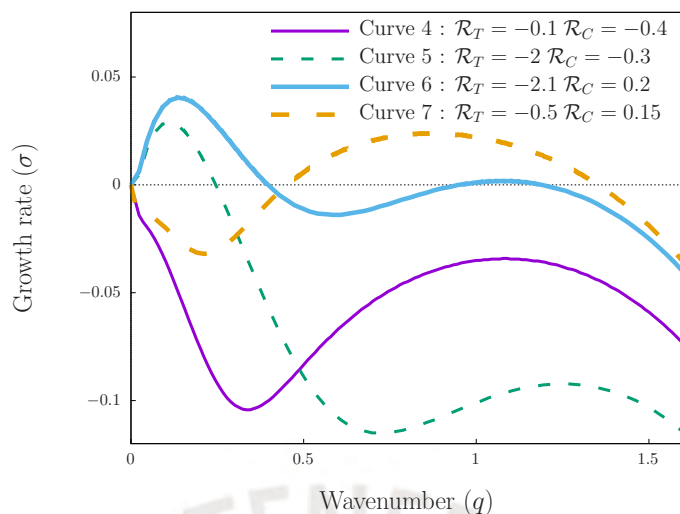


Figure 16: Dispersion relations for points with negative R_T . The curve numbers correspond to the points displayed in Fig. 2. The solid lines are the largest real part of the growth rate. All the corresponding growth rates have no imaginary part.

6.1.2 Nonlinear results

We solve the system of equations (4.93) in a vertical rectangular domain resembling a two-dimensional tube. If the domain is narrow, a convectionless flat front can propagate against gravity in the vertical y direction. The width of the tube L allows only perturbations of wavenumber q greater than π/L , which have a negative growth rate for large q . Increasing the width of the tube allows perturbations of smaller wavenumbers that may include positive growth rates. This takes place if the unbounded flat front is unstable, as determined by its dispersion relation. For tubes of width below a critical value L_c , all the allowed perturbations decay, consequently the front becomes flat. The flat front is unstable when the tube is wider than the critical value L_c . Near the transition, tubes wider than L_c lead to a curved front of steady shape propagating with constant speed. This is shown in Fig. 17 for different pairs of Rayleigh numbers having dispersion relations that allow instabilities. In this figure, we show the front speed relative to the flat front speed as a function of $\Delta L = L - L_c$, the difference between tube width and the corresponding critical value. Here we fix $\mathcal{R}_T = 0.5$ considering three different values of \mathcal{R}_C . For $\mathcal{R}_C = 0.2$ the critical width is $L_c = 2.05$, for $\mathcal{R}_C = 0$ it becomes $L_c = 2.6$, and for $\mathcal{R}_C = -0.2$ it corresponds to $L_c = 6.3$. These values show that decreasing \mathcal{R}_C increases L_c , a consequence of having a lower density fluid below the front. For values of L slightly above the critical value, all curves show an increase of speed. A higher value of \mathcal{R}_C also results in a higher speed due

to increased convection. Away from the transition, we notice different behaviors in each case. For $\mathcal{R}_C = 0.2$, the change of speed shows an inflection point not observed in the other curves. For a width just above the transition, we obtain a nonaxisymmetric curved front, as displayed in Fig. 18. In this figure $\mathcal{R}_C = 0.2$, with the other cases of 17 having similar shapes. In Fig. 18 (a), we show the velocity field in a region near the front. Here we observe a single convective roll centered just above the front. The fluid flow modifies the front, resulting in a non-axisymmetric shape. Figure 18 (b) shows the stream function on a larger region, exhibiting two convective rolls.

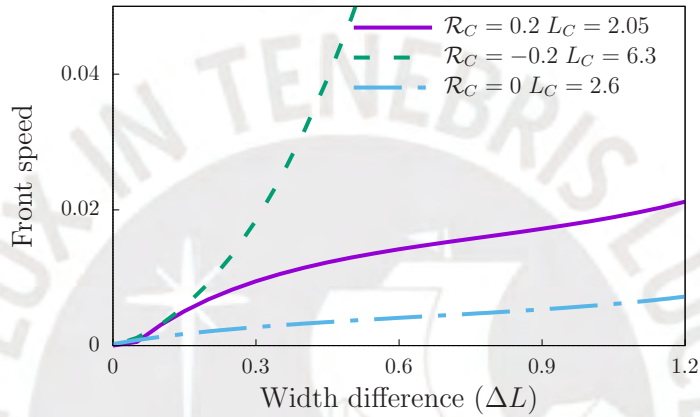


Figure 17: Front speed relative to the flat front speed as a function of $\Delta L = L - L_C$ for different values of \mathcal{R}_C and positive \mathcal{R}_T . We also display the case $\mathcal{R}_C = \mathcal{R}_T = 0$.

In the case of $\mathcal{R}_T = -2$ and $\mathcal{R}_C = -0.3$, the linear stability analysis shows that the front is unstable to convection even though the denser fluid is underneath the front. For these values, the nonlinear behavior is similar to the previous cases with positive \mathcal{R}_T . As we increase the tube width beyond a critical width, the front evolves into a constant nonaxisymmetric shape. This front propagates with a constant speed higher than the flat front speed (Fig. 19). The fluid velocity field develops two convective counter rotating rolls, one on top of the other, with the front located between the rolls (Fig. 20 (a)). In Fig. 20 (b), we display the stream function near the front, showing a faster rotation for the lower roll.

Changing the compositional Rayleigh number to a positive value ($\mathcal{R}_C = 0.15$), we find that the transition to convection takes place at a lower critical width than the previous negative \mathcal{R}_C (Fig. 21). This is a consequence of the increased buoyancy caused by the compositional changes on the density gradient. Near the transition, the speed of the front initially increases as a function of L , reaching a

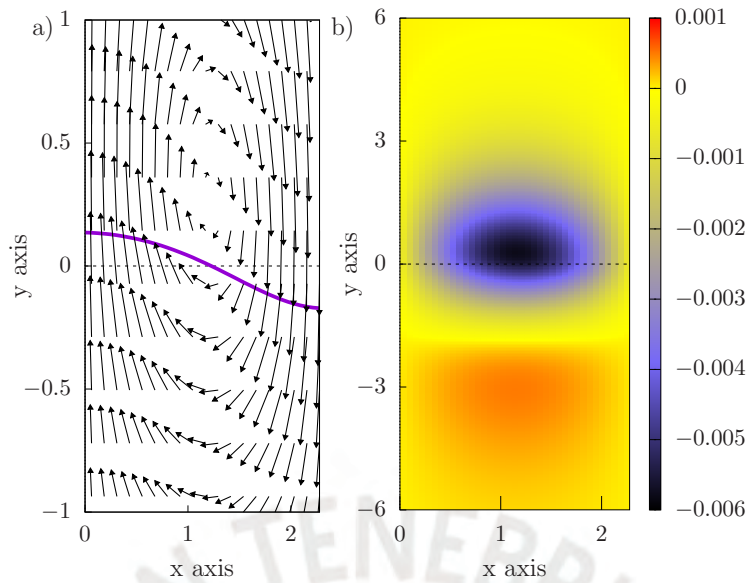


Figure 18: Velocity field and front profile (a) for $\mathcal{R}_T = 0.5$ and $\mathcal{R}_C = 0.2$, corresponding to point 1 of figure 14. The color map (b) shows the stream function on a longer region centered at the front, showing two convective rolls. This domain has width $L_x = 2.28$.

relative maximum. This increase and decrease of speed as a function of width is a similar behavior for fronts in the convectionless KS equation. [175, 176, 68] A second relative maximum appears as the width increases further. The shape of the front near the transition is nonaxisymmetric (Fig. 22), with the fluid motion corresponding to two counterrotating rolls, one above the other. The front is located inside the lower roll, with fluid rising on one side of the front, and falling on the opposite side. As the width of the tube increases, the shape of the front becomes axisymmetric, with the front tip near the center of the tube (Fig. 23 (a)). The front is located within two counterrotating rolls, with fluid rising near the center of the tube and falling near the sides. Two additional rolls form above the front as shown in Fig. 23 (b), with weaker convection than the lower rolls.

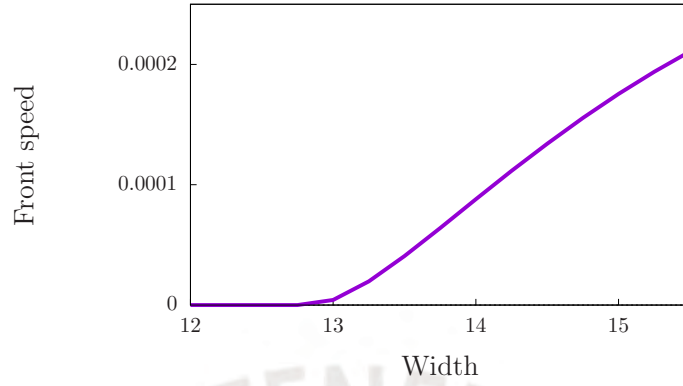


Figure 19: Front speed relative to the flat front speed as a function of the width L , for $\mathcal{R}_T = -2$ and $\mathcal{R}_C = -0.3$. Corresponding to point 5 of the figure 14.

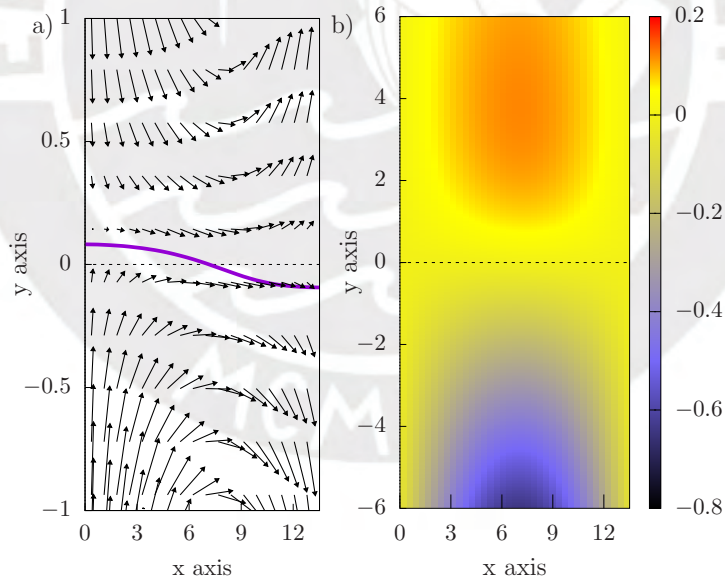


Figure 20: Velocity field and front profile (a) for $\mathcal{R}_T = -2$ and $\mathcal{R}_C = -0.3$, corresponding to point 5 of figure 14. The color map (b) shows the stream function on a longer region centered at the front, showing two convective rolls. This domain has width $L_x = 13.52$.

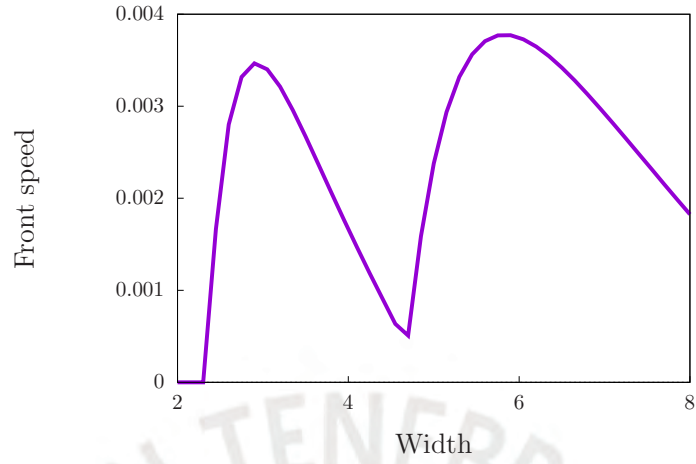


Figure 21: Front speed relative to the flat front speed as a function of the width L , for $\mathcal{R}_T = -0.5$ and $\mathcal{R}_C = 0.15$. Corresponding to point 7 of the figure 14.

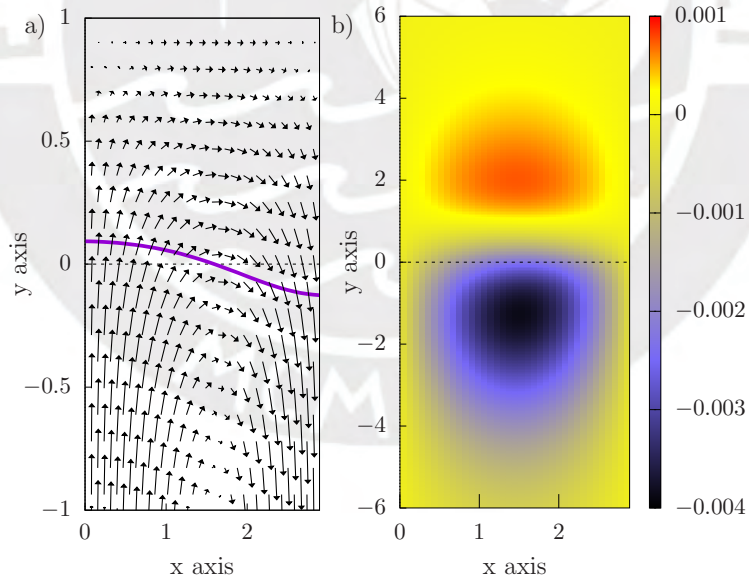


Figure 22: Velocity field and front profile (a) for $\mathcal{R}_T = -0.5$ and $\mathcal{R}_C = 0.15$, corresponding to point 7 of figure 14. The color map (b) shows the stream function on a longer region centered at the front, showing two convective rolls. This domain has width $L_x = 2.89$.

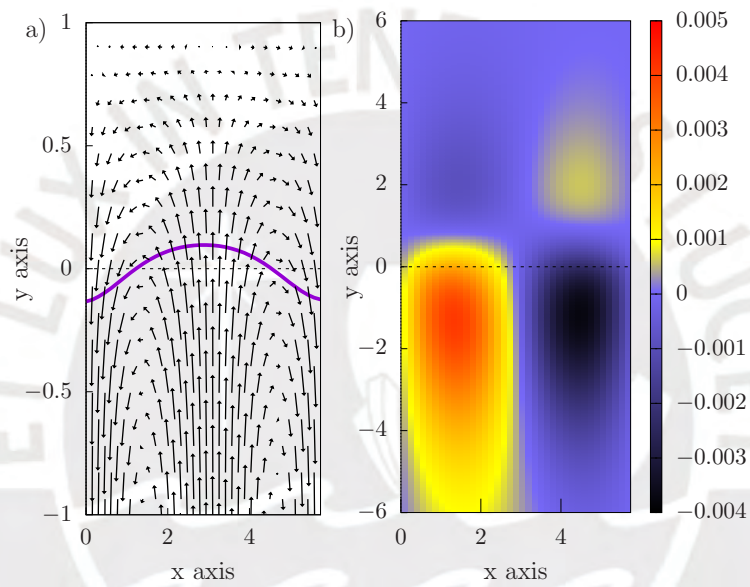


Figure 23: Velocity field and front profile (a) for $\mathcal{R}_T = -0.5$ and $\mathcal{R}_C = 0.15$, corresponding to point 7 of figure 14. The color map (b) shows the stream function on a longer region centered at the front, showing four convective rolls. This domain has width $L_x = 5.74$.

6.2 Summary and discussion

In this chapter, we studied the effects of fluid motion driven by density gradients on the stability of flat fronts. These fronts are described by the Kuramoto-Sivashinsky (KS) equation coupled to hydrodynamics. In this chapter, the unbounded KS front without convection exhibits instabilities with respect to small perturbations. The front separates fluids of different chemical concentrations and temperature, leading to density gradients across the front. Positive Rayleigh numbers for composition and temperature, representing a higher density above the front, enhance the front instability. In these cases, decreasing the density of the fluid below the front lead to instabilities. A negative compositional Rayleigh number tends to stabilize the front. Increasing the magnitude of a negative thermal Rayleigh number can initially help to stabilize the front. However, increasing it further results in an unstable front. In this configuration, the instability results from a denser fluid underneath a less dense fluid, contrary to what is expected. This result is similar to previous results for reaction-diffusion-advection fronts where the hydrodynamics was described by Darcy's law. [164]

The stability of a flat front propagating inside a two-dimensional narrow rectangular tube depends on the width. Flat fronts propagating inside narrow tubes are stable. In this case, the width of the tube only allows perturbations of short wavelengths, which always decay. When the width is increased, our nonlinear calculations show fronts of constant shape propagating with constant speed higher than the flat front speed. Near the transition to convection, the front is nonaxisymmetric, with fluid motion corresponding to two counter rotating rolls one on top of the other. In some cases, we found that increasing the width results in a maximum speed for the nonaxisymmetric front (Fig. 21). Increasing it even further results in a front shape with a tip near the middle, propagating with four convective rolls.

Our results showed that density gradients can stabilize reaction fronts such as the ones observed in diffusive instabilities. But at the same time, they can lead to unexpected instabilities for negative \mathcal{R}_T numbers, where the less dense fluid is above the denser fluid. Here we studied the interaction between instabilities in a front evolution equation and density driven convection. The transition to instability with $\mathcal{R}_C = 0$ corresponds to $\mathcal{R}_T = -0.985$, with a critical value of q near zero, corresponding to a large critical wavelength. An estimate using the parameters of the IAA reaction [126], assuming \mathcal{V} to be the molecular diffusivity, leads to a critical wavelength of 0.48 cm. The corresponding value of \mathcal{R}_T is -898, beyond the

onset of the instability. This estimate leaves out the fact that convectionless flat fronts in the IAA reaction are stable, which is not the case for fronts in the KS equation. A detailed comparison with experiments would require accurate knowledge of the fluid parameters, such as compositional and thermal density changes, heat losses, and three-dimensional effects. Further theoretical work, such as using unstable reaction-diffusion-advection fronts with different Lewis and Prandtl numbers, may reveal new dynamics.



7 Conclusions

This thesis showed new instabilities in the propagation of chemical fronts in viscous fluids. They arise from heat effects due to the chemical reaction, changing the density of the fluid.

In chapter 5, we showed the effects of heat loss through the boundaries of the domain, changing the temperature profile of the reaction front. We defined a dimensionless Biot number that describes the amount of heat loss through the boundaries. For insulating walls, the Biot number is zero and the temperature behind the front is constant. However, for nonzero Biot numbers the temperature behind the front decreases as heat is lost through the container walls. The temperature shows a maximum value halfway between the walls and near the reaction front. Thus for vertical propagation, there is a horizontal temperature gradient. This results in convection for all nonzero Biot numbers. In the presence of heat loss, we find a solution that has an axisymmetric shape, but close to the flat front solution with $Bi = 0$. For insulating walls ($Bi = 0$), the flat front solution is stable for small domain widths. As the Biot number increases, the front remains stable but becomes slightly axisymmetric. Increasing the width of the domain beyond a critical value, the stable state is a nonaxisymmetric front with speed higher than the flat front. The critical width for this transition increases as the Biot number increases. This means that small heat losses can inhibit the transition to the highly convective state with a nonaxisymmetric shape. For high Biot numbers, we did not find the transition for widths less than $L_x = 49$, but it can still take place at larger widths. We also studied the front propagation as a function of Biot number keeping the width constant. For a small domain width, the nonaxisymmetric front shape exists in a finite range of values of Biot numbers. Beyond a critical value of Biot numbers, there is only a low convection front with an almost symmetric shape. Increasing the Biot number further causes higher convection, but with a small increase in front velocity. For a higher domain width, we find a region of bistability between the nonaxisymmetric state and the slower axisymmetric front. In this bistability region, the final state of the system depends on the initial shape of the front and the temperature distribution. The region of bistability increases at larger domain widths, taking place at higher Biot numbers. In horizontal propagation, the front always has a nonaxisymmetric shape. For larger domain widths, the front speed shows an abrupt speed increase. The Biot number affects this transition to a high speed front, as was the case of vertical propagation.

In chapter 6, we described a thin front propagating in a viscous fluid according to

the KS equation. In this case, fluid flow is driven by thermal and compositional density changes. Two dimensionless Rayleigh numbers characterize the system, one for thermal and another for compositional effects. The KS equation describes an unstable flat front in the absence of convection, since perturbations of large wavelength have a positive growth rate. This instability persists for very small Rayleigh numbers independent of their sign. The flat front remains unstable if both Rayleigh numbers are positive. Positive Rayleigh numbers represent a fluid of higher density on top of a fluid of lower density, which is an unstable configuration. Therefore, we expect negative Rayleigh numbers to help to stabilize the front. We find that a negative compositional Rayleigh number by itself ($\mathcal{R}_T = 0$) can stabilize the flat front. However, using only a negative thermal Rayleigh number ($\mathcal{R}_C = 0$) can stabilize the front in a finite range of values. Initially, a certain value of negative thermal Rayleigh number leads to a stable flat front. However, decreasing beyond a critical value, the flat front becomes unstable. In this situation, the less dense fluid above the front induces the instability. In addition to the linear stability analysis, we study solutions of the nonlinear front evolution equation. As we increase the domain width, we find slight increases of speed beyond a critical value. The critical width is consistent with the prediction of the linear stability theory. The increase of speed is very small for negative thermal Rayleigh numbers. The shape of the convective pattern depends on the specific values of the Rayleigh numbers. While all of them exhibit two rolls around the front, the front position can be near the top roll, or near the bottom roll, or somewhere in between the rolls.

This thesis focused on the effects of thermal and compositional density gradients in propagating fronts with convection. The presence of heat loss is unavoidable in experiments. Our theory describes these effects using a dimensionless Biot number. We found that heat loss may lead to a bistability between two shapes of fronts. In the thin front approximation, the KS equation can be stabilized for some values of Rayleigh numbers. The linear stability analysis shows transitions to convection due to thermal and compositional density gradients. Thermal effects can generate an instability with a lesser dense fluid above a denser fluid separated by the front. These theoretical results aim to motivate experiments to test our predictions. Further theoretical work can lead to a better understanding of these instabilities.

References

- [1] Jerzy Maselko and Irving R. Epstein. Chemical chaos in the chlorite–thiosulfate reaction. *The Journal of Chemical Physics*, 80(7):3175–3178, April 1984.
- [2] Miklos Orban and Irving R. Epstein. Systematic design of chemical oscillators. Part 13. Complex periodic and aperiodic oscillation in the chlorite–thiosulfate reaction. *J. Phys. Chem.*, 86(20):3907–3910, September 1982.
- [3] Patrick De Kepper, Irving R. Epstein, and Kenneth Kustin. A systematically designed homogeneous oscillating reaction: The arsenite-iodate-chlorite system. *J. Am. Chem. Soc.*, 103(8):2133–2134, April 1981.
- [4] Irving R. Epstein, Irving Robert Epstein, John Anthony Pojman, and John A. Pojman. *An Introduction to Nonlinear Chemical Dynamics: Oscillations, Waves, Patterns, and Chaos*. Topics in Physical Chemistry. Oxford University Press, New York, 1998.
- [5] Y. Kuramoto and T. Tsuzuki. Persistent Propagation of Concentration Waves in Dissipative Media Far from Thermal Equilibrium. *Progress of Theoretical Physics*, 55(2):356–369, February 1976.
- [6] T. Yamada and Y. Kuramoto. A Reduced Model Showing Chemical Turbulence. *Progress of Theoretical Physics*, 56(2):681–683, August 1976.
- [7] Peter Ortoleva and John Ross. Theory of propagation of discontinuities in kinetic systems with multiple time scales: Fronts, front multiplicity, and pulses. *The Journal of Chemical Physics*, 63(8):3398–3408, October 1975.
- [8] Alan Turing. The chemical basis of morphogenesis. *Phil. Trans. R. Soc. Lond. B*, 237(641):37–72, August 1952.
- [9] V. Castets, E. Dulos, J. Boissonade, and P. De Kepper. Experimental evidence of a sustained standing Turing-type nonequilibrium chemical pattern. *Phys. Rev. Lett.*, 64(24):2953–2956, June 1990.
- [10] Stephen K. Scott and Kenneth Showalter. Simple and complex propagating

- reaction-diffusion fronts. *J. Phys. Chem.*, 96(22):8702–8711, October 1992.
- [11] George H. Markstein. Experimental and Theoretical Studies of Flame-Front Stability. *Journal of the Aeronautical Sciences*, 18(3):199–209, March 1951.
- [12] G. I. Sivashinsky. Diffusional-Thermal Theory of Cellular Flames. *Combustion Science and Technology*, 15(3-4):137–145, January 1977.
- [13] Paul Clavin. Dynamic behavior of premixed flame fronts in laminar and turbulent flows. *Progress in Energy and Combustion Science*, 11(1):1–59, January 1985.
- [14] O. Séro-Guillaume, S. Ramezani, J. Margerit, and D. Calogine. On large scale forest fires propagation models. *International Journal of Thermal Sciences*, 47(6):680–694, June 2008.
- [15] Benjamin A. Suslick, Julie Hemmer, Brecklyn R. Groce, Katherine J. Stawiasz, Philippe H. Geubelle, Giulio Malucelli, Alberto Mariani, Jeffrey S. Moore, John A. Pojman, and Nancy R. Sottos. Frontal Polymerizations: From Chemical Perspectives to Macroscopic Properties and Applications. *Chem. Rev.*, 123(6):3237–3298, March 2023.
- [16] C.W. Lan. Recent progress of crystal growth modeling and growth control. *Chemical Engineering Science*, 59(7):1437–1457, April 2004.
- [17] W. W. Mullins and R. F. Sekerka. Stability of a Planar Interface During Solidification of a Dilute Binary Alloy. *Journal of Applied Physics*, 35(2):444–451, February 1964.
- [18] Muhammad Kashif Aslam, Yubin Niu, Tanveer Hussain, Hassina Tabassum, Wenwen Tang, Maowen Xu, and Rajeev Ahuja. How to avoid dendrite formation in metal batteries: Innovative strategies for dendrite suppression. *Nano Energy*, 86:106142, August 2021.
- [19] Joaquim Fort and Toni Pujol. Progress in front propagation research. *Rep. Prog. Phys.*, 71(8):086001, August 2008.
- [20] Kaifa Wang and Wendi Wang. Propagation of HBV with spatial dependence.

Mathematical Biosciences, 210(1):78–95, November 2007.

- [21] P.G. Kevrekidis, Travis B. Thompson, and Alain Goriely. Anisotropic diffusion and traveling waves of toxic proteins in neurodegenerative diseases. *Physics Letters A*, 384(36):126935, December 2020.
- [22] Rebecca A. B. Burton, Aleksandra Klimas, Christina M. Ambrosi, Jakub Tomek, Alex Corbett, Emilia Entcheva, and Gil Bub. Optical control of excitation waves in cardiac tissue. *Nature Photon*, 9(12):813–816, December 2015.
- [23] Ágota Tóth, Dezsó Horváth, and Andrea Siska. Velocity of propagation in reaction–diffusion fronts of the chlorite–tetrathionate reaction. *Faraday Trans.*, 93(1):73–76, 1997.
- [24] David M. Weitz and Irving R. Epstein. Spatial waves in the reaction of chlorite with iodide. *J. Phys. Chem.*, 88(22):5300–5304, October 1984.
- [25] John A. Pojman, Istvan P. Nagy, and Irving R. Epstein. Convective effects on chemical waves. 3. Multicomponent convection in the iron(II)-nitric acid system. *J. Phys. Chem.*, 95(3):1306–1311, February 1991.
- [26] Adel Hanna, Alan Saul, and Kenneth Showalter. Detailed studies of propagating fronts in the iodate oxidation of arsenous acid. *J. Am. Chem. Soc.*, 104(14):3838–3844, July 1982.
- [27] Edward J. Reusser and Richard J. Field. The transition from phase waves to trigger waves in a model of the Zhabotinskii reaction. *J. Am. Chem. Soc.*, 101(5):1063–1071, February 1979.
- [28] Richard J. Field, editor. *Oscillations and Traveling Waves in Chemical Systems*. A Wiley-Interscience Publication. Wiley, New York, 1985.
- [29] Patricia Dähmow, Vladimir K. Vanag, and Stefan C. Müller. Effect of solvents on the pattern formation in a Belousov-Zhabotinsky reaction embedded into a microemulsion. *Phys. Rev. E*, 89(1):010902, January 2014.
- [30] John J. Tyson and Paul C. Fife. Target patterns in a realistic model

- of the Belousov–Zhabotinskii reaction. *The Journal of Chemical Physics*, 73(5):2224–2237, September 1980.
- [31] Arthur T. Winfree. Rotating Chemical Reactions. *Sci Am*, 230(6):82–95, June 1974.
- [32] M A Budroni, F Wodlei, and M Rustici. Butterfly effect in a chemical oscillator. *Eur. J. Phys.*, 35(4):045005, July 2014.
- [33] László Györgyi and Richard J. Field. A three-variable model of deterministic chaos in the Belousov–Zhabotinsky reaction. *Nature*, 355(6363):808–810, February 1992.
- [34] Boyd F. Edwards. Poiseuille Advection of Chemical Reaction Fronts. *Phys. Rev. Lett.*, 89(10):104501, August 2002.
- [35] M. Leconte, J. Martin, N. Rakotomalala, and D. Salin. Pattern of Reaction Diffusion Front in Laminar Flows. *Phys. Rev. Lett.*, 90(12):128302, March 2003.
- [36] C. R. Nugent, W. M. Quarles, and T. H. Solomon. Experimental Studies of Pattern Formation in a Reaction-Advection-Diffusion System. *Phys. Rev. Lett.*, 93(21):218301, November 2004.
- [37] Hidetoshi Miike, Hideaki Yamamoto, Shoichi Kai, and Stefan C. Müller. Accelerating chemical waves accompanied by traveling hydrodynamic motion and surface deformation. *Phys. Rev. E*, 48(3):R1627–R1630, September 1993.
- [38] H.J. Kull. Theory of the Rayleigh-Taylor instability. *Physics Reports*, 206(5):197–325, August 1991.
- [39] Yunqing Wu, Desiderio A. Vasquez, Boyd F. Edwards, and Joseph W. Wilder. Convective chemical-wave propagation in the Belousov-Zhabotinsky reaction. *Phys. Rev. E*, 51(2):1119–1127, February 1995.
- [40] John A. Pojman, Irving R. Epstein, Terence J. McManus, and Kenneth Showalter. Convective effects on chemical waves. 2. Simple convection in

- the iodate-arsenous acid system. *J. Phys. Chem.*, 95(3):1299–1306, February 1991.
- [41] J. Martin, N. Rakotomalala, D. Salin, and M. Böckmann. Buoyancy-driven instability of an autocatalytic reaction front in a Hele-Shaw cell. *Phys. Rev. E*, 65(5):051605, May 2002.
- [42] I. Bou Malham, N. Jarrige, J. Martin, N. Rakotomalala, L. Talon, and D. Salin. Lock-exchange experiments with an autocatalytic reaction front. *The Journal of Chemical Physics*, 133(24):244505, December 2010.
- [43] J. Yang, A. D’Onofrio, S. Kalliadasis, and A. De Wit. Rayleigh–Taylor instability of reaction-diffusion acidity fronts. *The Journal of Chemical Physics*, 117(20):9395–9408, November 2002.
- [44] S. Chandrasekhar. *Hydrodynamic and Hydromagnetic Stability*. Dover Publications, New York, dover ed edition, 1981.
- [45] Kerstin Eckert, Michael Bestehorn, and André Thess. Square cells in surface-tension-driven Bénard convection: Experiment and theory. *J. Fluid Mech.*, 356:155–197, February 1998.
- [46] Gábor Schuszter, Gábor Pótári, Dezső Horváth, and Ágota Tóth. Three-dimensional convection-driven fronts of the exothermic chlorite-tetrathionate reaction. *Chaos: An Interdisciplinary Journal of Nonlinear Science*, 25(6):064501, June 2015.
- [47] Istvan. Nagypal, Gyorgy. Bazsa, and Irving R. Epstein. Gravity-induced anisotropies in chemical waves. *J. Am. Chem. Soc.*, 108(13):3635–3640, June 1986.
- [48] J. Martin, N. Rakotomalala, L. Talon, and D. Salin. Measurement of the temperature profile of an exothermic autocatalytic reaction front. *Phys. Rev. E*, 80(5):055101, November 2009.
- [49] J. D’Heroncourt, A. Zebib, and A. De Wit. Reaction Driven Convection around a Stably Stratified Chemical Front. *Phys. Rev. Lett.*, 96(15):154501, April 2006.

- [50] Pablo M. Vilela, Roberto Guzman, and Desiderio A. Vasquez. Thermally Driven Convection Generated by Reaction Fronts in Viscous Fluids. *Symmetry*, 16(3):269, February 2024.
- [51] Éva Pópity-Tóth, Véronique Pimienta, Dezső Horváth, and Ágota Tóth. Hydrodynamic instability in the open system of the iodate–arsenous acid reaction. *The Journal of Chemical Physics*, 139(16):164707, October 2013.
- [52] Federico Rossi, Marcello A. Budroni, Nadia Marchettini, and Jorge Carballido-Landeira. Segmented waves in a reaction-diffusion-convection system. *Chaos: An Interdisciplinary Journal of Nonlinear Science*, 22(3):037109, September 2012.
- [53] P. Bába, L. Rongy, A. De Wit, M. J. B. Hauser, Á. Tóth, and D. Horváth. Interaction of Pure Marangoni Convection with a Propagating Reactive Interface under Microgravity. *Phys. Rev. Lett.*, 121(2):024501, July 2018.
- [54] L. Rongy, A. De Wit, and G. M. Homsy. Asymptotic structure of steady nonlinear reaction-diffusion-Marangoni convection fronts. *Physics of Fluids*, 20(7):072103, July 2008.
- [55] Roberto Guzman and Desiderio A. Vasquez. Surface tension driven flow on a thin reaction front. *The European Physical Journal Special Topics*, 225(13-14):2573–2580, November 2016.
- [56] James P. Keener and John J. Tyson. Spiral waves in the Belousov-Zhabotinskii reaction. *Physica D: Nonlinear Phenomena*, 21(2-3):307–324, September 1986.
- [57] Jie Huang, Desiderio A. Vasquez, Boyd F. Edwards, and Paul Kolodner. Onset of convection for autocatalytic reaction fronts in a vertical slab. *Phys. Rev. E*, 48(6):4378–4386, December 1993.
- [58] Roberto Guzman and Desiderio A. Vasquez. Marangoni flow traveling with reaction fronts: Eikonal approximation. *Chaos*, 27(10):103121, October 2017.
- [59] Desiderio A. Vasquez, Joseph W. Wilder, and Boyd F. Edwards. Convective

- instability of autocatalytic reaction fronts in vertical cylinders. *Physics of Fluids A: Fluid Dynamics*, 4(11):2410–2414, November 1992.
- [60] Jonathan Masere, Desiderio A. Vasquez, Boyd F. Edwards, Joseph W. Wilder, and Kenneth Showalter. Nonaxisymmetric and Axisymmetric Convection in Propagating Reaction-Diffusion Fronts. *J. Phys. Chem.*, 98(26):6505–6508, June 1994.
- [61] Dezső Horváth and Kenneth Showalter. Instabilities in propagating reaction-diffusion fronts of the iodate-arsenous acid reaction. *The Journal of Chemical Physics*, 102(6):2471–2478, February 1995.
- [62] M.R. Alharthi, T.R. Marchant, and M.I. Nelson. Mixed quadratic-cubic autocatalytic reaction–diffusion equations: Semi-analytical solutions. *Applied Mathematical Modelling*, 38(21-22):5160–5173, November 2014.
- [63] Anatoly Malevanets, Agustí Careta, and Raymond Kapral. Biscala chaos in propagating fronts. *Phys. Rev. E*, 52(5):4724–4735, November 1995.
- [64] Edwin A. Llamoca, P. M. Vilela, and Desiderio A. Vasquez. Instabilities in cubic reaction–diffusion fronts advected by a Poiseuille flow. *Eur. Phys. J. Spec. Top.*, 231(3):505–511, April 2022.
- [65] J. D’Heroncourt, J. H. Merkin, and A. De Wit. Interaction between buoyancy and diffusion-driven instabilities of propagating autocatalytic reaction fronts. I. Linear stability analysis. *The Journal of Chemical Physics*, 130(11):114502, March 2009.
- [66] J. D’Heroncourt, J. H. Merkin, and A. De Wit. Interaction between buoyancy and diffusion-driven instabilities of propagating autocatalytic reaction fronts. II. Nonlinear simulations. *The Journal of Chemical Physics*, 130(11):114503, March 2009.
- [67] Drew Elliott and Desiderio A. Vasquez. Convection in stable and unstable fronts. *Physical Review E*, 85(1), January 2012.
- [68] P. M. Vilela and Desiderio A. Vasquez. Stability of fronts in the Kuramoto-Sivashinsky equation advected by a Poiseuille flow. *Phys. Rev.*

E, 86(6):066102, December 2012.

- [69] Roberto Guzman, P. M. Vilela, and Desiderio A. Vasquez. Fronts described by the Kuramoto–Sivashinsky equation under surface tension driven flow. *Eur. Phys. J. Spec. Top.*, 227(5-6):521–531, September 2018.
- [70] Roberto Guzman and Desiderio A. Vasquez. Thermal convection in reaction fronts confined between conductive walls. *Meccanica*, March 2024.
- [71] Roberto Guzman and Desiderio A. Vasquez. Front instabilities in the presence of convection due to thermal and compositional gradients. *Chaos: An Interdisciplinary Journal of Nonlinear Science*, 34(1):013123, January 2024.
- [72] Lawrence E. Malvern. *Introduction to the Mechanics of a Continuous Medium*. Prentice-Hall Series in Engineering of the Physical Sciences. Prentice-Hall, Englewood Cliffs, N.J, 1969.
- [73] Rutherford Aris. *Vectors, Tensors, and the Basic Equations of Fluid Mechanics*. Dover Books on Engineering. Dover Publications, New York, dover ed edition, 1989.
- [74] Richard L. Bishop and Samuel I. Goldberg. *Tensor Analysis on Manifolds*. Dover, New York, 1980.
- [75] Harley Flanders. *Differential Forms with Applications to the Physical Sciences*. Dover Publications, Mineola, N.Y, 1989.
- [76] R. W. R. Darling. *Differential Forms and Connections*. Cambridge University Press, Cambridge ; New York, NY, USA, 1994.
- [77] George B. Arfken, Hans-Jurgen Weber, and Frank E. Harris. *Mathematical Methods for Physicists: A Comprehensive Guide*. Elsevier, AP, Amsterdam Boston Heidelberg London New York Oxford Paris San Diego San Francisco Singapore Sydney Tokyo, seventh edition edition, 2013.
- [78] Frederick W. Byron and Robert W. Fuller. *Mathematics of Classical and Quantum Physics*. Dover Publications, New York, 1992.

- [79] Peter J. Olver. *Introduction to Partial Differential Equations*. Springer Science+Business Media, LLC, New York, NY, 2013.
- [80] G. B. Whitham. *Linear and Nonlinear Waves*. Pure and Applied Mathematics. Wiley, New York, 1974.
- [81] R. F. Hoskins. *Delta Functions: An Introduction to Generalised Functions*. Horwood Pub, Chichester, UK, 2nd ed edition, 2009.
- [82] *Brain Dynamics an Introduction to Models and Simulations*. Springer, Berlin [u.a.], 2. ed edition, 2010.
- [83] Gerd Grubb. *Distributions and Operators*. Number 252 in Graduate Texts in Mathematics. Springer, New York, 2009.
- [84] D J Griffiths. Boundary conditions at the derivative of a delta function. *J. Phys. A: Math. Gen.*, 26(9):2265–2267, May 1993.
- [85] Ronald N. Bracewell. *The Fourier Transform and Its Applications*. McGraw-Hill Series in Electrical and Computer Engineering. McGraw Hill, Boston, 3rd ed edition, 2000.
- [86] Lars Hörmander. *The Analysis of Linear Partial Differential Operators. 1: Distribution Theory and Fourier Analysis*. Classics in Mathematics. Springer, Berlin Heidelberg, repr. of the 2. ed edition, 2003.
- [87] Steven E.. Koonin and Dawn C.. Meredith. *Computational Physics: Fortran Version*. London : New York : CRC Press, Boca Raton, 2019.
- [88] Tao Pang. *An Introduction to Computational Physics*. Cambridge University Press, Cambridge, 2nd ed edition, 2006.
- [89] Philip J. Davis and Philip Rabinowitz. *Methods of Numerical Integration*. Computer Science and Applied Mathematics. Academic Press, Orlando, 2nd ed edition, 1984.
- [90] Randall J. LeVeque. *Finite Difference Methods for Ordinary and Partial Differential Equations: Steady-State and Time-Dependent Problems*. Society

for Industrial and Applied Mathematics (SIAM, 3600 Market Street, Floor 6, Philadelphia, PA 19104), Philadelphia, Pa., 2007.

- [91] V. S. Riaben'kiĭ and Semyon V. Tsynkov. *A Theoretical Introduction to Numerical Analysis*. Chapman & Hall/CRC, Boca Raton, FL, 2007.
- [92] J. A. Robinson and Andrei Voronkov, editors. *Handbook of Automated Reasoning*. Elsevier ; MIT Press, Amsterdam ; New York : Cambridge, Mass, 2001.
- [93] John C. Strikwerda. *Finite Difference Schemes and Partial Differential Equations*. Society for Industrial and Applied Mathematics, Philadelphia, 2nd ed edition, 2004.
- [94] D. W. Peaceman and H. H. Rachford, Jr. The Numerical Solution of Parabolic and Elliptic Differential Equations. *Journal of the Society for Industrial and Applied Mathematics*, 3(1):28–41, March 1955.
- [95] A. R. Paterson. *A First Course in Fluid Dynamics*. Cambridge University Press, Cambridge ; New York, 1983.
- [96] Ronald L. Panton. *Incompressible Flow*. John Wiley and Sons, Inc, Hoboken, New Jersey, fourth edition edition, 2013.
- [97] Harold Jeffreys. *Cartesian Tensors*. Cambridge Science Classics. Cambridge Univ. Press, Cambridge, repr edition, 1987.
- [98] R M Brannon. *Rotation, Reflection, and Frame Changes: Orthogonal Tensors in Computational Engineering Mechanics*. IOP Publishing, April 2018.
- [99] Iain G. Currie. *Fundamental Mechanics of Fluids*. CRC Press, Boca Raton, Fla., 4th ed edition, 2013.
- [100] Radyadour Kh. Zeytounian. Joseph Boussinesq and his approximation: A contemporary view. *Comptes Rendus Mécanique*, 331(8):575–586, August 2003.
- [101] Antonio Barletta, Michele Celli, and D. Andrew S. Rees. On the Use and

- Misuse of the Oberbeck–Boussinesq Approximation. *Physics*, 5(1):298–309, March 2023.
- [102] Joseph George Coffin. *Vector Analysis: An Introduction to Vector-Methods and Their Various Applications to Physics and Mathematics*. N.D., Place of publication not identified, 2010.
- [103] H. Tennekes and John L. Lumley. *A First Course in Turbulence*. MIT Press, Cambridge, Mass, 1972.
- [104] Geoffrey B. West. *Scale: The Universal Laws of Growth, Innovation, Sustainability, and the Pace of Life in Organisms, Cities, Economies, and Companies*. Penguin Press, New York, 2017.
- [105] Michael A.B. Deakin. G.I. Taylor and the Trinity test. *International Journal of Mathematical Education in Science and Technology*, 42(8):1069–1079, December 2011.
- [106] R. W. Robinett. Dimensional analysis as the *other* language of physics. *American Journal of Physics*, 83(4):353–361, April 2015.
- [107] E. M. Purcell. Life at low Reynolds number. *American Journal of Physics*, 45(1):3–11, January 1977.
- [108] Guillermo A. Narsilio, Olivier Buzzi, Stephen Fityus, Tae Sup Yun, and David W. Smith. Upscaling of Navier–Stokes equations in porous media: Theoretical, numerical and experimental approach. *Computers and Geotechnics*, 36(7):1200–1206, September 2009.
- [109] P. G. Saffman and Geoffrey Taylor. The Penetration of a Fluid into a Porous Medium or Hele-Shaw Cell Containing a More Viscous Liquid. *Proceedings of the Royal Society of London. Series A, Mathematical and Physical Sciences*, 245(1242):312–329, 1958.
- [110] P. M. Vilela. *Propagating Reaction Fronts in Moving Fluids*. PhD thesis, PUCP, Lima, Perú, 2015.
- [111] Jie Zeng, Yannis C. Yortsos, and Dominique Salin. On the Brinkman correc-

- tion in unidirectional Hele-Shaw flows. *Physics of Fluids*, 15(12):3829–3836, December 2003.
- [112] John H. Lienhard and John H. Lienhard. *A Heat Transfer Textbook*. Dover Publications, Inc, Mineola, New York, fifth edition edition, 2019.
- [113] K. C. Cheng. Some Observations on the Origins of Newton’s Law of Cooling and Its Influences on Thermofluid Science. *Applied Mechanics Reviews*, 62(6):060803, November 2009.
- [114] E. L. Cussler. *Diffusion: Mass Transfer in Fluid Systems*. Cambridge University Press, Cambridge ; New York, 3rd ed edition, 2009.
- [115] John Crank. *The Mathematics of Diffusion*. Univ. Pr, Oxford, 2. ed., repr edition, 2011.
- [116] Raj K. Pathria and Paul D. Beale. *Statistical Mechanics*. Academic Press, an imprint of Elsevier, London San Diego Cambridge, MA Oxford, fourth edition edition, 2022.
- [117] R. A. Fisher. The Wave of Advance of Advantageous Genes. *Annals of Eugenics*, 7(4):355–369, June 1937.
- [118] Kenneth Showalter. Quadratic and Cubic Reaction–Diffusion Fronts. *Non-linear Science Today*, 4(4):8, 1995.
- [119] A. N. Kolmogorov. *Selected Works I: Mathematics and Mechanics*. Springer, The Netherlands, 2019.
- [120] Mark J. Ablowitz and Anthony Zeppetella. Explicit solutions of Fisher’s equation for a special wave speed. *Bltm Mathcal Biology*, 41(6):835–840, November 1979.
- [121] John J. Tyson and Pavel K. Brazhnik. On Traveling Wave Solutions of Fisher’s Equation in Two Spatial Dimensions. *SIAM J. Appl. Math.*, 60(2):371–391, January 2000.
- [122] Kenneth Showalter and John J. Tyson. Luther’s 1906 discovery and analysis

- of chemical waves. *J. Chem. Educ.*, 64(9):742, September 1987.
- [123] J H. Merkin and H Ševčíková. Travelling waves in the iodate–arsenous acid system. *Phys. Chem. Chem. Phys.*, 1(1):91–97, 1999.
- [124] Jordi García-Ojalvo and Jose M. Sancho. *Noise in Spatially Extended Systems*. Institute for Nonlinear Science. Springer, New York, 1999.
- [125] L. Rongy, N. Goyal, E. Meiburg, and A. De Wit. Buoyancy-driven convection around chemical fronts traveling in covered horizontal solution layers. *The Journal of Chemical Physics*, 127(11):114710, September 2007.
- [126] Boyd F. Edwards, Joseph W. Wilder, and Kenneth Showalter. Onset of convection for autocatalytic reaction fronts: Laterally unbounded system. *Phys. Rev. A*, 43(2):749–760, January 1991.
- [127] James P. Keener. A Geometrical Theory for Spiral Waves in Excitable Media. *SIAM J. Appl. Math.*, 46(6):1039–1056, December 1986.
- [128] Y. Kuramoto. Instability and Turbulence of Wavefronts in Reaction-Diffusion Systems. *Progress of Theoretical Physics*, 63(6):1885–1903, June 1980.
- [129] Joseph W. Wilder, Boyd F. Edwards, Desiderio A. Vasquez, and Gregory I. Sivashinsky. Derivation of a nonlinear front evolution equation for chemical waves involving convection. *Physica D: Nonlinear Phenomena*, 73(3):217–226, June 1994.
- [130] Desiderio A. Vasquez and Dan I. Coroian. Stability of convective patterns in reaction fronts: A comparison of three models. *Chaos: An Interdisciplinary Journal of Nonlinear Science*, 20(3):033109, September 2010.
- [131] N. Jarrige, I. Bou Malham, J. Martin, N. Rakotomalala, D. Salin, and L. Talon. Numerical simulations of a buoyant autocatalytic reaction front in tilted Hele-Shaw cells. *Phys. Rev. E*, 81(6):066311, June 2010.
- [132] Robert S. Spangler and Boyd F. Edwards. Poiseuille advection of chemical reaction fronts: Eikonal approximation. *The Journal of Chemical Physics*,

118(13):5911–5915, April 2003.

- [133] Jeremy Quastel and Herbert Spohn. The one-dimensional KPZ equation and its universality class. *J Stat Phys*, 160(4):965–984, August 2015.
- [134] Dezső Horváth, Valery Petrov, Stephen K. Scott, and Kenneth Showalter. Instabilities in propagating reaction-diffusion fronts. *The Journal of Chemical Physics*, 98(8):6332–6343, April 1993.
- [135] Demetrios T. Papageorgiou and Yiorgos S. Smyrlis. The route to chaos for the Kuramoto-Sivashinsky equation. *Theoret. Comput. Fluid Dynamics*, 3(1):15–42, September 1991.
- [136] L. Rongy and A. De Wit. Buoyancy-driven convection around exothermic autocatalytic chemical fronts traveling horizontally in covered thin solution layers. *The Journal of Chemical Physics*, 131(18):184701, November 2009.
- [137] Desiderio A. Vasquez, Joseph M. Littley, Joseph W. Wilder, and Boyd F. Edwards. Convection in chemical waves. *Phys. Rev. E*, 50(1):280–284, July 1994.
- [138] M. Leconte, J. Martin, N. Rakotomalala, D. Salin, and Y. C. Yortsos. Mixing and reaction fronts in laminar flows. *The Journal of Chemical Physics*, 120(16):7314–7321, April 2004.
- [139] D. J. Tritton. *Physical Fluid Dynamics*. Oxford Science Publications. Clarendon Press ; Oxford University Press, Oxford [England] : New York, 2nd ed edition, 1988.
- [140] T. L. Bergman, Adrienne Lavine, and Frank P. Incropera. *Fundamentals of Heat and Mass Transfer*. John Wiley & Sons, Inc., Hoboken, NJ, eighth edition edition, 2017.
- [141] J. D’Hernoncourt, A. De Wit, and A. Zebib. Double-diffusive instabilities of autocatalytic chemical fronts. *J. Fluid Mech.*, 576:445–456, April 2007.
- [142] Joseph W. Wilder, Boyd F. Edwards, and Desiderio A. Vasquez. Finite thermal diffusivity at onset of convection in autocatalytic systems: Continuous

- fluid density. *Phys. Rev. A*, 45(4):2320–2327, February 1992.
- [143] E. Anderson, editor. *LAPACK Users' Guide*. Software, Environments, Tools. Society for Industrial and Applied Mathematics, Philadelphia, 3rd ed edition, 1999.
- [144] John A. Pojman, Richard Craven, Akhtar Khan, and William West. Convective instabilities in traveling fronts of addition polymerization. *J. Phys. Chem.*, 96(18):7466–7472, September 1992.
- [145] Desiderio A. Vasquez, Boyd F. Edwards, and Joseph W. Wilder. Finite thermal diffusivity at onset of convection in autocatalytic systems: Discontinuous fluid density. *Physics of Fluids*, 7(10):2513–2515, October 1995.
- [146] L. Šebestíková and M. J. B. Hauser. Buoyancy-driven convection may switch between reactive states in three-dimensional chemical waves. *Phys. Rev. E*, 85(3):036303, March 2012.
- [147] Tamara Tóth, Dezső Horváth, and Ágota Tóth. Thermal effects in the density fingering of the chlorite–tetrathionate reaction. *Chemical Physics Letters*, 442(4-6):289–292, July 2007.
- [148] Tamás Bánsági, Dezső Horváth, and Ágota Tóth. Multicomponent convection in the chlorite–tetrathionate reaction. *Chemical Physics Letters*, 384(1-3):153–156, January 2004.
- [149] David R. A. Ruelas Paredes and Desiderio A. Vasquez. Convection induced by thermal gradients on thin reaction fronts. *Physical Review E*, 96(3), September 2017.
- [150] S. Mukherjee and M.R. Paul. The fluid dynamics of propagating fronts with solutal and thermal coupling. *J. Fluid Mech.*, 942:A36, July 2022.
- [151] S. Mukherjee and M. R. Paul. Velocity and geometry of propagating fronts in complex convective flow fields. *Phys. Rev. E*, 99(1):012213, January 2019.
- [152] E. Goli, S.R. Peterson, and P.H. Geubelle. Instabilities driven by frontal polymerization in thermosetting polymers and composites. *Composites Part*

B: Engineering, 199:108306, October 2020.

- [153] T. Gérard and A. De Wit. Stability of exothermic autocatalytic fronts with regard to buoyancy-driven instabilities in presence of heat losses. *Wave Motion*, 48(8):814–823, December 2011.
- [154] J. D’Hernoncourt, S. Kalliadasis, and A. De Wit. Fingering of exothermic reaction-diffusion fronts in Hele-Shaw cells with conducting walls. *The Journal of Chemical Physics*, 123(23):234503, December 2005.
- [155] J. D’Hernoncourt and A. De Wit. Influence of heat losses on nonlinear fingering dynamics of exothermic autocatalytic fronts. *Physica D: Nonlinear Phenomena*, 239(11):819–830, June 2010.
- [156] L. Šebestíková, J. D’Hernoncourt, M. J. B. Hauser, S. C. Müller, and A. De Wit. Flow-field development during finger splitting at an exothermic chemical reaction front. *Phys. Rev. E*, 75(2):026309, February 2007.
- [157] L. Rongy, N. Goyal, E. Meiburg, and A. De Wit. Buoyancy-driven convection around chemical fronts traveling in covered horizontal solution layers. *The Journal of Chemical Physics*, 127(11):114710, September 2007.
- [158] S. Mukherjee and M. R. Paul. Propagating fronts in fluids with solutal feedback. *Phys. Rev. E*, 101(3):032214, March 2020.
- [159] Martin Böckmann and Stefan C. Müller. Growth Rates of the Buoyancy-Driven Instability of an Autocatalytic Reaction Front in a Narrow Cell. *Phys. Rev. Lett.*, 85(12):2506–2509, September 2000.
- [160] Dezső Horváth, Tamás Bánsági, and Ágota Tóth. Orientation-dependent density fingering in an acidity front. *The Journal of Chemical Physics*, 117(9):4399–4402, September 2002.
- [161] L. Rongy, G. Schuszter, Z. Sinkó, T. Tóth, D. Horváth, A. Tóth, and A. De Wit. Influence of thermal effects on buoyancy-driven convection around autocatalytic chemical fronts propagating horizontally. *Chaos: An Interdisciplinary Journal of Nonlinear Science*, 19(2):023110, June 2009.

- [162] Desiderio A. Vasquez, Joseph M. Littley, Joseph W. Wilder, and Boyd F. Edwards. Convection in chemical waves. *Phys. Rev. E*, 50(1):280–284, July 1994.
- [163] Joseph Wilder, Desiderio Vasquez, and Boyd Edwards. Nonlinear front evolution of hydrodynamic chemical waves in vertical cylinders. *Phys. Rev. E*, 56(3):3016–3020, September 1997.
- [164] J. D’Heroncourt, A. Zebib, and A. De Wit. Reaction Driven Convection around a Stably Stratified Chemical Front. *Phys. Rev. Lett.*, 96(15):154501, April 2006.
- [165] L. Šebestíková, J. D’Heroncourt, M. J. B. Hauser, S. C. Müller, and A. De Wit. Flow-field development during finger splitting at an exothermic chemical reaction front. *Phys. Rev. E*, 75(2):026309, February 2007.
- [166] L. Rongy and A. De Wit. Buoyancy-driven convection around exothermic autocatalytic chemical fronts traveling horizontally in covered thin solution layers. *The Journal of Chemical Physics*, 131(18):184701, November 2009.
- [167] P. M. Vilela and Desiderio A. Vasquez. Rayleigh-Taylor instability of steady fronts described by the Kuramoto-Sivashinsky equation. *Chaos: An Interdisciplinary Journal of Nonlinear Science*, 24(2):023135, June 2014.
- [168] Dan Coroian and Desiderio A. Vasquez. Oscillatory instability in a reaction front separating fluids of different densities. *Phys. Rev. E*, 98(2):023102, August 2018.
- [169] Yoshiki Kuramoto. *Chemical Oscillations, Waves, and Turbulence*, volume 19 of *Springer Series in Synergetics*. Springer Berlin Heidelberg, Berlin, Heidelberg, 1984.
- [170] Sonja Tötz, Jakob Löber, Jan Frederik Tötz, and Harald Engel. Control of transversal instabilities in reaction-diffusion systems. *New J. Phys.*, 20(5):053034, May 2018.
- [171] Radu Cimpanu, Susana N. Gomes, and Demetrios T. Papageorgiou. Active control of liquid film flows: Beyond reduced-order models. *Nonlinear Dyn.*

104(1):267–287, March 2021.

- [172] Leonid Kagan, Peter V. Gordon, and Gregory Sivashinsky. Viscous dissipation as a mechanism for spatiotemporal chaos in Rayleigh-Bénard convection between poorly conducting boundaries at infinite Prandtl number. *Phys. Rev. Fluids*, 7(11):113501, November 2022.
- [173] Yuji Nomi, Hiroshi Gotoda, Shuya Kandani, and Christophe Almarcha. Complex network analysis of the gravity effect on premixed flames propagating in a Hele-Shaw cell. *Phys. Rev. E*, 103(2):022218, February 2021.
- [174] J. D’Hernoncourt, A. Zebib, and A. De Wit. On the classification of buoyancy-driven chemo-hydrodynamic instabilities of chemical fronts. *Chaos*, 17(1):013109, March 2007.
- [175] James M. Hyman, Basil Nicolaenko, and Stéphane Zaleski. Order and complexity in the Kuramoto-Sivashinsky model of weakly turbulent interfaces. *Physica D: Nonlinear Phenomena*, 23(1-3):265–292, December 1986.
- [176] John N. Elgin and Xuesong Wu. Stability of Cellular States of the Kuramoto-Sivashinsky Equation. *SIAM J. Appl. Math.*, 56(6):1621–1638, December 1996.